

MINING THE *DROSOPHILA* GUSTATORY RECEPTOR FAMILY FOR NEW
THERMOSENSITIVE PROTEINS

- Basic science and tool development -

A Dissertation
presented to
the Faculty of the Graduate School
at the University of Missouri-Columbia

In Partial Fulfillment
of the Requirements for the Degree
Doctor of Philosophy

by

MARZIE AMIRSHENAVA

Drs. Lorin Milescu, Mirela Milescu, and Pamela Brown, Dissertation Mentors

DECEMBER 2021

© Copyright by

Marzie Amirshenava

2021 All Rights Reserved

The undersigned have examined the dissertation entitled

MINING THE *DROSOPHILA* GUSTATORY RECEPTOR FAMILY FOR NEW

THERMOSENSITIVE PROTEINS

- Basic science and tool development -

presented by Marzie Amirshenava,

a candidate for the degree of doctor of philosophy,
and hereby certify that, in their opinion, it is worthy of acceptance.

Professor Pamela Brown

Professor Mirela Milescu

Professor Lorin Milescu

Professor T.C. Hwang

Acknowledgments

There was no way that I could have completed this dissertation without the support of many people in my life.

I had the chance of working with three mentors during my PhD program. My journey started in the Milescu lab, where I started and completed my projects on ion channel biophysics. For the last two years of my program, I joined Dr. Pamela Brown's lab, wherein I got the support to continue my studies and finish my dissertation.

I owe an enormous amount of gratitude to my advisors and mentors, Drs. Mirela Milescu and Lorin Milescu. I am truly thankful to them for believing in me and helping me grow as a person and as a scholar. They always supported me, even at their rockiest times, and their passion for my success was a source of inspiration for me to keep working toward my goals. Though it was not always easy for me to keep up with the standards of the Milescu lab, my experience working in such a vibrant and friendly environment helped me grow professionally, as a scientist. There is a lot to thank Mirela and Lorin for, but here I would just like to say that I truly appreciate all the concerns and consideration they always had for me.

I would also like to thank Pam for the tremendous amount of support she provided me. Her encouragement, wisdom, and advice kept me on the right track toward finishing my dissertation research project. Pam, indeed, helped me pave the way to a complete thesis and I am deeply thankful of her.

I am very grateful to Dr. Troy Zars, who started the overall project on gustatory receptors, and who collaborated with my mentors until his untimely death, in 2018. I will always remember Troy as a very gentle man, and a great scientist and mentor.

I would also like to thank Dr. T.C. Hwang, my outside committee member, for his support and advice throughout my bumpy road toward completing my dissertation.

The project described in Chapter 3 reflects a collaboration between my mentors and Dr. Sergei Sukharev, from the University of Maryland – College Park. I learned a lot from Dr. Sukharev and his collaborators, Dr. Andriy Anishkin and Elissa Moller, and I am very grateful for their assistance and advice.

Last, but certainly not least, I am enormously thankful to my family back home in Iran, and to Mojtaba and Ahva, who are here with me. Thank you for all the support and encouragement you gave me all the time. I love you.

To everyone who is not named but was just as essential in my journey, thank you!

Table of Contents

| | |
|----------------------------------------------------------------------------------------------------------------------------|-------------|
| Acknowledgments | II |
| List of Figures | VI |
| Abstract | VIII |
| Introduction | 1 |
| Optogenetics – controlling cellular activity with light. | 1 |
| Alternatives to optogenetics | 2 |
| Thermosensation as a critical element of sensory perception | 3 |
| A brief overview of TRP channels..... | 3 |
| The limitations of ThemoTRPs | 4 |
| Thermosensitive gustatory receptors from <i>Drosophila</i> - a new family of thermogenetic tools..... | 5 |
| My contribution to the understanding of Gr28bD thermosensitivity and its application to thermogenetics | 6 |
| Chapter 1 | 8 |
| Abstract..... | 8 |
| Introduction | 9 |
| Results..... | 11 |
| Biophysical properties of Gr28bD in <i>Xenopus</i> oocytes..... | 11 |
| Modulation of neuronal activity by Gr28bD | 15 |
| Activation of Gr28bD alters behavior | 18 |
| Discussion..... | 20 |
| Chapter 2 | 30 |
| Temperature sensitivity in of Gr28bD orthologs..... | 30 |
| Abstract..... | 30 |
| Introduction | 30 |
| Results..... | 31 |
| Sequence similarity/identity between Gr28bD orthologs | 31 |
| A protocol for assessing temperature sensitivity of Gr | 32 |
| Thermosensitivity properties vary between Gr28bD orthologs | 33 |
| Conductance properties change with temperature | 35 |
| A mutation that results in a nonfunctional channel | 35 |
| Discussion..... | 36 |
| Chapter 3 | 45 |
| A model-driven analysis of thermosensation mechanisms in <i>Drosophila</i> thermosensitive gustatory receptors..... | 45 |
| Abstract..... | 45 |
| Introduction | 46 |
| Results..... | 48 |
| Computational modeling Gr28bD and its orthologs after Orco | 48 |

| | |
|---------------------------------------------------------------------------------------------------------------|------------|
| Screening Gr28bD mutants, as suggested by the computational model | 49 |
| Thermosensitivity properties of Gr28bD mutants | 51 |
| Discussion..... | 51 |
| Chapter 4 | 59 |
| Parameter optimization for ion channel models: integrating new data with known channel properties..... | 59 |
| Abstract..... | 59 |
| Introduction | 60 |
| Materials | 65 |
| Computer | 65 |
| Methods..... | 65 |
| Install the QuB software | 65 |
| Set up the modeling interface in QuB..... | 65 |
| Prepare the data for fitting | 66 |
| Prepare a kinetic model | 68 |
| Define linear parameter constraints | 69 |
| Calculating the total penalty | 78 |
| Setting up the optimization | 79 |
| Run the optimization..... | 80 |
| Run I – no constraints applied..... | 81 |
| Run II – all constraints applied | 82 |
| Conclusions | 84 |
| Chapter 5 | 101 |
| Methods..... | 101 |
| Gr28b constructs and oocyte expression..... | 101 |
| Site-directed mutagenesis | 101 |
| Oocyte electrophysiology and data analysis..... | 101 |
| Flies and rearing conditions (Mishra et al, 2018)..... | 103 |
| Calcium fluorescence imaging and data analysis (Mishra et al, 2018) | 103 |
| Behavioral experiments (Mishra et al, 2018)..... | 104 |
| Computational modeling of Gr28bD..... | 105 |
| Kinetic modeling software and simulations..... | 105 |
| Animal care | 105 |
| Conclusions and summary..... | 106 |
| References..... | 107 |
| Vita | 125 |

List of Figures

| | |
|-------------------------------------------------------------------------------------------------------------------------|----|
| Fig. 1.1. Biophysical properties of Gr28bD in <i>Xenopus</i> oocytes. | 24 |
| Fig. 1.2. Temperature-dependent modulation of cellular activity by Gr28bD | 26 |
| Fig. 1.3. Temperature-dependent modulation of fly behavior by Gr28bD | 28 |
| Fig. 2.1. Sequence alignment of Gr28b isoforms and Gr28bD orthologs | 39 |
| Fig. 2.2. Phylogenetic tree of Gr28b isoforms and Gr28bD orthologs | 40 |
| Fig. 2.3. Testing temperature sensitivity with a slow temperature ramp protocol | 41 |
| Fig. 2.4. Temperature-sensitive properties of Gr28bD orthologs | 42 |
| Fig. 2.5. The effect of temperature on ionic selectivity | 43 |
| Fig. 2.6. Sequence alignment of part of the polypeptide chain in Gr28b isoforms and Gr28bD orthologs | 44 |
| Fig. 3.1. Overlapped homology models of <i>D. melanogaster</i> Gr28bD and its orthologs | 53 |
| Fig. 3.2. Molecular dynamics simulations indicate dry hydrophobic pore in both structures, consistent with closed state | 54 |
| Fig. 3.3. Mutagenesis of key residues with potential functional roles | 56 |
| Fig. 3.4. Temperature sensitive properties of Gr28bD and its mutants | 57 |
| Fig. 3.5. Temperature sensitivity of single and double cysteine mutants | 58 |
| Fig. 4.1. State models for ion channel kinetic mechanisms | 86 |
| Fig. 4.2. Customizing the modeling interface in the QuB software | 87 |
| Fig. 4.3. Preparing the data for analysis | 88 |
| Fig. 4.4. A simple Nav model | 89 |

| | |
|-----------------------------------------------------------------------------------------|-----|
| Fig. 4.5. The model used as the starting point of optimization | 90 |
| Fig. 4.6. The starting model makes predictions that significantly deviate from the data | 91 |
| Fig. 4.7. Defining linear parameter constraints | 92 |
| Fig. 4.8. Defining behavioral constraints | 93 |
| Fig. 4.9. Setting up the optimization | 94 |
| Fig. 4.10. Model parameters – no constraints applied | 95 |
| Fig. 4.11. Model predictions – no constraints applied | 96 |
| Fig. 4.12. Optimization progress – no constraints applied | 97 |
| Fig. 4.13. Model parameters – all constraints applied | 98 |
| Fig. 4.14. Model predictions – all constraints applied | 99 |
| Fig. 4.15. Optimization progress – all constraints applied | 100 |

Abstract

Extrinsic control of neural activity is a powerful paradigm for understanding how neural circuits operate and regulate behavior. Traditionally, optogenetic tools are used to activate or inhibit neuronal activity with light. However, using visible light as the stimulus has some limitations, such as limited penetration in opaque tissue and overlap of absorption spectra when using multiple probes. A complementary approach is to use temperature as a stimulus, and thermosensitive TRP channels as the thermogenetic probes. These channels also have some limitations, particularly in their temperature sensitivity range. A new and exciting candidate for developing new thermogenetic tools has been recently identified as Gr28bD, a member of the *Drosophila* gustatory receptor family, normally involved in high-temperature avoidance behavior. My work on Gr28bD started with a characterization of its biophysical properties, particularly temperature sensitivity and ionic selectivity (Chapter 1). Then, to expand the pool of potential candidates for thermogenetic tools, I examined the orthologs of Gr28bD in other species of *Drosophila*, and I found five other receptors that have distinct thermosensitive properties (Chapter 2). To better understand the mechanism of thermosensitivity, our team successfully modeled the molecular structure of Gr28bD, obtaining preliminary evidence of its homotetrameric organization. To obtain further information on the structural and functional elements of this channel, I tested a series of Gr28bD mutants (Chapter 3). Finally, I participated in writing a book chapter on new computational methods for testing ion channel kinetic mechanisms (Chapter 4).

Introduction

Extrinsic control of neural activity is a powerful paradigm for understanding how neural circuits operate and regulate behavior. The role of specific neural elements (cells, circuits, etc.) can be dissected out by applying external stimuli that change (enhance, inhibit, or disable) the activity of those elements. These external stimuli must act exclusively on receptors expressed endogenously or genetically engineered in specific groups of cells. In turn, these receptors control, directly or indirectly, cellular activity. Ion channels and ionic pumps make great candidates for both receptor and controller roles, because they normally respond to a variety of stimuli and can act directly and immediately on neuronal activity, via an ionic current that can either depolarize or hyperpolarize the cell.

Optogenetics – controlling cellular activity with light. The discovery of light-activated microbial opsins triggered a revolution in neuroscience, establishing optogenetics as one of the most powerful techniques in biology. Opsins are seven transmembrane-domain proteins found in a variety of organisms, from archaea to plants. Conveniently, these proteins are ion channels or pumps that are modulated by light (Boyden, 2011). Three major classes have emerged as important players in the field: *halorhodopsins*, working as a chloride pump activated by yellow light, *channelrhodopsins*, acting as non-selective cation channels responsive to blue light, and *archaerhodopsins*, working as proton pumps responsive to yellow or green light (Chow et al., 2010; Gradinaru et al., 2008; Matsuno-Yagi & Mukohata, 1977; Schobert & Lanyi, 1982). Depending on their ionic selectivity, these natural opsins - or their engineered

variants - can generate either an excitatory (channelrhodopsin) or inhibitory (halorhodopsin and archaerhodopsin) current when subjected to the appropriate light stimulus, and thus can enhance or inhibit the firing activity of the host cell (Berndt et al., 2014; Friedmann et al., 2015).

Starting in neuroscience, optogenetics has expanded quickly into many other fields of biomedical research, providing uniquely powerful tools for studying behavior, physiology, and pathology, from reduced preparations such as brain slices (Shirai & Hayashi-Takagi, 2017) , to *in vivo* experiments with awake animals. For example, one of the first *in vivo* applications of optogenetics shed light on the role of neurons that produce orexin (a neuropeptide that regulates arousal, wakefulness, and appetite), in mice awakening from sleep (Adamantidis et al., 2007). Since then, *in vivo* optogenetics was applied to many other model organisms, from invertebrates such as *Drosophila*, to non-human primates (Dai et al., 2015; Diester et al., 2011; Vries & Clandinin, 2013).

Alternatives to optogenetics. The magic of optogenetics resides in its immediate response (milliseconds), reversibility, and specificity, which makes it possible to easily and precisely target specific groups of cells, and quickly manipulate their electrical excitability within a heterogeneous population, without interfering with the neighboring cells. However, optogenetics has some limitations too. Most importantly, light cannot easily penetrate opaque and/or thick tissues, such as the brain, without using invasive methods (Mancuso et al., 2011). Furthermore, the number of optogenetic receptors (opsins) that can coexist in a preparation is limited by the overlap in their light absorption spectra, even between opsins with different peak absorption wavelengths (Klapoetke et

al., 2014; V. Venkatachalam & Cohen, 2014). The intrinsic light sensitivity of some neurons may also be a drawback (Edwards et al., 2008).

To mitigate the shortcomings of optogenetics, one must turn to alternative and/or complementary tools for extrinsic neural control. In principle, the physical stimulus could be any form of energy other than (visible) light (e.g., chemical, electrical, or mechanical), as long as it can be applied with high specificity to certain groups of cells. Of course, reversibility, quick response, and tissue penetration are also very important aspects. A logical possibility is to use heat as the physical stimulus and rely on temperature-sensitive molecules that can be used, directly or indirectly, to modulate cellular excitability. What molecules can we use as thermogenetic probes?

Thermosensation as a critical element of sensory perception. From bacteria to humans, organisms are able to survive in a generally hostile environment because they can perceive different stimuli, process them, and flee to escape danger or approach food to eat. We react not only to chemicals, light, mechanical pressure and sound waves, but also to temperature. Like all the other senses, thermosensation is vital, enabling us to avoid dangerous temperatures and maintain appropriate body temperature for physiological processes. As with other sensorial modalities, the key molecules that mediate thermosensation are ion channels.

A brief overview of TRP channels. The most studied thermosensitive receptors are the transient receptor potential (TRP) channels (K. Venkatachalam & Montell, 2007). A variety of thermosensitive TRP channels, from cold activated to heat activated, have been identified in a wide range of animals, from *C. elegans* to humans (Barbagallo & Garrity, 2015; Caterina et al., 1997; Caterina & Julius, 2001; Dhaka et al., 2006;

Patapoutian et al., 2003). These channels are highly responsive to changes in temperature, covering the physiologically relevant range, from noxious cold (<15 °C) to burning heat (>43°C) (Clapham, 2003; Dhaka et al., 2006; Jordt et al., 2003; Latorre et al., 2009; Voets et al., 2005). These receptors respond not only to temperature, but also to other types of stimuli, converting multimodal sensory information to electrical signals (Dhaka et al., 2006).

ThermoTRPs, a subset of TRP proteins found in at least four TRP subfamilies (TRPV, TRPA, TRPM, and TRPP), have high temperature sensitivity and are critical players in thermosensation and other temperature-regulated processes, in a wide range of organisms. ThermoTRPs contain six transmembrane segments, similar to voltage-gated ion channels, and form temperature-activated cationic channels (Liao et al., 2013; Ramsey et al., 2006). ThermoTRP are also known for their remarkably high Q_{10} values: 100 for TRPV2 (mouse), and 116 for TRPA1 type A (*Drosophila*) (Clapham & Miller, 2011; Hille, 2001; Xiao & Xu, 2021). Q_{10} represents the ratio between channel activities at temperatures separated by 10 °C. A high Q_{10} is potentially advantageous, because a small change in temperature can bring upon a large change in ionic current.

The limitations of ThermoTRPs. These channels represent the best studied group of thermosensors and have become valuable experimental tools for controlling cellular excitability (Bellemer, 2015; Bernstein et al., 2012). However, ThermoTRPs have some limitations as well. First, ThermoTRPs lack the millisecond temporal resolution of optogenetic tools (Hamada et al., 2008; Pulver et al., 2009; Zhang et al., 2010), although this is more a matter of how fast temperature can be changed, because at least some

ThermoTRPs (TRPV1) can respond fast (5-10 ms) to IR laser-induced temperature changes (Ermakova et al., 2017).

Furthermore, these proteins are tuned to report on conditions where it's either too cold or too hot, and thus have limited use in the physiological range. Another problem is that ThermoTRPs can be modulated by voltage as well, which means that their response to external temperature stimuli will be influenced by their response to the electrical activity of the cell, normal or induced (Dhaka et al., 2006; Nilius et al., 2005; Zheng, 2013). Finally, only excitatory ThermoTRPs have been characterized to date, and so they cannot be used to down-regulate cellular activity.

Thermosensitive gustatory receptors from *Drosophila* - a new family of thermogenetic tools. The limitations of ThermoTRPS have created the need for alternative or complementary thermogenetic probes. Fortunately, another molecule from nature's arsenal has come to the rescue, through a serendipitous discovery made by Paul Garrity and his collaborators at Brandeis University, that some mutant *Drosophila melanogaster* fruit flies have lost preference for comfortable temperatures (Ni et al., 2013). Surprisingly, these mutant flies lacked not a TRP channel, but a gustatory receptor. Further study has determined that thermosensation in fruit flies relies on two sets of ion channels, the TRPs and the Gustatory Receptor (Gr) 28bD (Barbagallo & Garrity, 2015).

Together with olfactory receptors, gustatory receptors in insects form the large superfamily of chemoreceptors, with rather limited sequence similarity between the two families and within each family. In *Drosophila*, there are 60 genes that encode for 68 gustatory receptors. These membrane proteins are proposed to have a seven-

transmembrane topology, with an intracellular N-terminus and an extracellular C-terminus (Benton et al., 2006a). One of the gustatory receptor genes, *Gr28b*, encodes five alternatively spliced isoforms (Gr28bA through E). Gr28bD is the only isoform involved in rapid heat avoidance in flies, although its C-terminal shares 100% sequence identity with the other isoforms (Ni et al., 2013b). In fact, Gr28bD is the only member of the *D. melanogaster* gustatory receptor family that exhibits thermosensitivity. This is surprising, as Gr28bD does not exhibit any unusual sequence features that make it either different from the other GRs, or similar to TRPs, with which it shares no sequence homology.

My contribution to the understanding of Gr28bD thermosensitivity and its application to thermogenetics. The discovery of Gr28bD as a thermosensitive protein has opened the door to our lab for new and exciting research, in which I was involved from the beginning of my graduate studies. First, I participated in the initial characterization of Gr28bD as a thermosensitive channel, started by my former colleague, Dr. Autoosa Salari. For this, I used *Xaenopus laevis* oocytes as the heterologous expression host, and the two-electrode voltage clamp (TEVC) technique to measure channel activity under different conditions. Through this research, as presented in ***Chapter 1***, we established that Gr28bD is a voltage-insensitive, non-selective cation channel that responds with a robust current when the temperature rises above 10-15 °C, with little or no adaptation. In parallel, my colleague Benton Berigan and Dr. Aditi Mishra from the Zars lab have validated the potential of Gr28bD as a thermogenetic tool.

In a second project, I started to mine the *Drosophila* genus for other thermosensitive gustatory receptors, with a focus on Gr28bD orthologs. In this research, as presented in ***Chapter 2***, we identified five Gr28bD orthologs with high (>80%)

sequence homology to Gr28bD from *D. melanogaster*, and established that these orthologs have robust thermosensitivity, but with different characteristics. Interestingly, these characteristics seem to match the temperature preference of the respective species. Again, Benton Berigan and Dr. Aditi Mishra have tested and validated these orthologs for thermogenetic applications.

With all this wealth of functional data, my lab has recently started a collaboration with Dr. Sergei Sukharev at the University of Maryland – College Park, to investigate the molecular mechanisms of thermosensation. In this structure–function study, as described in *Chapter 3*, I tested a number of Gr28bD mutants, with the aim of establishing key structural elements involved in thermosensitivity, and we generated a computational model for several Gr28b isoforms. Finally, I had a chance to participate in writing a book chapter that describes a computational method for analyzing ion channel kinetic mechanisms, as described in *Chapter 4*.

Chapter 1

The *Drosophila* Gr28bD product is a non-specific cation channel that can be used as a novel thermogenetic tool

Adapted from: Mishra, A., Salari, A., Berigan, B. R., Miguel, K. C., Amirshenava, M., Robinson, A., Zars, B. C., Lin, J. L., Milescu, L. S., Milescu, M., & Zars, T. (2018). The *Drosophila* Gr28bD product is a non-specific cation channel that can be used as a novel thermogenetic tool. *Scientific Reports*, 8(1), 901. <https://doi.org/10.1038/s41598-017-19065-4>.

This chapter reflects a collaboration between three different labs (M. Milescu, L. Milescu, and T. Zars). My contribution was to design TEVC experiments, record data, analyze the results, and participate in writing and editing the manuscript. Some of my data and analysis results have been included in Fig. 1.1, with the rest obtained by Dr. Autoosa Salari and Kayla Miguel. The imaging experiments shown in Fig. 2.1 were performed by Benton Berigan, and the behavioral experiments shown in Fig. 3.1 were done by Dr. Aditi Mishra.

Abstract

Extrinsic control of single neurons and neuronal populations is a powerful approach for understanding how neural circuits function. Adding new thermogenetic tools to existing optogenetic and other forms of intervention will increase the complexity of questions that can be addressed. A good candidate for developing new thermogenetic tools is the *Drosophila* gustatory receptor family, which has been implicated in high-temperature

avoidance behavior. We examined the five members of the Gr28b gene cluster for temperature-dependent properties via three approaches: biophysical characterization in *Xenopus* oocytes, functional calcium imaging in *Drosophila* motor neurons, and behavioral assays in adult *Drosophila*. Our results show that Gr28bD expression in *Xenopus* oocytes produces an inward cationic current that is activated by elevated temperatures. This current is non-inactivating and non-voltage dependent. When expressed in *Drosophila* motor neurons, Gr28bD can be used to change the firing pattern of individual cells in a temperature-dependent fashion. Finally, we show that pan-neuronal or motor neuron expression of Gr28bD can be used to alter fruit fly behavior with elevated temperatures. Together, these results validate the potential of the Gr28bD gene as a founding member of a new class of thermogenetic tools.

Introduction

Extrinsic control of cellular activity is a powerful paradigm for understanding how neural circuits regulate behavior. The standard approach relies on optogenetics to activate or inhibit neuronal activity with light (Bernstein et al., 2012; Klapoetke et al., 2014). However, the existing molecular tools used in optogenetic experiments have overlapping spectral sensitivities, limiting the number of neural components that can be controlled independently. As the field moves toward testing more and more components within a neural circuit, other modalities for extrinsic control must be identified.

Thermogenetic tools use temperature as the physical controlling agent and provide an ideal complementary approach to optogenetics (Bernstein et al., 2012; Ermakova et al., 2017).

Multiple classes of temperature-sensing proteins have been identified in *Drosophila*, including the transient receptor potential (TRP), ionotropic receptor, and gustatory receptor (Gr) families (Barbagallo & Garrity, 2015; Cao et al., 2013; Hamada et al., 2008; Ni et al., 2013a, 2016). Each one of these classes provides unique opportunities for developing new thermogenetic tools, given their specific temperature sensitivity, ionic selectivity, kinetics, and regulation (Bernstein et al., 2012; Ni et al., 2016; Rosenzweig et al., 2005). With a response threshold of about 25°C and abrupt activation with temperature (Hamada et al., 2008; Kang et al., 2012), the TRP protein family (e.g., TRPA1) has been the most extensively studied and applied to understand neural circuits in *Drosophila* and other organisms (Lewis et al., 2015; Pavlou et al., 2016; Shyu et al., 2017).

Although their potential for thermogenetic applications has not been explicitly tested so far, the *Drosophila* Grs are promising new candidates. This large family contains some members with ion channel activity and with advantageous temperature responses that fall within the physiological range of model organisms (Ni et al., 2013a; Sato et al., 2011). For example, the Gr28bD gene product has a neurophysiological response threshold similar to TRPA1, when tested in adult *Drosophila* neurons (Ni et al., 2013a). However, the Grs differ widely from TRPs in their primary structure and predicted molecular architecture, giving us an opportunity to discover new molecular mechanisms of temperature responsiveness and to engineer new tools for extrinsic control via temperature.

We examined here the temperature response of the five members of the Gr28b gene family (Gr28bA through Gr28bE) via three approaches: biophysical characterization

in *Xenopus laevis* oocytes, functional calcium imaging in *Drosophila* motor neurons, and behavioral assays in adult *Drosophila*. Heterologous expression systems (e.g., oocytes or mammalian cell lines) are ideally suited for biophysical analysis, as the current can be better isolated and studied. Despite successful characterization of related gustatory and olfactory receptors in various artificial expression systems (Sato et al., 2008, 2011), previous attempts to heterologously express Gr28b proteins were reported ineffective (Ni et al., 2013a). However, we were able to establish a quick and robust expression system to study the Grs in *Xenopus* oocytes, and found that Gr28bD is the only member of the Gr28b family that generates a temperature-dependent current. When expressed in *Drosophila* motor neurons, Gr28bD can alter the firing patterns of individual cells as a function of temperature. In behaving flies, neuronal expression of Gr28bD leads to temperature-dependent changes in behavior. Altogether, these results validate the potential of the Gr28bD gene as a founding member of a new class of thermogenetic tools.

Results

Biophysical properties of Gr28bD in Xenopus oocytes. We report here the first successful expression of Gr28bD in *Xenopus laevis* oocytes, using established procedures (see Methods). We examined the temperature dependence, ionic selectivity, and basic kinetic properties of Gr28bD, using the two-electrode voltage clamp (TEVC) technique to record oocyte currents under different conditions of temperature, membrane potential, and ionic composition of the extracellular solution. The other members of the Gr28b family were also tested, but no currents were observed. When subjected to temperature steps (Fig. 1.1A, bottom panel), oocytes injected with Gr28bD cRNA exhibit large,

temperature-sensitive currents (Fig. 1.1A, middle panel). In contrast, water-injected oocytes exhibit only a tiny amount of background current, with no significant temperature dependence (Fig. 1.1A, top panel). As can be observed from the example in Fig. 1.1A, our temperature application system cannot change temperature rapidly, which makes it difficult to estimate the kinetics of the Gr28bD current in response to a change in temperature. Cross-correlation analysis indicates that the current lags behind the temperature by approximately five seconds. Whether this lag is an experimental artifact or genuine channel kinetics remains to be determined through more precise temperature application experiments.

For thermogenetics applications, it is very important to know whether the temperature-induced current can be maintained over long durations. From the response to temperature steps (Fig. 1.1A), we determined that the Gr28bD currents do not inactivate significantly over a 100-second time course. Moreover, the currents return to their initial value upon cooling. The properties of a temperature-dependent current can be summarized by three quantities: the threshold of activation, the steepness of the response, and the saturation. To examine these properties, we subjected the oocytes to slow temperature ramps (approximately $2.5\text{ }^{\circ}\text{C} / 60\text{ s}$), which should allow the channel to reach a state of quasi-equilibrium with respect to slow activation or inactivation kinetics, if any, and would also minimize temperature distribution artifacts within the recording chamber. The temperature was limited to a range of $10\text{ }^{\circ}\text{C} - 40\text{ }^{\circ}\text{C}$ to avoid damage to the oocyte and to maintain reliable recording conditions. An example of the current elicited by a temperature ramp is shown in Fig. 1.1B. In this case, the cross-correlation analysis indicates a lag of less than one second. Furthermore, the on-ramp and the off-ramp

produce approximately symmetrical responses, altogether confirming that channels are at quasi-equilibrium at these slow ramp rates. The logarithm of the normalized current versus temperature is shown in Fig. 1.1C. Inspection of the current response reveals a threshold of activation of approximately 14 °C. Above this temperature, the logarithm of the current increases linearly with a slope that corresponds to a Q_{10} of approximately 9.05 ± 0.88 , until 20 °C, where Q_{10} changes to 5.2 ± 0.95 ($n = 12$). These results were obtained with an extracellular solution (ND96) commonly used for oocytes recordings, containing 1.8 mM Ca^{2+} .

However, oocytes are known to express endogenous calcium-activated chloride currents (Boton et al., 1989) which could contaminate our measurements, should the Gr have a significant calcium conductance. We tested this possibility using a nominally calcium-free ND96 recording solution and found Q_{10} values of 9.9 ± 1.3 and 5.6 ± 1.2 ($n = 6$), below and above 20°C, respectively. These values are not statistically different from those reported above, obtained with 1.8 mM Ca^{2+} (unpaired t-test, p -value > 0.12). The *Gr28bD* currents do not exhibit any detectable voltage dependence, at either low (10 °C) or high (35 °C) temperature, as illustrated in Fig. 1.1D and E. In control oocytes, the endogenous currents are very small across a broad voltage range (-100 mV - +30 mV), with no discernable voltage dependence. This implies that the currents recorded from Gr28bD-injected oocytes are generated by *Gr28bD*, with very little contamination from endogenous currents across a wide range of temperatures and membrane potentials.

Under the ND96 extracellular solution, containing (in mM) 96 NaCl, 2 KCl, and 1.8 CaCl_2 , the Gr28bD currents are inward at -60 mV (see Fig. 1.1A), with a measured reversal potential of -12 ± 0.7 mV (Fig. 1E). This value suggests that Gr28bD would act

as an excitatory agent in thermogenetics applications. Nevertheless, to be able to predict the response of the channel and the nature of its effect in other biological preparations and solutions, it is necessary to determine its ionic selectivity. Under the ND96 solution and assuming 7 mM Na⁺, 100 mM K⁺, and 0.1 mM Ca²⁺ intracellular concentrations (Weber, 1999), the predicted Nernst potentials would be approximately +69 mV for Na⁺, -104 mV for K⁺, and +24 mV for Ca²⁺, at 35 °C. The measured reversal potential of -12 mV under ND96 does not match any of these values, indicating that the channel is conducting more than one type of ion. Considering these measured and estimated values, the relative K⁺ conductance must be at least 35%, as would be calculated assuming zero relative Na⁺ conductance, or as much as 47%, assuming zero relative Ca²⁺ conductance.

To further investigate the relative conductance for Na⁺ ions, we recorded Gr28bD currents under various Na⁺ concentrations, with Na⁺ ions accordingly replaced by NMDG⁺, which is known not to permeate through Na⁺ or cation non-selective channels (Caterina et al., 1999). The relative conductance for an ion can be calculated from the ratio between the observed shift in the reversal potential of the current and the predicted shift in the Nernst potential for that ion. As illustrated in Fig. 1.1F, when the extracellular Na⁺ concentration is reduced from 96 to 48 mM, the measured reversal potential changes from -12 to -23.7 ± 0.17 mV, while the predicted Na⁺ Nernst potential changes from +69 to +51 mV, corresponding to an estimated 65% relative Na⁺ conductance. When the extracellular Na⁺ is reduced to 2 mM, the measured reversal potential changes to -59 ± 0.9 mV, while the predicted Na⁺ Nernst potential changes to -33 mV, corresponding to an estimated 45% relative Na⁺ conductance. These results average to a 55% relative Na⁺

conductance. Considering this and the above estimates for the K^+ conductance (35% to 47%) the partial Ca^{2+} conductance should be less than 10%.

We also tested low-calcium extracellular solutions, one nominally Ca^{2+} free and one with 0.6 mM Ca^{2+} , and found only a small negative shift in the reversal potential, of less than 1 mV. This result is consistent with a Ca^{2+} conductance of less than 4%.

Additional experiments in which Cl^- was replaced with gluconate ($C_6H_{11}O_7^-$) did not alter the reversal potential, suggesting that the Gr28bD current is not carried by Cl^- ions or contaminated by endogenous chloride currents (data not shown).

Altogether, these results clearly indicate the non-selective cationic nature of the current, similar to that of several TRP channels (K. Venkatachalam & Montell, 2007). Although further experiments are necessary to obtain more precise values, most of the Gr28bD conductance appears to be due to Na^+ (55%) and K^+ (35 - 47%) permeability, with any potential remainder due to Ca^{2+} ions. In contrast to *Gr28bD*, expression of the four other Gr28b isoforms (A, B, C, and E) did not produce any measurable current, temperature-sensitive or not, above the endogenous level. Moreover, co-expression of all possible binary combinations of these isoforms did not elicit any temperature-dependent current (data not shown). However, the possibility of functional Gr28b heteromers cannot be ruled out, as more than two isoforms may be needed to form a functional protein.

Modulation of neuronal activity by Gr28bD. To use a thermogenetic tool, one must have a good way to calibrate and monitor its effects on neuronal activity. As shown by our biophysical experiments and by a previous study (Ni et al., 2013a), Gr28bD generates a temperature-sensitive inward current in both *Xenopus* oocytes and *Drosophila* neurons, and elicits strong proboscis extension when expressed in sweet-responsive fruit

fly chemosensors. According to these results, Gr28bD should, in principle, generate excitatory inward currents in target neurons. However, enough current must be generated relative to the battery of endogenous currents normally expressed by a cell to modulate its activity. In this regard, electrophysiology is potentially the most precise measuring method (Ni et al., 2013a), but it is not suitable for large-scale monitoring of neuronal populations. Therefore, we used imaging techniques to test Gr28bD in adult *Drosophila*, in combination with a genetically-encoded calcium indicator (GCaMP6f), to determine if it produces a robust, temperature-dependent effect that can be easily identified, analyzed, and interpreted with common imaging and data analysis techniques.

We also tested control flies expressing only GCaMP6f. For these tests, we focused on the motor neurons in the lateral abdominal neuromeres, located in the ventral nerve cord (VNC). As illustrated in Fig. 1.2A, these neurons are a good target for calcium imaging experiments as they are easy to identify and consistently exhibit robust firing activity. Moreover, these neurons are conveniently located in the same plane and exhibit calcium fluorescence with comparable intensity and good signal-to-noise ratio, altogether making it easy to image multiple cells at the same time.

Additionally, motor neurons are generally larger than other neuronal types, making them a good test system to determine whether expression of Gr28bD can generate enough current to modulate cellular activity. The thermosensitive effect of Gr28bD on neuronal activity was tested with temperature steps alternating between 19 °C and 28 °C. We recorded from 21 GCaMP6f control cells in five flies and 20 Gr28bD + GCaMP6f cells in six *GR28bD*-expressing flies. Under repetitive application of

temperature steps, calcium fluorescence activity could be observed for 73.6 ± 4.5 minutes in control flies and 49.7 ± 7.4 minutes in Gr28bD-expressing flies.

One would anticipate that changing temperature by approximately $10\text{ }^{\circ}\text{C}$ would have an effect on neuronal activity, even in control flies, but would these changes be different between control and Gr28bD-expressing flies? Indeed, as illustrated in Fig. 1. 2B, control flies (top panel) and Gr28bD-expressing flies (middle and bottom panels) respond differently to temperature steps. The most notable distinction is in how the average fluorescence intensity changes between low and high temperature (Fig. 1. 2C). In control flies, the average fluorescence level is attenuated by high temperature ($\Delta F/F = -0.1524 \pm 0.1358$), but it is slightly increased in Gr28bD-expressing flies ($\Delta F/F = 0.03656 \pm 0.10$) (unpaired t-test; p-value < 0.00001). Although the temperature-induced change in average fluorescence in Gr28bD-expressing neurons is small ($\approx 3.7\%$), it should be regarded as relative to the control group. Accordingly, the Gr28bD-specific effect is an overall increase in fluorescence of almost 20%. The average calcium fluorescence is proportional to the overall neuronal activity (Helmchen et al., 1996; Spruston et al., 1995), independent, to some degree, of the specific firing pattern (e.g., tonic spiking vs. bursting). Therefore, the observed changes in average fluorescence elicited by high temperature can be interpreted as a slow-down of neuronal activity in control flies versus an increase in activity in Gr28bD-expressing flies.

GCaMP6f is in principle capable of reporting individual action potentials. However, without simultaneous electrical recordings, it is difficult to determine whether the individual calcium fluorescence events detected in our data correspond to single action potentials or to more complex patterns of activity (e.g., episodes of high-frequency

firing). Thus, we used the continuous wavelet-transform (CWT) with a Morlet wavelet (Ruffinatti et al., 2011) to examine the spectral content of the calcium fluorescence data. As illustrated by the example recordings in Fig. 1. 2B, there are significant differences between control (top panel) and Gr28bD-expressing flies (middle and bottom panels).

In control neurons, the spectral content of fluorescence data changes relatively little with temperature, with respect to both frequency and amplitude. These neurons are active at both low and high temperatures, as demonstrated by the multiple spectral bands that are visible in the 1 - 4 Hz frequency range, some of which potentially corresponding to the repetition rate of action potentials. The strongest of these bands (1 - 2 Hz) becomes slightly more intense and more regular at high temperature. In contrast, some of the Gr28bD-expressing neurons exhibit similar tonic activity at 19 °C (n = 8), while others are in a more quiescent state (n = 12). The onset of high temperature triggers a remarkable increase in the amplitude of high-frequency oscillations, lasting as much as 100 seconds. The effects of temperature were reversible in both control and Gr28bD-expressing flies. After each four-minute exposure to 28 °C, the cells resumed their normal activity when temperature was returned to 19 °C, throughout the lifetime of the preparation.

Activation of Gr28bD alters behavior. Our imaging experiments demonstrate the ability of Gr28bD to induce temperature-dependent effects in the firing activity of individual neurons. However, we also see temperature effects in control flies. To determine how these specific and non-specific effects scale up to the level of the entire organism, we investigated the behavioral response of flies to different temperatures in the 24 - 40 °C range. Gr28bD and each of the other four different transgenes in the Gr28b

family were individually tested with pan-neuronal overexpression using the nSyb-GAL4 driver. An initial screening exposed flies to temperatures ranging from 24 to 40 °C in two-degree steps (Fig.1. 3A). Most of the flies overexpressing Gr28bD became incapacitated at 34 °C, in contrast to flies overexpressing the Gr28bA, C and E transgenes, which did not incapacitate. A temperature response was also observed for Gr28bB flies, but only at the upper temperature limit of our experimental paradigm (40 °C), which prevented further investigation. We also tested the effect of a more restricted overexpression of Gr28bD, in motor neurons only, using the OK6-GAL4 driver. In this case, we found that most of the flies were incapacitated at 36 °C (Fig.1. 3A).

In the remainder of the Results section, all references to overexpression should be read as “pan-neuronal” overexpression. To obtain a better resolution of the Gr28bD-induced effect, flies from control and experimental genotypes were subjected to temperatures in the 32 - 40 °C range in one-degree steps. Flies overexpressing Gr28bD became incapacitated between 33 and 36 °C, with most of the flies incapacitated at 34 °C (Fig.1. 3B). In contrast, no genetic control flies were incapacitated. Next, we tested whether the time to incapacitation and the time to recovery from incapacitation are affected by the exposure temperature. We examined these two quantities by exposing flies overexpressing Gr28bD to a sudden increase in temperature for 90 seconds (Fig.1. 3C). All flies exposed to 36, 38, and 40 °C became incapacitated during the 90 second exposure, with more than 50% reaching incapacitation within 10 seconds (Fig.1.3D). At 34 °C, only ≈65% of the exposed flies became incapacitated and the time to incapacitation was significantly longer, suggesting that 34 °C is a threshold value for temperature-sensitive behavior. In contrast, none of the genetic control flies were

incapacitated within the 90 seconds exposures at any tested temperature, with the exception of the UAS-Gr28bD heterozygous flies. About 10% of these flies became incapacitated at 40 °C, potentially due to a leaky expression of the UAS-Gr28bD transgene. The time to recovery for flies overexpressing Gr28bD was more graded than the time to incapacitation. Flies exposed to high temperatures took an exponentially longer time to recover than flies exposed to low temperatures. From 34, 36, 38, and 40 °C, the 50% recovery time was 20, 162, 383, and 760 seconds, respectively. Moreover, at 40 °C, the recovery was not complete within the 1080 seconds of the recovery phase of the experiment with 22% of the flies remaining incapacitated.

Discussion

The ability to control neuronal activity is the most direct and powerful approach for understanding how neural circuits control behavior. An ideal suite of tools for extrinsic neuronal control would include activating and inactivating methods that can target multiple cell types and neuronal populations in a behaving animal. The development of thermogenetic tools as a complement to optogenetics and other approaches is a promising step toward multi-modality control of neuronal activity (Bernstein et al., 2012; Klapoetke et al., 2014). The *Drosophila* gustatory receptor gene family, which has been largely unexplored with respect to temperature responsiveness, provides an opportunity to identify novel thermogenetic tools. We show here that one member of the Gr28b family, Gr28bD, generates a temperature-dependent cation current when expressed in *Xenopus* oocytes. This current does not require any explicit co-expression of additional factors, suggesting the possibility that Gr28bD forms a previously uncharacterized temperature-sensitive ion channel (Fig. 1.1).

Moreover, we show that overexpression of Gr28bD in motor neurons can be used to drive temperature-dependent neuronal activity (Fig.1. 2). The expression system is sufficient to drive activity in these relatively large neurons, suggesting that the Gr28bD product can be used in multiple cellular contexts. Finally, we show that temperature activation of Gr28bD overexpressed in neurons can have profound effects on behavior (Fig.1. 3). Expression of Gr28bD in all neurons gives rise to temperature-dependent paralysis, with the time to incapacitation and the recovery time both related to exposure temperatures.

We also demonstrate that flies with Gr28bD expression restricted to motor neurons display a similar temperature-dependent paralysis, but shifted by approximately +2 °C. This small shift could be explained by a difference in Gr28bD expression levels, as caused by different strengths of the two GAL4 drivers, and / or by differences between the neuronal types overexpressing Gr28bD. According to these results, the Gr28bD gene product is useful as a thermogenetic tool and is a good starting point for designing new molecular tools for extrinsic control of neuronal activity. Our first attempts to demonstrate that behavior can be altered with Gr28bD activation showed that the gene product has a sharp temperature effect, with nearly all flies reaching paralysis within a narrow temperature window (33 - 36 °C). This temperature range for Gr28bD is about 4 °C higher than that required to activate and paralyze TRPA1 expressing flies (data not shown).

Interestingly, the time required for recovery from paralysis was temperature dependent, with flies exposed to higher temperatures taking longer to recover from paralysis. The difference in recovery at different temperatures could be a function of the

Gr28bD product or of the neural systems that need to recover from extrinsic activation. However, the temperature-sensitive currents recorded in *Xenopus* oocytes expressing Gr28bD follow the change in temperature equally rapidly (Fig. 1.1A), within seconds, between any two temperatures. This suggests that the temperature-dependent slow recovery rates observed in the behavioral experiments are the result of neuronal properties, rather than Gr28bD temperature sensitivity and kinetics. Further experiments are necessary to more precisely determine the time response of the Gr28bD to changes in temperature. With the estimates we have so far (seconds), it is possible that Gr28bD kinetics are slow compared to fly behaviors such as the escape response or the tuning of wing movements in flight (Card & Dickinson, 2008; Schnell et al., 2017). Nevertheless, the response kinetics are compatible with the testing of other behaviors, such as phototaxis, negative gravitaxis, and conditioning, which are typically measured in the seconds range (Armstrong et al., 2006; Benzer, 1967; Kahsai & Zars, 2011).

While Gr28bD has clear temperature sensitive effects that can be corroborated at all tested levels (oocytes, individual neurons, and whole organism), the other members of the Gr28b family have no observable effect (Gr28bA and C) or are less consistent across experimental paradigms (Gr28bB and E). Thus, expression of Gr28bB in *Xenopus* oocytes does not show a temperature-dependent current (data not shown). However, pan-neuronal expression of Gr28bB gives rise to temperature-dependent paralysis at the highest probed temperature of 40 °C (Fig. 1.3A). One possible explanation is that Gr28bB requires higher temperatures to activate and generate current, the temperatures which could not be reached in the *Xenopus* experiments.

Alternatively, there may be insufficient expression of Gr28bB in *Xenopus* oocytes, causing a lack of detectable current. Heterologous expression systems that can tolerate higher temperatures may be able to address this issue. However, the observed temperature-dependent paralysis is an encouraging result, suggesting that the Gr28bB gene product may also generate a temperature responsive current.

Finally, there is evidence from a previous study that Gr28bE has temperature response properties when expressed in the hot-cells of the *Drosophila* antennae (Ni et al., 2013a). In our experiments, expression in *Xenopus* oocytes and in all *Drosophila* neurons do not show any detectable temperature-dependent effect of Gr28bE. There may be factors in the hot-cells that provide the environment for Gr28bE temperature responsiveness that are lacking in other neurons and in *Xenopus* oocytes.

To summarize, we show that Gr28bD, a member of the *Drosophila* Gustatory receptor family, can be used as a thermogenetic tool. The gene encodes a temperature-dependent current in heterologous cells and is able to activate multiple cell types in the fly. Gr28bD can be used to interrogate neural circuit function in imaging and behavioral studies. Further testing of the Gustatory receptor family may identify new members with temperature sensitive properties that may aid in the development of designer thermogenetic tools, useful in multiple models, and result in a better understanding of how ion channels respond to temperature.

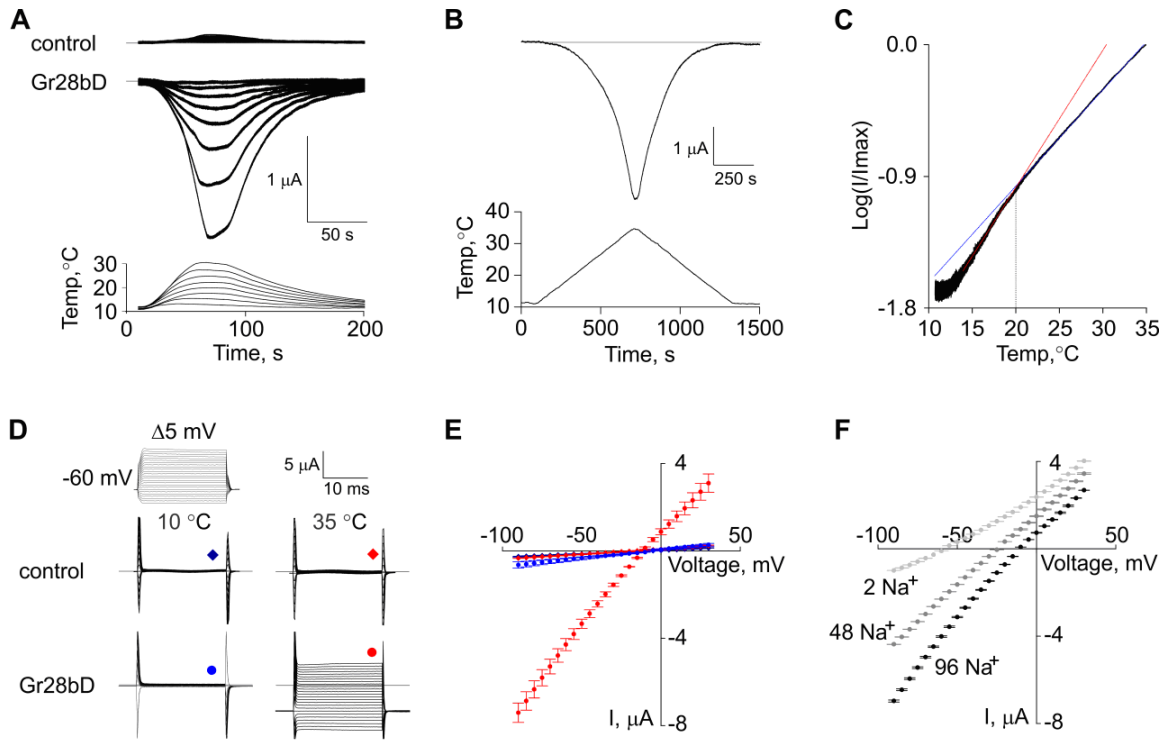


Fig. 1.1. Biophysical properties of Gr28bD in *Xenopus* oocytes. (A) Temperature response: oocytes injected with Gr28bD cRNA display temperature-activated inward current in response to temperature steps. Control oocytes injected with RNase-free water exhibit no significant current. (B) Response of Gr28bD current to slow temperature ramps ($\approx 2.5\text{ }^{\circ}\text{C} / 60\text{ s}$). (C) Temperature sensitivity: the logarithmic plot of normalized Gr28bD current versus slow ramp temperature exhibits two ranges of temperature sensitivity. Red and blue lines represent linear fits to data in each range ($14 - 19\text{ }^{\circ}\text{C}$ and $21 - 35\text{ }^{\circ}\text{C}$). Q_{10} values were calculated using the equation $Q_{10} = 10^{10 \times s}$, where s is the slope of the linear fit. (D) Voltage response: control and Gr28bD currents in response to voltage steps at two different temperatures. Endogenous currents are small at all voltages and temperatures. (E) Current-voltage relationships for GR28bD-expressing and control oocytes at 10 and $35\text{ }^{\circ}\text{C}$, as obtained with the voltage step protocol in D. Gr28bD current

does not show voltage sensitivity at the tested temperatures. The symbols are as in D. (F) Ionic selectivity: Gr28bD currents were obtained as in E, at 35 °C, with Na⁺ partially replaced by NMDG⁺ in the external solution (96 mM Na⁺: 0 mM NMDG⁺, 48 : 48, and 2 : 94). The measured reversal potentials were (in mV): -12.0 ± 0.7 , -23.7 ± 0.2 , and -59.0 ± 0.9 , respectively. The holding voltage was -60 mV in all experiments. Data shown in A, B, C, and D are representative examples. In E and F, data points are mean \pm SEM (n = 6 - 8). The currents were obtained under ND96 solution (see methods), except were otherwise noted.

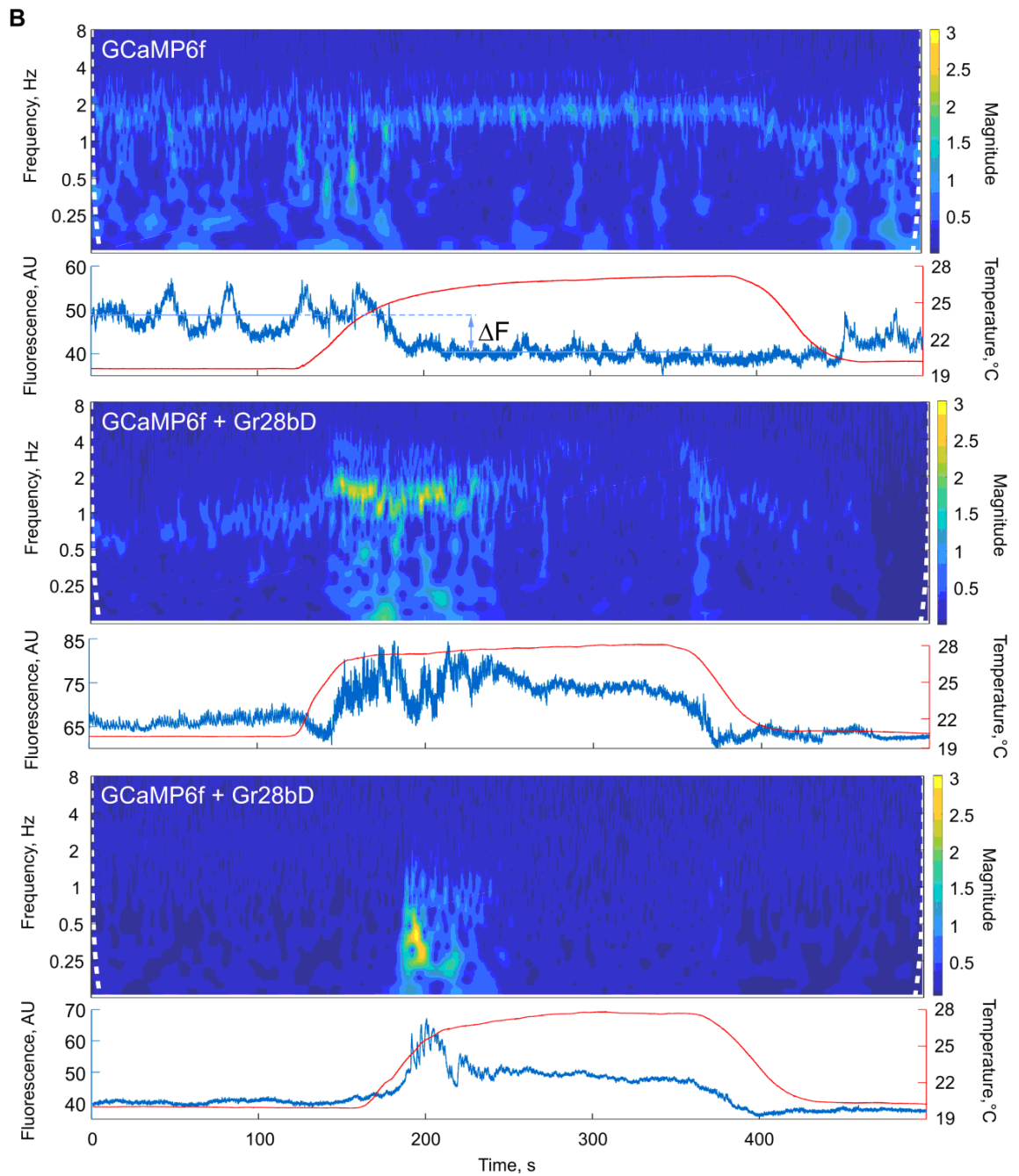
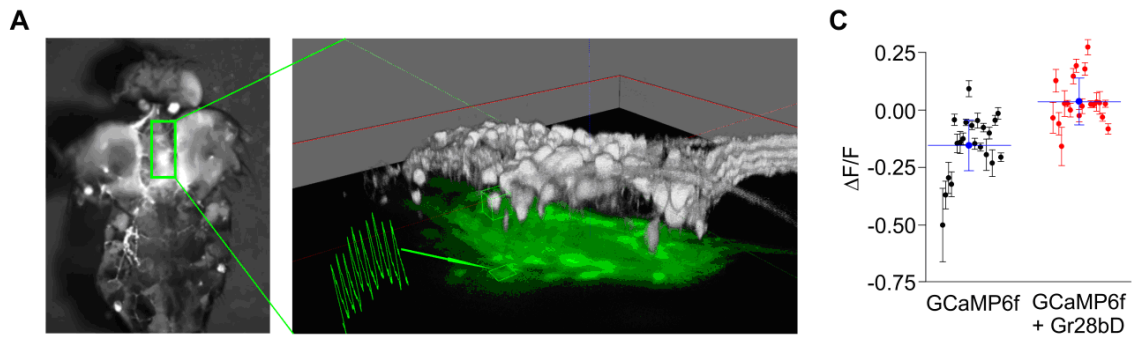


Fig. 1.2. Temperature-dependent modulation of cellular activity by Gr28bD. (A)

Left panel: dorsal view of adult *Drosophila* dissected to expose ventral nerve cord motor neurons to saline bath. Right panel: composite image of epifluorescence (green on black) and two-photon 3D reconstruction (gray scale) of abdominal neuromere neurons expressing GCaMP6f. The green trace is an example of single-cell activity, as obtained via epifluorescence from the indicated region of interest. (B) Single-cell fluorescence signals (blue traces) obtained in response to a temperature step (red traces), analyzed by continuous wavelet-transform (spectrogram). Top panel: representative data from control flies expressing only GCaMP6f in motor neurons. Middle and bottom panels: representative data sets illustrating two types of temperature responses in flies expressing GCaMP6f + Gr28bD in motor neurons. (C) Change in average fluorescence between low and high temperature. $\Delta F/F$ was calculated as $(F_H - F_L) / F_L$, where F_L and F_H are the average fluorescence intensities (in arbitrary units) for a given cell, at low and high temperature. Data points are mean \pm SDV ($n = 21$ cells from five flies for GCaMP6f, and $n = 20$ cells from six flies for GCaMP6f + Gr28bD). The blue lines represent mean \pm SDV for each data set. $\Delta F/F = -0.1524 \pm 0.1358$ in control flies and 0.03656 ± 0.10 in GR28bD-expressing flies (unpaired t-test; p-value < 0.00001).

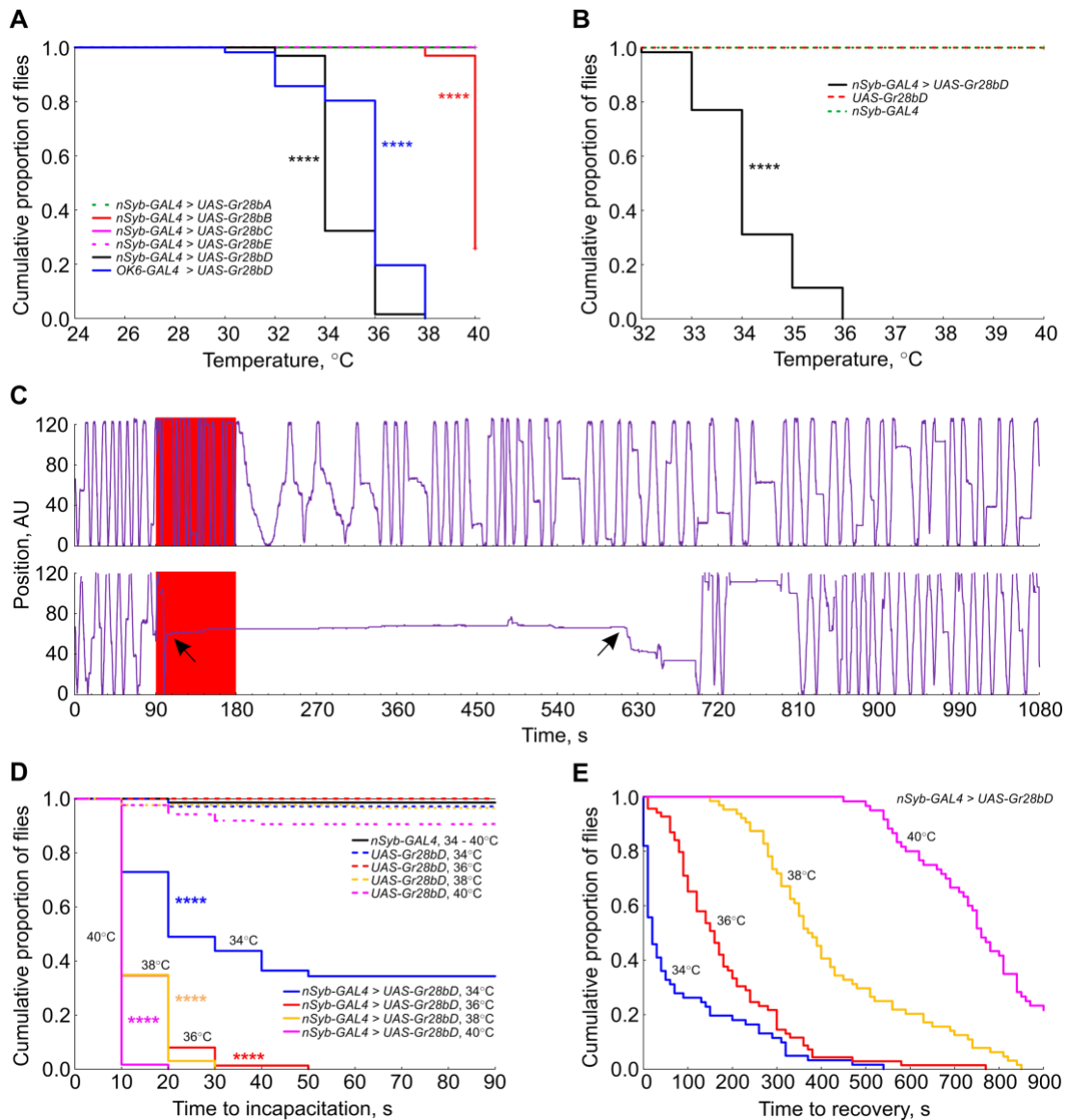


Fig. 1.3. Temperature-dependent modulation of fly behavior by Gr28bD. (A)

Incapacitation by temperature: flies overexpressing GR28b genes had their locomotor activity recorded for 90 seconds at 24 – 40 °C in two-degree steps. The plot shows the cumulative proportion of flies not incapacitated at each temperature. Most flies with pan-neuronal or motor neuron *nSyb* overexpression of GR28bD were temporarily incapacitated at 34 or 36 °C, respectively. Gr28bB overexpression had an effect at the very high end of the tested temperature range. (B) Control and Gr28bD-overexpressing flies were exposed

to 32 – 40 °C in one-degree steps. Most flies overexpressing Gr28bD pan-neuronally were incapacitated at 33 – 35 °C. The heterozygous genetic control flies did not show incapacitation over the tested temperatures. Incapacitation is faster and recovery is slower at higher exposure temperatures. (C) Example position traces of a non-incapacitated fly (top panel) and of an incapacitated fly that recovered (bottom trace). The red area represents the exposure to high temperature and the arrows mark the times of incapacitation and recovery. (D) Time to incapacitation at different temperatures: flies overexpressing Gr28bD and flies heterozygous for the GAL4 driver and UAS-Gr28bD construct were tested. Most flies with Gr28bD pan-neuronal overexpression were incapacitated within 10 seconds at 36, 38, and 40 °C, but it took much longer at 34 °C. Few flies from the control genotypes were incapacitated at the temperatures tested. (E) Time to recovery from incapacitation: flies recovered faster when subjected to lower temperature. In A, B, and D, statistical difference between control and experimental genotypes was determined with a Kaplan-Meier test, $p < 0.000001 = ****$. In each experiment, 60 - 80 flies of each genotype were tested.

Chapter 2

Temperature sensitivity in of Gr28bD orthologs

I performed all the work presented in this chapter, which is original and unpublished.

Abstract

In a previous study, we showed that Gr28bD, a member of the *Drosophila melanogaster* gustatory receptor family, exhibits a non-inactivating, temperature dependent, cation non-specific current, when expressed in *Xenopus laevis* oocytes. Here, we explored the temperature sensitivity of Gr28bD orthologs from five *Drosophila* species (*D. yakuba*, *D. simulans*, *D. pseudoobscura*, *D. willistoni*, and *D. mojavensis*) that inhabit different environments. These orthologs exhibit various temperature sensitivities and current densities in two-electrode voltage clamp (TEVC) experiments. These results identify novel thermosensitive gustatory receptors in *Drosophila* and expand the pool of potential candidates for thermogenetic tools. Investigating these orthologs also provide clues for further structure/function studies aimed at elucidating the molecular biophysics of thermosensation.

Introduction

Thermosensation is an important biological function that relies on ion channels to transduce changes in temperature into electrical signals. In mammals, this role is played by TRP channels (Clapham, 2003; Dhaka et al., 2006; Huang et al., 2006; Patapoutian, 2005; Voets, 2014). Interestingly, some form of thermosensation in *Drosophila melanogaster* fruit flies has been shown recently to rely on a member of the gustatory receptor family, Gr28b (Ni et al., 2013a). The Gr28b gene features alternative splicing

and can produce five isoforms, Gr28bA to Gr28bE. When heterologously expressed in *Xenopus laevis* oocytes, Gr28bD exhibits the properties of a cation non-selective ion channel that starts to activate around 13 °C and responds to temperature with a Q_{10} of ~10 (Mishra et al., 2018). Besides being physiologically important, we have shown that Gr28bD can be used as a thermogenetic tool for extrinsic control of brain activity (Mishra et al., 2018). Ideally, we would want to start with Gr28bD and use it as a basis to derive new proteins with distinct specific properties, such as temperature activation threshold or Q_{10} . For this, we would need to understand the molecular basis of thermosensation of Gr28bD. However, this protein has a currently unsolved structure, and shares no similarity with the relatively well understood TRP channels (Ni et al., 2013a; Robertson et al., 2003).

Here, we are taking advantage of the existing natural diversity of *Drosophila* species, to explore the thermosensitivity of Gr28bD orthologs. We focused on *D. melanogaster*, *D. yakuba*, *D. pseudoobscura*, *D. willistoni*, *D. mojavensis*, *D. simulans*, *D. virilis*, and *D. oleae*. With the exception of *D. virilis* and *D. oleae* orthologs, we found that all these proteins exhibit thermosensitivity, yet they have distinct properties, as tested in TEVC experiments in *Xenopus* oocytes. We also tested these orthologs for their ability to function as thermogenetic tools, by expressing them in *D. melanogaster* fruit flies that were subjected to cellular and behavioral assays, and found a good correlation with their biophysical properties.

Results

Sequence similarity/identity between Gr28bD orthologs. Because Gr28bD is the only Gr28b isoform that exhibits ionic currents with temperature sensitivity, we

performed a BLAST search for proteins that show high sequence similarity to Gr28bD. The search showed high similarity for *D. melanogaster* Gr28bD orthologs in multiple *Drosophila* species, including *D. simulans* isoform X4/E (percentage sequence identity = 98.41%), *D. yakuba* isoform X5/B (95.68%), *D. pseudoobscura* isoform X4 (84.51%), *D. willistoni* isoform B (81.18%), and *D. mojavensis* Dmoj_GI17781 (80.18%). All of these orthologs were tested and exhibited thermosensitivity, as described further. We also tested a Gr28b ortholog with lower sequence similarity, the *D. virilis* isoform X1 (61.2%), which did not produce any current. For comparison, the sequence similarity of Gr28bD with the other isoforms is: Gr28bB 66.28%, Gr28bC 64.22%, Gr28bA 62.50%, and Gr28bE 62.39%.

A sequence alignment of all the tested orthologs and the previously tested Gr28bD isoforms (Mishra et al., 2018) is shown in (Fig.2. 1). All orthologs, as well as the five Gr28b isoforms from *D. melanogaster*, share 90% sequence similarity toward the end of their polypeptide chain (C-terminus). The N-terminus shows variability. Orthologs of Gr28bD in *D. simulans* and *D. yakuba* share more than 90% sequence similarity with Gr28bD from *D. melanogaster*, while *Drosophila mojavensis* shows the least similarity. A map of all Gr28bD ortholog proteins (Fig. 2.2) shows that Gr28bD from *D. melanogaster* and its protein ortholog from *D. simulans* are closest to each other with 98% sequence identity.

A protocol for assessing temperature sensitivity of Gr. Because temperature changes occur on a relatively slow timescale, both physiologically and in thermogenetic experiments, we were particularly interested in the steady-state thermosensitivity of the Gr. Assessing steady-state temperature dependence requires relatively long recording

protocols. To minimize the total recording time and reduce preparation run-down, we designed a voltage clamp protocol that combines a slow temperature ramp (from ~10 to ~40 °C) at a constant voltage (-60 mV) with brief (1 ms) voltage ramps (-60 to 0 mV) inserted to test conductance at different temperatures, as shown in (Fig. 2.3, V-T-ramp). We established that this ramp speed produced relatively steady-state currents, as indicated by a small hysteresis between the up and down phases of an up-down temperature ramp (data not shown). The actual voltage deviated only a few mV from the prescribed value.

Thermosensitivity properties vary between Gr28bD orthologs. The Gr current as a function of temperature is shown in Fig. 2. 4, panel A, for the six orthologs and for uninjected oocytes. The same data are shown on a logarithmic scale in panel C. Because the actual temperature can vary slightly between experiments, the current was binned in 2 °C intervals. The (negative) derivative of the current with respect to temperature is shown in panel B, and the Q_{10} of the current as a function of temperature is shown in panel D.

The uninjected oocytes have very little current throughout the tested temperature range (0 uA at 12 °C and -0.2 nA at 36 °C). The Q_{10} value for uninjected oocytes is virtually 1 over the entire range, which means that the endogenous currents have little or no temperature sensitivity. In contrast, *D. mel.* exhibits a robust temperature-sensitive current that starts to activate at around 15 °C and increases exponentially with temperature, reaching approximately 4 nA at 36 °C. According to the logarithmic plot, the rate of current increase with temperature is not constant, being the highest in the range of approximately 15 to 25 °C. Q_{10} starts at 2 at 13 °C, ramps up to a peak of ≈ 12 at 18 °C, and then decreases monotonically to approximately 4 at 34 °C. At the lowest

tested temperature, it appears that the channel produces some constitutively active current.

The other orthologs exhibit a number of interesting differences. Strikingly, the *D. sim.* ortholog generates more than twice the *D. mel.* current, and also has significant current at low temperature. Its Q_{10} peaks at the same temperature as *D. mel.* (18 °C), but it only reaches ~ 6. *D. yak.* generates current with similar properties to *D. mel.*, in terms of average current and Q_{10} , but it seems to be slightly shifted toward higher temperatures.

D. pse. produces significantly less current and exhibits a substantially lower rate of activation, with a Q_{10} that only reaches a peak value of 4 at 22 °C. *D. wil.* also generates relatively little current. However, its activation is dramatically shifted by ~10 °C, with a Q_{10} that reaches a peak value of ~7. Finally, *D. moj.* generates the least amount of current, reaching less than 150 nA at 36 °C. Its Q_{10} steadily increases with temperature but only reaches ~2 at 36 °C.

These results suggest a correlation between the degree of sequence similarity and the biophysical properties. Thus, *D. sim.* (98.41%) and *D. yak.* (95.68%), which are the two orthologs that are the most similar in sequence to *D. mel.*, generate the most robust current, with relatively similar rate of activation. The other three orthologs have significantly lower similarity scores and exhibit the greatest differences: *D. pse.* (84.51%) has a significantly lower Q_{10} , *D. wil.* (81.18%) has a strong shift with temperature, and *D. moj.* (80.18%) generates very little current with shallow activation. We currently do not have any information on expression levels, so the differences in current amplitude between orthologs may be partially caused by differences in expression.

Conductance properties change with temperature. The previous results make it clear that the Gr current changes with temperature. However, the current is a product of several factors: the number of channels, the unitary conductance, the open probability, and the driving force. The open probability is the obvious source of temperature sensitivity, but what about the driving force? Indeed, all these orthologs exhibit some degree of temperature dependence in their reversal potential (V_{rev}), as illustrated in Fig. 2.5 (V_{rev}). Interestingly, the background current in uninjected oocytes also exhibits strong temperature dependence. At high temperatures, all orthologs but *D. moj.* have similar V_{rev} , but they spread at lower temperatures. The V_{rev} estimates for *D. moj.* are not reliable, because the current is small compared to the background current. However, the estimates should be quite reliable for *D. mel*, *sim*, *yak*, and *pse*, at temperatures ≥ 20 °C. In particular, *D. sim*, and *D. mel*, have strikingly dissimilar trends. Considering that the Gr channel is cation non-selective, with comparable Na⁺ and K⁺ selectivities (Mishra et al., 2018), this temperature dependence suggests that the relative permeability changes with temperature. A simple temperature effect according to the Nernst equation would not explain the magnitude of the observed trend.

A mutation that results in a nonfunctional channel. By comparing the Gr28bD sequence with the ortholog proteins, we identified a sequence of four residues of amino acids (IEQQ) right next to the second putative transmembrane domain (Fig.2. 6) that we considered to be a good candidate as a site of ion permeation and thermosensitivity. These residues are conserved among the conductive ortholog proteins and contain the negatively charged amino acid glutamate, which is not found in any other Gr28b nonconductive isoforms. We hypothesized that this glutamate amino acid may interact

with cations in the channel. We performed single and double mutations of glutamate to alanine and checked their effect on the magnitude of current compared to the wild type. We found that IEQQ to AAAA mutation of the Gr 28bD of *D. melanogaster* resulted in a non-functional channel, when expressed in *X. laevis* oocytes (data not shown).

Discussion

In a previous study, we showed that Gr28bD exhibits a non-inactivating, temperature dependent, cation non-specific current, when expressed in *Xenopus laevis* oocytes (Mishra et al., 2018). To understand the structure-function relationship of Gr28bD, we explored the temperature sensitivity of Gr28bD orthologs from five *Drosophila* species (*D. yakuba*, *simulans*, *pseudoobscura*, *willistoni*, and *mojavensis*) that inhabit different environments. These species populate wide range of ecosystems from Sub-Saharan tropical Africa (*D. yakuba*), Caribbean islands (*D. willistoni*), North America (*D. pseudoobscura*) to Mojave desert (*D. mojavensis*), and cosmopolitan species *D. melanogaster* and *D. simulans*. The selected species have ortholog proteins that share 80 to 98% amino acid sequence identity with Gr28bD.

TEVC experiments revealed different degrees of temperature sensitivity among orthologs of Gr28bD, which correlate with the degree of sequence similarity between these proteins and Gr28bD from *D. melanogaster*. The ortholog of Gr28bD from *D. sim* generates a high amount of current relative to Gr28bD from *D. mel.*, and the current starts at lower temperature (18 °C). *D.yak.* produces a current that is as big as the *D. mel.* current, although the onset is shifted toward higher temperatures. The current generated by the *D. pse.* and *D. will.* orthologs was significantly lower, with an onset at higher temperatures. *D. moj.* produced the least current among all orthologs, which correlates

with its lowest sequence similarity score. Our results confirm the hypothesis of similar orthologs of Gr28bD may have temperature sensitivity, as well as unique temperature properties of these orthologs considering the environmental diversity of the flies.

Additionally, when these orthologs are expressed in *Drosophila* motor neurons, along with a genetically-encoded calcium sensor (GCaMP6f), Gr28bD orthologs exhibit unique changes in the firing pattern of individual cells, in a temperature-dependent fashion.

Moreover, flies over-expressing GR28bD orthologs exhibit different temperature-dependent behavior. The trend in temperature sensitivity of Gr28b orthologs observed in the TEVC experiments is also found in the imaging and behavioral data.

Also, our attempt for mutation in Gr28bD resulted to a non-conductive channel upon expression in *Xenopus* oocytes. The permeability and selectivity of a given channel is dictated by specific amino acid sequences within the pore that discriminate ions based on various properties such as size, hydration, and charge. Our selected residues contain a negative charge amino acid and may play role in ionic interaction of the protein. This result might explain the role of this glutamate residue in channel function. However, further investigation of the level of expression of this mutant channel needs to be done to confirm our hypothesis. We are working on developing a quantitative method for assessing the expression of Gr28b protein in the membranes of oocytes. Further orthologues-sequence guided mutagenesis will help with understanding the molecular mechanism of Gr28b thermosensitivity and the development of new molecular thermosensors.

Overall, the results presented here show novel thermosensitive gustatory receptors in *Drosophila sp.*, expanding the pool of potential candidates for thermogenetics tools.

They also provide clues for further structure/function studies aimed at elucidating the molecular biophysics of thermosensation.

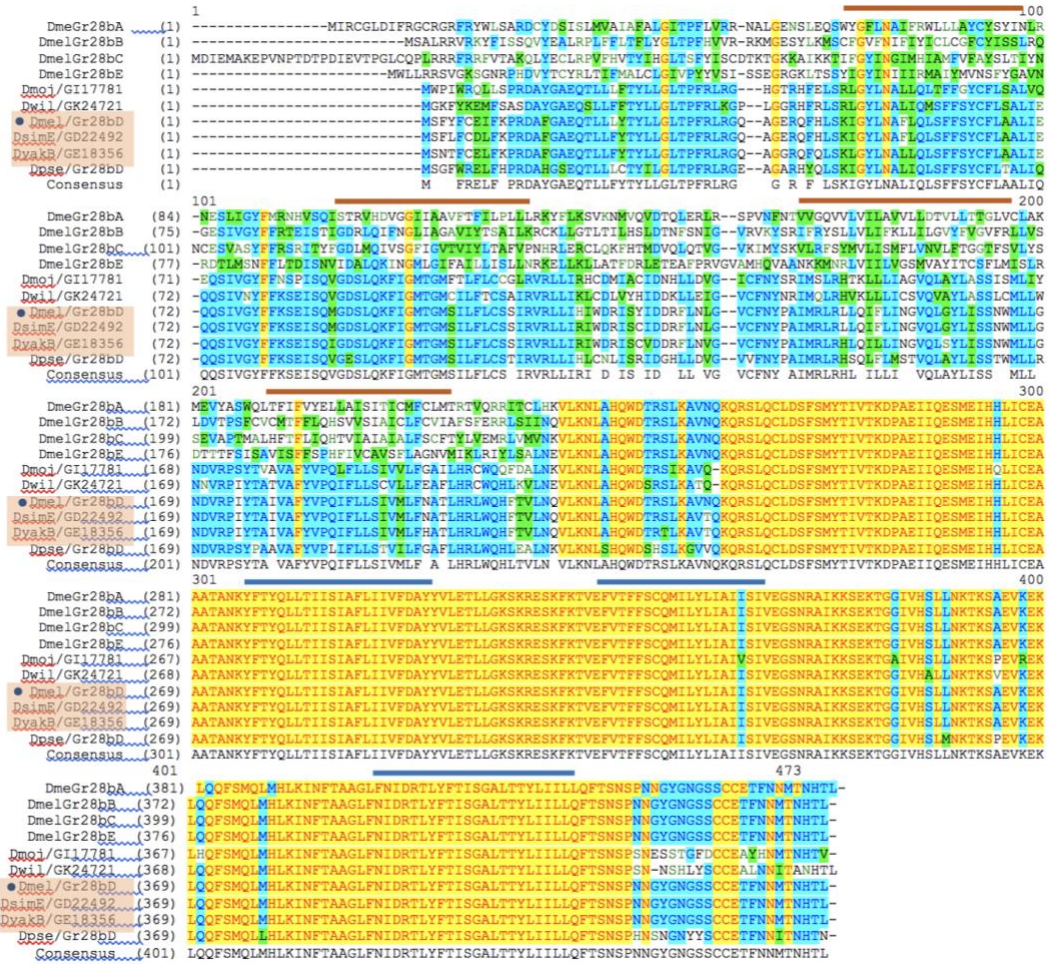


Fig. 2.1. Sequence alignment of Gr28b isoforms and Gr28bD orthologs. The highlights show sequence conservation, with *D. melanogaster* Gr28bD as the reference. The consensus is shown with the threshold of >95% amino acid similarity. All orthologs and Gr28 isoforms show more than 90 percent sequence similarity in their C-terminus. The solid bars represent the putative 7 transmembrane domains.

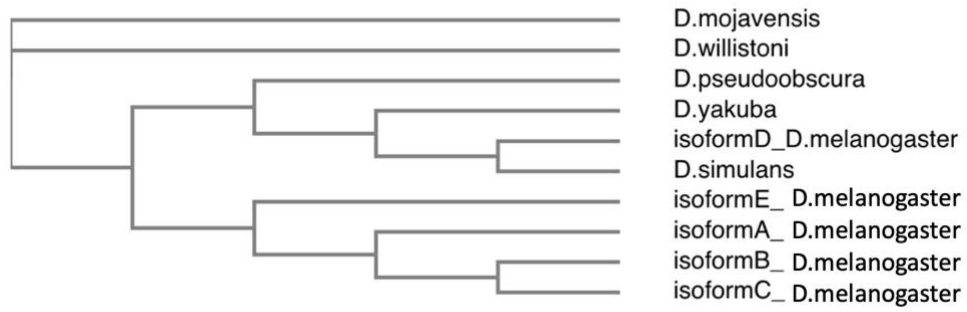


Fig. 2.2. Phylogenetic tree of Gr28b isoforms and Gr28bD orthologs. Gr 28bD from *D. melanogaster* and its ortholog from *D. simulans* share the maximum identity to each other. *D. mojavensis* is more distantly related, with only 80% identity to *D. melanogaster*. Gr28bD shares less similarity with its isoforms A, B, C, and E. The Gr28bD orthologs are from different species of *Drosophila* and occupy a wide variety of habitats.

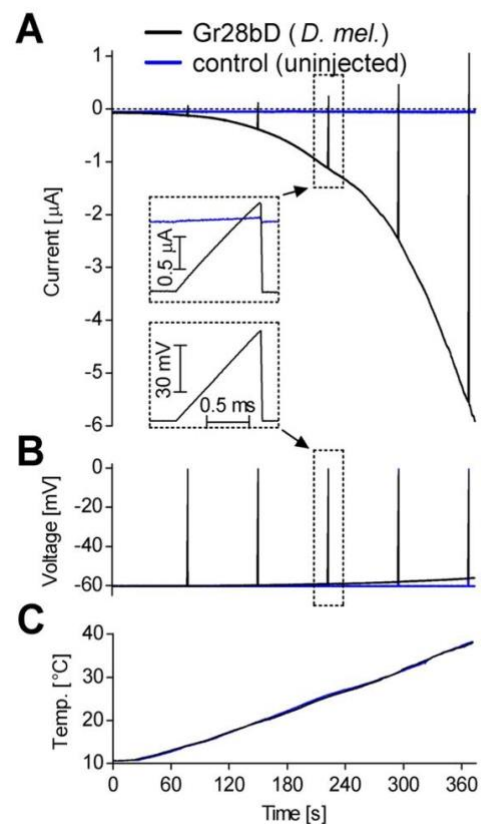


Fig. 2.3. Testing temperature sensitivity with a slow temperature ramp protocol. The temperature is slowly (~ 6 minutes) ramped up (~ 10 to ~ 40 $^{\circ}\text{C}$), under constant voltage (-60mV) to test the steady-state changes in conductance with temperature. Brief (1 ms) voltage ramps (from -60 to 0 mV) are interspersed within the temperature ramp, to test the steady state changes in ionic selectivity at different temperatures. Uninjected oocytes were used as control.

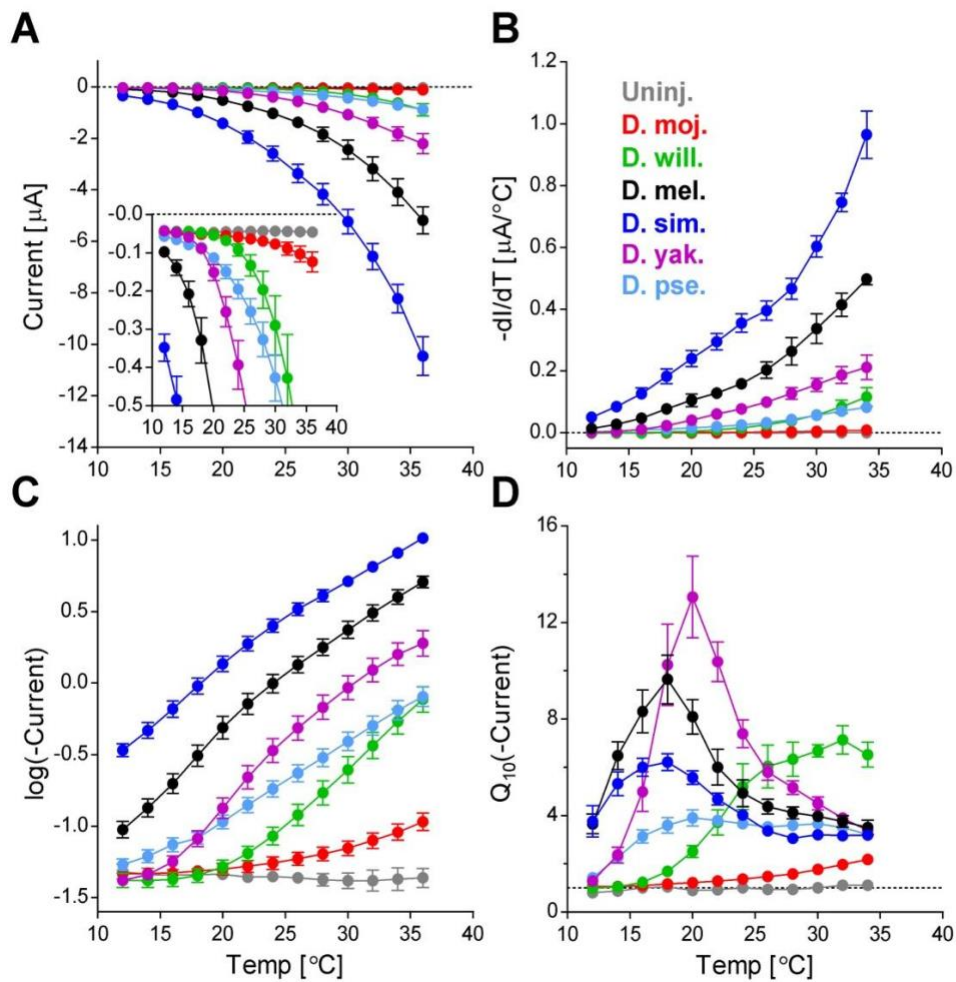


Fig.2. 4. Temperature-sensitive properties of Gr28bD orthologs. The average steady-state current vs. temperature is shown in panel A, for Gr28bD, its five orthologs, and uninjected oocytes (control). The uninjected oocytes have very little current, whereas Gr28bD and most of the orthologs have large currents. The exception is *D. moj.*, which exhibits small current, but significantly greater than the control. The other panels show the derivative of current with temperature (B), the logarithm of current (C), and Q_{10} (D). Interestingly, the orthologs exhibit a wide range in their thermosensitive properties (compare *D. sim.* with *D. moj.*).

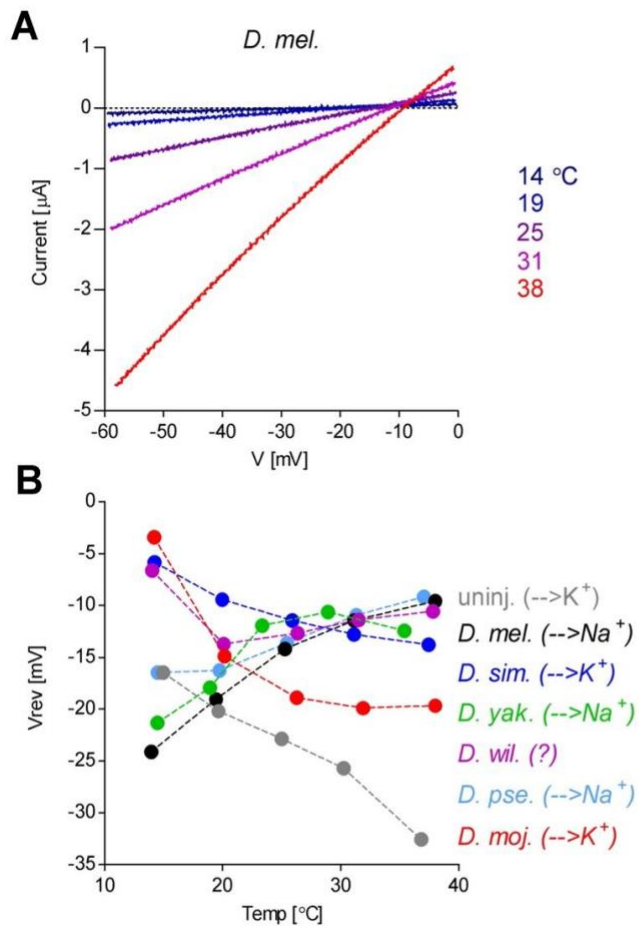
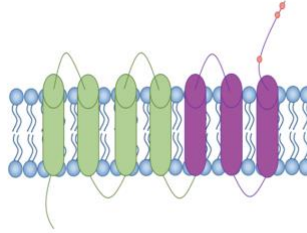


Fig. 2.5. The effect of temperature on ionic selectivity. The current generated by the channel in response to a brief voltage ramp at different temperatures (see Fig.2. 3) is shown in panel A for *D. mel.* (representative recording). The reversal voltage is this current is plotted vs. temperature in panel B, for Gr28bD, its five orthologs, and uninjected oocytes (representative recordings). Interestingly, the reversal voltage exhibits a significant degree of temperature dependence, with notable differences between the orthologs (e.g., *D. sim.*

vs. *D. mel*), particularly at low temperature. This dependence suggests a change in ionic selectivity with temperature.



| | | |
|-------------------------|--------------------------------------------------------------------------|-----|
| D.mojavensis | RLR--GH-GTRHFELSRIGYLNALLQLTFPGYCPLSAIV- EQE SVIGYFFNSPIISQVGDS | 89 |
| D.willistoni | RLK--GPLGGRHFRLSRLGYLNALIQMSFFSYCPLSAI I -EQQSVINYPFKSEISQVGDS | 90 |
| D.pseudoobscura | RLR--GEAGARHYQLSKIGYLNALIQLSFFSYCPLTA I -QQQSVIGYFFKSEISQVGES | 90 |
| D.yakuba | RLR--GQAGGRQFQLSKIGYLNALLQLSFFSYCPLAA I -EQQSVIGYFFKSEISQIGDS | 90 |
| isoformD,D.melanogaster | RLR--GQAGERQFHLSKIGYLN AFLQLSFFSYCPLAA I -EQQSVIGYFFKSEISQMGDS | 90 |
| D.simulans | RLR--GQAGERQFHLSKIGYLN AFLQLSFFSYCPLAA I -EQQSVIGYFFKSEISQMGDS | 90 |
| isoformE, | YVS-ISSEGRGKLTSSYIGYINIIIRMAIMVNSPYGAV-NRDTLMSNPF LD ISNVIDA | 95 |
| isoformA, | LVR-RNALGENSLEQSWYGF LN AIFRWLLAYCVSYINL-RNESLIGYFMRNHVSQISTR | 102 |
| isoformB, | HVV-RRKMGESYLKMSCFGVFNIFIYICLCGFCYIS-SLRQGESIVGYFFRTEISTIGDR | 93 |
| isoformC, | YISCDTKTGKKAIKKIFGYINGIMHAMFVFPAYSLTIYNNCESVASYFFRSRITYFGDL | 120 |
| | : * : * : * : : : : : : : : * : : : : | |

Fig. 2.6. Sequence alignment of part of the polypeptide chain in Gr28b isoforms and Gr28bD orthologs. An IEQQ motif is present in current-producing Gr28b proteins, and we reasoned that it may have a functional role in the channel. Indeed, mutating IEQQ to AAAA eliminated the current.

Chapter 3

A model-driven analysis of thermosensation mechanisms in *Drosophila* thermosensitive gustatory receptors

This chapter is unpublished and reflects a collaboration with the Sukharev lab at U. Maryland – College Park. I performed the bioinformatic analysis of orthologs and the sequence alignment to identify targets for mutagenesis studies, based on the molecular modeling performed in the Sukharev lab. Also, I performed all the TEVC experiments and analyzed the data. The molecular modeling of Gr28bD was done by Drs. Andriy Anishkin and S. Sukharev. Elissa Moller contributed to the mutagenesis work.

Abstract

Drosophila gustatory receptor Gr28bD is a temperature sensitive cation - non selective ion channel. This protein contains 443 amino acids and is predicted to have seven transmembrane segments. However, its molecular structure is not known. Although it is thermosensitive, Gr28bD lacks any homology with all known TRP channels, and questions regarding its overall structure, ion permeation pathway, and temperature sensing domains remain unanswered. To address these issues, we took advantage of the solved tetrameric cryoEM structure of Orco, a distantly related olfactory co-receptor, to generate a set of models for *D. melanogaster* Gr28bD and several of its orthologs. Based on these models, we then generated several mutants in *D. melanogaster* Gr28bD, and investigated them with the TEVC technique. The results illustrate differential sensitivity to temperature in these mutants, and the correlations observed between residue

substitution and channel function point out to the protein segments responsible for the thermosensitive phenotype.

Introduction

The gustatory receptor Gr28bD, a protein involved in temperature avoidance behavior in *Drosophila melanogaster*, has recently emerged as a novel thermogenetic tool (Mishra et al., 2018). We have previously demonstrated that Gr28bD can be expressed in *X. laevis* oocytes, where it forms a cation non-selective ion channel. Moreover, Gr28bD can be used to control fly behavior, when expressed in neurons. To generate variants with distinct and optimized thermosensitive properties, we have previously mined the *Drosophila* family and found five thermosensitive orthologs. Although sequence differences between these orthologs hint at structural and functional domains, the structure of Gr28bD remains unknown, which makes it difficult to understand the molecular mechanisms of thermosensitivity, and to engineer new variants. Although it is thermosensitive, Gr28bD lacks any homology with all known TRP channels, and questions regarding its overall structure, ion permeation pathway, and temperature sensing domains remain unanswered.

To address these issues, we took advantage of the solved tetrameric cryoEM structure of Orco, a distantly related olfactory co-receptor. Insect olfactory receptors (ORs) have a heteromultimeric structure that is composed of OR subunits and the co-receptor Orco. The Orco protein was originally found in *Drosophila* and, unlike other olfactory receptors, is super conserved across insects (Missbach et al., 2014; Vosshall et al., 2000). The necessity of Orco for olfaction in *Drosophila* is confirmed through studies that showed that ORs' localization, assembling, and function are dependent on Orco

(Benton et al., 2006b; DeGennaro et al., 2013; Larsson et al., 2004). Some wingless insects that are evolutionarily older than winged insects lack ORs but have Orco, which suggests that ORs may have evolved from Orco (Missbach et al., 2014).

Orco can form homomers or heteromers with ORs (Stengl & Funk, 2013). It has been suggested that both the Orco homomer and the Orco-OR heteromer function as cation channels. A detailed structure of the Orco-OR oligomer does not exist yet, but the cryo-EM structure of the Orco homomer has been recently solved by the Ruta lab at the Rockefeller University (Butterwick et al., 2018). The homotetrameric channel structure of Orco contains a central pore, formed by several transmembrane helices, and a small intracellular anchor domain that provides inter-subunit interactions. It is suggested that the heterotetrametric Orco-OR structure forms through the interaction of OR with the pore and the anchor domain.

Here, we used the Orco structure as a scaffold to generate a set of models for the *D. melanogaster* Gr28bD. We identified three C-terminal transmembrane domains that form the multimerization interfaces and contribute to the conductive pore with an extracellularly located hydrophobic gate (Fig.3. 1). The most encouraging predictions of putative thermosensitive domains come from the modeling of Gr28bD paralogs from closely related species *D. yakuba*, *D. simulans*, *D. pseudoobscura*, and *D. mojavensis*, which live in different habitats and have adapted to different temperature ranges. We provide experimental data that illustrate differential sensitivity to temperature in these paralogs, and we analyze correlated substitutions in the structural models that suggest the protein segments responsible for the thermosensitive phenotype. To better understand the pore structure of Gr28bD and to identify the sites that may be involved in ionic

selectivity and temperature sensitivity of this protein, we mutated several residues, as suggested by our computational model.

Results

Computational modeling Gr28bD and its orthologs after Orco. The cryo-EM structure of Orco revealed that exclusive expression of Orco in the absence of OR results in a homotetrameric cation channel. The subunit contains seven transmembrane domains (S1 to S7), with S7 forming the pore. The S7 segment is divided into two helices: S7a is a cytoplasmic segment that is connected to the transmembrane segment S7b by a 15-residue β -hairpin loop. The S7a is involved in the structure of anchor domain and S7b is involved in the pore structure and ionic selectivity of the channel (Butterwick et al., 2018).

Like Orco, the Gr28bD modeled structure denotes a homotetrameric protein (Fig. 3.1, panel A and B). According to this model, Gr28bD has seven transmembrane segments, with the last three transmembrane helices forming the pore. Molecular dynamics simulations show that, when embedded in a membrane bilayer, the gate is at the extracellular side of the channel and is connected to the cytoplasmic side by water “sleeves” between transmembrane and cytoplasmic domains (Fig.3.2.)

Pocket structures are cavities on the surface or in the interior part of a protein that provides a space for binding ligands or water in thermosensitive proteins. Here we believe that Gr28bD possess a pocket structure that play role in interaction with water. This structure contains hydrophilic amino acids.

We also identified several divergent residues among Gr28bD orthologs, by overlapping their structure (Fig.3.1, panel C and D green residues). The existence of polar amino acids like threonine and serine (Fig.3.1, purple residues) suggests that they may contribute to the pocket structure of these proteins and play a role in thermosensitivity. The pocket structure provides a space for water molecules to be trapped and interact with the hydroxyl groups in these residues, causing a conformational change in the structure of the protein upon facing water. Also, when comparing orthologs, we hypothesized that the higher thermosensitivity of *D. melanogaster* relative to *D. mojavensis* is the result of *D. melanogaster* having a higher fraction of polar residues in the non-polar regions of the membrane.

Screening Gr28bD mutants, as suggested by the computational model. Once we modeled Gr28bD after the Orco cryo-EM structure, we were able to determine which structural parts were divergent between the orthologs (Fig.3.1 panel C and D green residues). To investigate how individual amino acid residues contribute to channel topology, pore structure, and thermosensitivity, we performed several mutations in Gr28bD and examined the resulting channel properties via TEVC. To design these mutations, we were guided by the sequence differences and similarities in the last transmembrane segment, across the orthologs (Fig. 3.3).

We categorized the mutations into two main groups: mutations that are expected to alter the pore structure and the ionic selectivity of the channel, and mutations that are expected to modify the thermosensitivity of the protein. Because our model suggests that the last three transmembrane domains are involved in pore structure and ionic selectivity, we introduced all the mutations close to the C-terminus (Fig.3. 4).

Serine 400 and threonine 404 are located within the last transmembrane segment, and these types of amino acids, due to their polarity, are known to interact with water molecules in thermosensitive proteins. Thus, we hypothesized that mutating these polar residues to non-polar ones would result in a loss-of-function phenotype, due to the reduction in the number of water molecules within the protein structure. As it turns out, T404V maintains temperature sensitivity but exhibits reduced conductance, while S400A remains similar to the wildtype channel phenotype.

I409A, F413A, and L410A substitutions were designed for a gain-of-function effect, with the expectation that the mutant channel would have an increased open probability. According to our TEVC data, the F413A mutation made the channel strongly temperature sensitive, overall increasing macroscopic conductance. However, the I409A mutation resulted in a much smaller current (~five fold), while the L410A mutation eliminated the current.

Two mutants were expected to change the selectivity of the channel from cationic to anionic: the single K mutant T394K and the double K mutant T394K+Q412K. The experimental data from these two mutants indicate a significant effect on the current magnitude, but further experiments remain to be performed to establish the exact contributions of different ions.

The I409C single mutation and the I408C+T406C double mutation were designed to probe the packing of these residues. The idea is that if these residues are located in different helices but in close proximity to each other, then the channel can be locked in either an open or closed state when these residues are replaced by cysteine. When the channel is treated with oxidizing agents, the cysteine sulfhydryl groups can form

disulfide bridges and lock the channel in that conformation. Our results show that both mutations made the channel less conductive, although the effect in the single cysteine mutation was rather small. Dithiothreitol (DTT) was added to the external solution during the TEVC recording, expecting that DTT would reduce and break possible disulfide bridges in the cysteine mutants and cause conformational changes in the channel. Adding DTT increased the current (Fig.3. 5).

Thermosensitivity properties of Gr28bD mutants. Fig.3. 3, panel A compares the thermosensitivity of currents generated by the above mutants, relative to the wild-type Gr28bD and uninjected oocytes. The same data are shown on a logarithmic scale in panel C. The (negative) derivative of the current with respect to temperature is shown in panel B, and the Q_{10} of the current as a function of temperature is shown in panel D. The loss-of-function mutants T404V and S400A produced current throughout the tested temperature range. However, the current generated by T404V was less than 2 μ A. The gain-of-function mutant F413A generated a large current throughout the tested temperature range. However, the mutants I409A and L410A decreased the current substantially. The T394L mutation shows temperature sensitivity with a current that resembles the wild-type channel. The cysteine mutant I409C generated ~ 3 μ A of current, while the double cysteine mutant I408C+T406C generated less than 2 μ A. Subsequent treatment with DTT, to break the disulfide bonds, show a significant increase in current (Fig.3. 5).

Discussion

We modeled here the Gr28bD after the Orco cryo-EM structure. Our model supports a homotetramer structure for Gr28bD, and we propose that the last three transmembrane

segments are involved in pore structure and ionic selectivity of Gr28bD. Screening Gr28bD mutants provided information about the contribution of individual amino acid residues to the protein structure. Our results showed that some mutations confirmed our structural hypotheses and can guide future studies aimed at understanding the biophysics of thermosensation in Gr28bD and its orthologs.

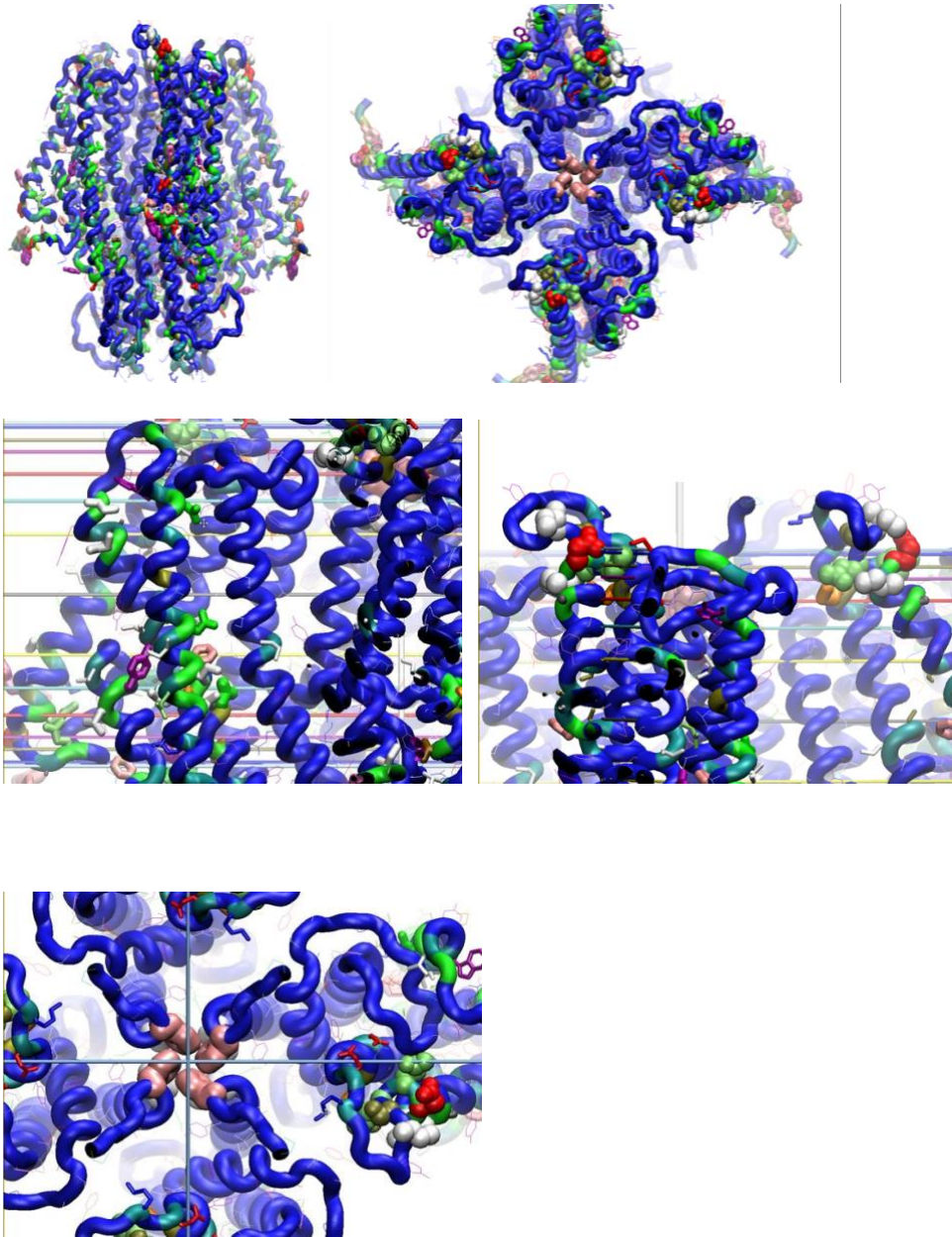


Fig. 3.1. Overlapped homology models of *D. melanogaster* Gr28bD and its orthologs.

The homology model was created using VMD (Hsin et al., 2008) and IntFOLD4 (McGuffin et al., 2019), following the consensus analysis of predictions from IntFold4, Phyre2, Rosetta, and ITASSER. The model covers residues 1-414, corresponding to residues 1-474 of the Orco template (PDB ID 6c70; Butterwick et al., 2019), as the C-

terminal part after the last (gate-forming) TM helix was not resolved. **(A)**. The transmembrane view of Gr28bD. **(B)**. Top view of Gr28bD. The green residues show the most divergent amino acids among orthologs, while the blue residues identify the conserved ones.

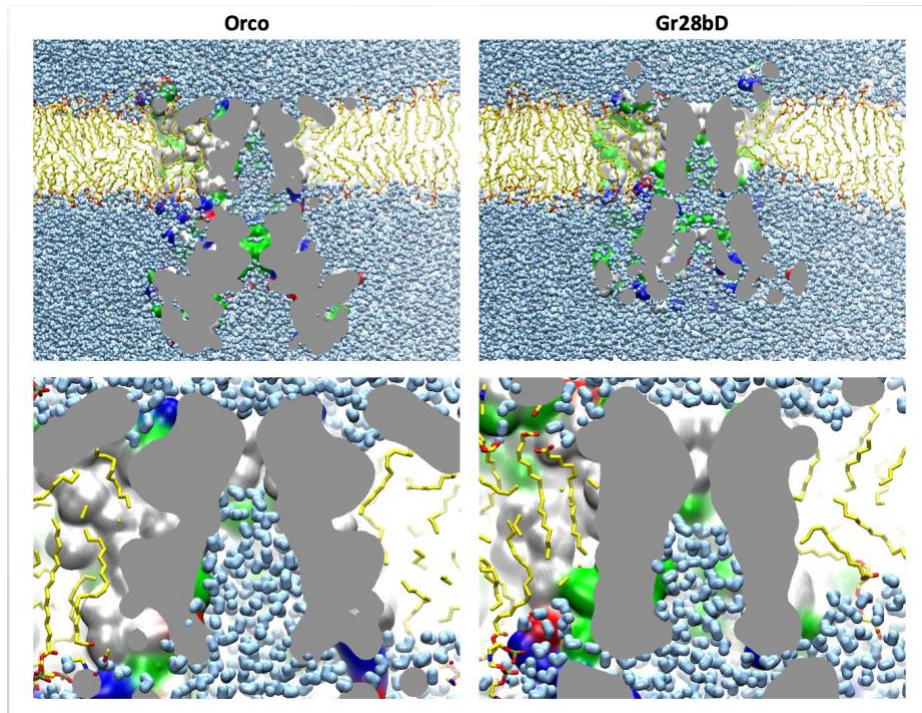


Fig. 3.2. Molecular dynamics simulations indicate dry hydrophobic pore in both structures, consistent with closed state. Both structures were embedded into bilayer patch (70% POPE, 20% POPC and 10% POPS), equilibrated with restrained backbone, and then simulated unrestrained for 10 ns to relax and test the stability of the structures, followed by 1 ns refinement using symmetry-driven simulated annealing. Simulations were performed using NAMD, CHARMM36 force field, TIP3P water, PME electrostatics with 12 Å cutoff, as NPT ensemble in a flexible simulation cell. The snapshots of the cross-section through the channels taken at the last step illustrate that the

gate at the extracellular side of the channel (top) is devoid of water (cyan), while the channel chamber is fully hydrated and connected to the cytoplasmic bulk by water “sleeves” between TM and cytoplasmic domains.


| | | |
|-----------|-----|------------------------------------------------------------------------------------|
| D. Mel | 301 | TLLGKSKRESKFKTVEFVTFPFSCQMILYLIAIISIVEGSNRAIKKSEKTGGIVHSLLNKT |
| D. Sim | 301 | TLLGKSKRESKFKTVEFVTFPFSCQMILYLIAIISIVEGSNRAIKKSEKTGGIVHSLLNKT |
| D. Yak | 301 | TLLGKSKRESKFKTVEFVTFPFSCQMILYLIAIISIVEGSNRAIKKSEKTGGIVHSLLNKT |
| D. Wil | 300 | TLLGKSKRESKFKTVEFVTFPFSCQMILYLIAIISIVEGSNRAIKKSEKTGGIVHALLNKT |
| D. Pse | 301 | TLLGKSKRESKFKTVEFVTFPFSCQMILYLIAIISIVEGSNRAIKKSEKTGGIVHSLMNKT |
| D. Moj | 299 | TLLGKSKRESKFKTVEFVTFPFSCQMILYLIAIIVSIVEGSNRAIKKSEKTGAIVHSLLNKT |
| consensus | 301 | TLLGKSKRESKFKTVEFVTFPFSCQMILYLIAIISIVEGSNRAIKKSEKTGgIVHsLlNKT |
| | | 394 400 405 409 413 ↓ ↓ ↓ ↓ ↓ |
| D. Mel | 361 | KSAEVKEKLQQFSMQLMHLKINFTAAGLFNIDRTLYFTTISGALTTYLIILLQFTSNSPNN |
| D. Sim | 361 | KSAEVKEKLQQFSMQLMHLKINFTAAGLFNIDRTLYFTTISGALTTYLIILLQFTSNSPNN |
| D. Yak | 361 | KSAEVKEKLQQFSMQLMHLKINFTAAGLFNIDRTLYFTTISGALTTYLIILLQFTSNSPNN |
| D. Wil | 360 | KSVEVKEKLQQFSMQLMHLKINFTAAGLFNIDRTLYFTTISGALTTYLIILLQFTSNSPSN |
| D. Pse | 361 | KSPEVKEKLQQFSMQLHLKINFTAAGLFNIDRTLYFTTISGALTTYLIILLQFTSNSPHN |
| D. Moj | 359 | KSPEVREKLHQFSMQLMHLKINFTAAGLFNIDRTLYFTTISGALTTYLIILLQFTSNSPSN |
| consensus | 361 | KSaEVkEKlQqFSMQLmHLKINFTAAGLFNIDRTLYFTTISGALTTYLIILLQFTSNSPnN |
| | |  |
| D. Mel | 421 | GYNGSSCCETFNNMT-NHTL |
| D. Sim | 421 | GYNGSSCCETFNNMT-NHTL |
| D. Yak | 421 | GYNGSSCCETFNNMT-NHTL |
| D. Wil | 420 | N-SHLYSCCEALNNITANHTL |
| D. Pse | 421 | SNGNYYSCCETFNNIT-NHTN |
| D. Moj | 419 | ESSTGFDCCCEAYHNMT-NHTV |
| consensus | 421 | gyngssCCetfnNmT NHTl |

Fig. 3.3. Mutagenesis of key residues with potential functional roles. These residues are located within the last transmembrane domain (purple bar), close to the C-terminus, and are similar among the Gr28bD orthologs. These mutations are expected to provide information on pore structure and the thermosensor domain. The mutants list is I409A, L410A, F413A, T394K, T394K+Q412K, I409C, I408C+T405C, T404V, S400A (only five are marked in the figure).

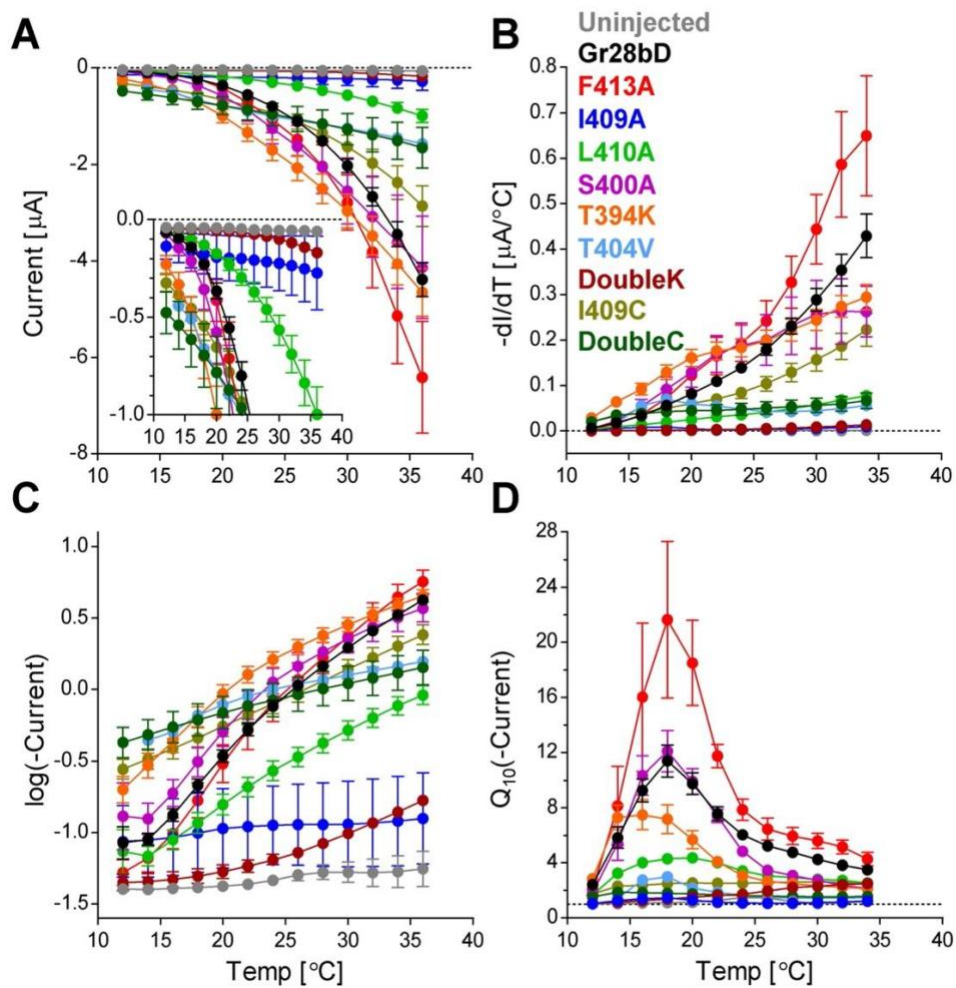


Fig. 3.4. Temperature sensitive properties of Gr28bD and its mutants. The thermosensitive properties for Gr28bD mutants were analyzed as in Fig.2.4 in Chapter 2. The F413A mutant shows strong temperature sensitivity, as denoted by a large peak current and a high Q_{10} .

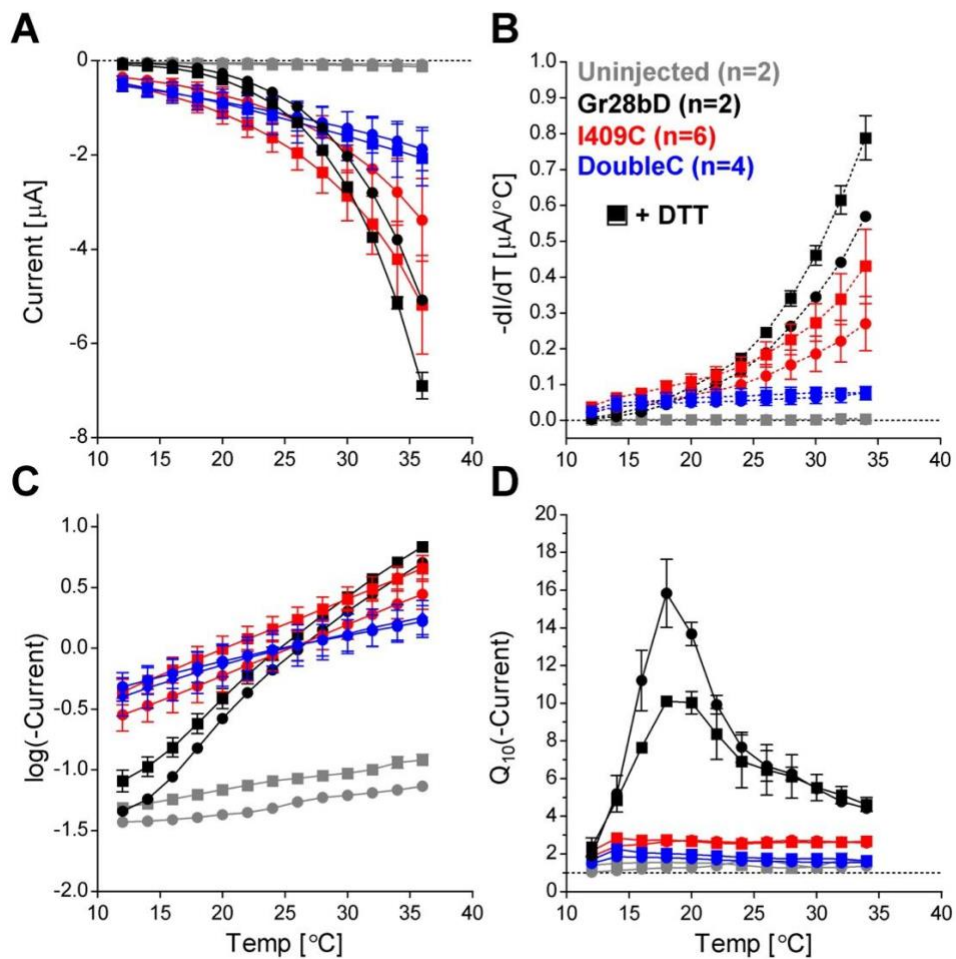


Fig. 5. Temperature sensitivity of single and double cysteine mutants. The data were analyzed as in Fig. 3.3. Interestingly, DTT significantly affected the single cysteine mutant and the Gr28bD wild type channel, but not the double cysteine mutant and the uninjected oocytes.

Chapter 4

Parameter optimization for ion channel models: integrating new data with known channel properties

Adapted from: Navarro, A., Amirshenava, M., Salari, A., Milescu, M., Milescu, L.S. (2021). Parameter optimization for ion channel models: integrating new data with known channel properties. In Quentin Vanhaelen (ed.), *Computational Methods for Estimating the Kinetic Parameters of Biological Systems*, 1st ed. 2021, Methods in Molecular Biology Series, Springer

My contribution: I participated in designing the content and writing and editing the manuscript.

Abstract

Ion channels play a central role in membrane physiology, but to fully understand how they operate, one must have accurate kinetic mechanisms. Estimating kinetics is not trivial when the mechanism is complex and a large number of parameters must be extracted from data. Furthermore, the information contained in the data is often limited and the model may not be fully determined. The solution is to reduce the number of parameters and to estimate them in such a way that they not only describe well the new data but also agree with existing knowledge. In a previous study, we presented a comprehensive formalism for estimating kinetic parameters subject to a variety of explicit and implicit constraints that define quantitative relationships between parameters and describe specific mechanism properties. Here, we introduce the reader to the QuB

software, which implements this constraining formalism. QuB features a powerful visual interface and a high-level scripting language that can be used to formulate kinetic models and constraints of arbitrary complexity, and to efficiently estimate the parameters from a variety of experimental data.

Introduction

Ion channels are membrane proteins that provide a controlled pathway for ions to cross the lipid bilayer of the cellular membrane (Hille, 2001). Structurally, the ion channel molecule contains a pore-forming domain with specific ionic selectivity, and some control elements that open and close the pore with defined sensitivity and timing, in response to specific ligand molecules or physical variables, such as voltage, mechanical tension, or temperature. Functionally, an ion channel is fully characterized by its ionic selectivity and kinetic properties. The kinetic mechanism can be conveniently represented as a Markov model with discrete states that correspond to experimentally and/or statistically detectable molecular conformations (Colquhoun & Hawkes, 1995). The states can represent, for example, the channel closed, open, or inactivated. The transitions between states are quantified by rate constants that follow the Eigen rate theory and can be modulated by the concentration of a ligand or by the magnitude of a physical variable. For example, voltage-gated ion channels have rate constants that can be parameterized as follows:

$$(1) \quad k_{ij} = k_{ij}^0 \times \exp(k_{ij}^1 \times V),$$

where V is voltage, k_{ij} is the rate constant for the transition between states i and j , k_{ij}^0 is the rate at zero voltage, and k_{ij}^1 is a factor that denotes voltage sensitivity. An example of

a kinetic mechanism is shown in Fig. 4.1, as proposed to describe the kinetic properties of voltage-gated sodium (Nav) channels (Kuo & Bean, 1994).

To understand how an ion channel functions, dynamically, at the molecular and cellular levels, one must fully characterize its kinetic mechanism. For this, one has to know the number of states and their connectivity (the “structure”, or “topology”), and the parameters that quantify the rate constants and their sensitivity to external factors, such as expressed by Eq. 1. Several decades of ion channel research have seen the development of powerful parameter estimation algorithms that extract the rate constants for a given topology from a variety of experimental data types, such as single channel or whole cell voltage-clamped currents (Ball et al., 1989; Celentano & Hawkes, 2004; Colquhoun & Sigworth, 1995; Csanády, 2006; Epstein et al., 2016; Gurkiewicz & Korngreen, 2007; Hawkes et al., 1992; Horn & Lange, 1983; Menon et al., 2009; Milescu et al., 2005; Moffatt, 2007; Qin et al., 1996, 2000; A. Stepanyuk et al., 2014; A. R. Stepanyuk et al., 2011; Venkataramanan & Sigworth, 2002), or current clamp recordings (Milescu et al., 2008).

Generally, parameter estimation algorithms use an optimization engine that explores a multi-dimensional parameter space to find a set of values that best explain the data (Salari et al., 2016). Finding these optimal parameters is not easy for ion channels, because they often have kinetic mechanisms with many states and transitions, which results in a large number of parameters that must be estimated. For example, the Nav model shown in Fig. 4.1 is rather minimalistic, yet it has no less than 64 kinetic parameters! Combined with the stochastic nature of the data and with the inevitable presence of recording artifacts, this many parameters would be very difficult to estimate.

If we cut corners and try to use smaller models, with fewer states and parameters, we may end up with a model that simply has not enough flexibility to describe the operation of the channel in a live cell (Milescu et al., 2010).

However, if we are fortunate enough, we may know something about the channel that can help us not only to reduce the number of parameters to be estimated, but also to guide the optimizer in its search for a solution. For example, we know that Nav channels have four voltage sensors that feature similar voltage sensitivities. Then, we can assume that both the forward rates along the $C_1 > C_2 > C_3 > C_4 > C_5$ pathway and the backward rates along the $C_5 > C_4 > C_3 > C_2 > C_1$ pathway are in the 4:3:2:1 ratio. The same assumptions can be made about the rates connecting the inactivated states $I_7 \dots I_{11}$. We can further assume that the channel obeys microscopic reversibility, which means that for each loop in the kinetic scheme (e.g., $C_1 > C_2 > I_8 > I_7 > C_1$), the product of the rates in the clockwise direction is equal to the product of the rates in the counterclockwise direction. Altogether, these are reasonable assumptions that reduce the number of model parameters from 64 to around 20. Finally, we also know that Nav channels have certain kinetic properties, and these must be reflected in the mechanism. For example, the channel must fully recover from inactivation in 5 – 20 ms, so as to enforce a brief but necessary refractory phase for nerve conduction, yet be ready quickly for the next action potential (Bean, 2007).

How can we integrate new data with everything we already know about the kinetic mechanism? We addressed this question in two recent papers (Navarro et al., 2018; Salari et al., 2018), where we proposed a methodology for extracting kinetic parameters that not only explain new experimental data but also satisfy existing

knowledge. We showed how prior knowledge can be enforced via two types of constraints: linear parameter constraints and behavioral constraints. Linear parameter constraints represent explicit mathematical relationships between model parameters, which include the rate constant parameters k_{ij}^0 and k_{ij}^1 in Eq. 1 and all other parameters or external variables that are needed to describe the experimental data and the recording conditions, such as the number of active channels in the recording. We implemented a unified mechanism that handles both equality and inequality linear parameter constraints, using linear algebra methods that transform the inter-dependent parameters of the model into a reduced set of independent parameters that are then optimized (Salari et al., 2018). Linear relationships can be used to implement a variety of constraints, such as scaling one rate to another, parameterizing allosteric relationships, enforcing microscopic reversibility, etc.

In contrast to linear relationships, behavioral constraints represent either specific model behaviors that result from implicit parameter relationships, or explicit parameter relationships that cannot be implemented via the linear algebra method (Navarro et al., 2018). For example, one may wish to enforce an estimated parameter to take values in a specific range. Although this constraint is both explicit and linear, it cannot be implemented via the linear constraint-type mechanism. As another example, one may want to enforce a set of parameters that produce a model with a specific maximum open probability. This constraint is implicit, in the sense that a mathematical relationship cannot be formulated between model parameters, at least not easily and not in the general case.

These constraints that cannot be handled by the linear algebra mechanism can be enforced by calculating a penalty that represents the degree by which the model deviates from that constraint, and then adding that penalty to the cost function that measures the error between the data and the prediction of the model (e.g., the sum of square errors or the likelihood). As the optimizer minimizes a cost function that now includes the penalty for behavioral constraints, it will generate a model that will not only fit the data but will also satisfy all the prior knowledge, formulated as a combination of linear parameter constraints and behavioral constraints. An interesting distinction is that linear parameter constraints are “hard” constraints that are implemented exactly, whereas behavioral constraints can be implemented with a certain degree of flexibility. Another difference is that linear parameter constraints reduce the number of free parameters (one for each equality relationship), whereas behavioral constraints effectively reduce the search space.

This chapter is meant as a companion to our previous studies (Navarro et al., 2018; Salari et al., 2018), where we presented extensively the mathematical and computational formalism for estimating ion channel kinetics with prior knowledge. The algorithms described there have been implemented in our freely available software, QuB – the MLab edition (Navarro et al., 2015). Here, we focus on demonstrating the practical aspects of using the QuB software to define model constraints and estimate kinetic parameters. To make it simpler for the reader, we use the same examples that were used in (Navarro et al., 2018), where we explained the required calculations step-by-step, using detailed numerical examples.

Materials

Computer. You need a PC running a Windows version compatible with the QuB software (XP, 7, 8, or 10). QuB has no special requirements in terms of computer hardware, but computation speed is commensurate with the characteristics of the processor. As QuB can parallelize the computation, a multi-core machine is recommended.

Methods

Install the QuB software. Go to the QuB website (<https://mileskulabs.org/qub.html>) and follow the instructions for how to install QuB. Download the example files that will be used in this tutorial (data file CCOC_Sim.qdf, model files CCOC_Sim.qmf, CCOC_Fit.qmf, and CCOC_FitStart.qmf, and library file Constraints.slf). You will also find materials that describe the scripting language that will be used to implement the behavioral constraints. If you encounter difficulties during the installation process, given the existing variety of Windows versions and user configurations, contact the authors for assistance.

Set up the modeling interface in QuB. For convenience, QuB has a number of predefined graphical user interfaces, each displaying a layout of windows appropriate for a given task – in this case, modeling the kinetic mechanism of ion channels. These predefined interfaces can be further customized, and new ones can be created. To turn on or off a window, go to Main Menu > View and check or uncheck that window. By default, QuB starts in a layout mode where windows are mutually resizable (to switch, select Main Menu > Interface > Floating windows). In this mode, to change the size of a window, use the spacer bar between that window and the adjacent one. To reposition a window, left-click on the caption bar of that window, hold the mouse button down, and

move the mouse around. A rectangle will become visible to indicate where the window will be positioned when you release the mouse button.

For this demonstration, select the Modeling interface and customize it as shown in Fig.4. 2, with the Data, Model, Scriptlets, Graph, and Report windows visible (your windows will be empty until you load the content, as explained in the next sections). The Data window is where we load the data that we want to fit. The Model window is where we construct the ion channel kinetic mechanism and define the linear parameter constraints. The Scriptlets window contains user-defined snippets of code (“scriptlets”), which will be used here to implement the computation of behavioral constraints. The Graph window provides a simple way of displaying curves and other graphics, and it will be used here by the optimization engine to show the convergence of the fit. Finally, the Report window is a text interface used by the optimizer (and other functions) to communicate status and performance and to display results.

Prepare the data for fitting. QuB can handle a number of data file formats, including its own native files with extension “.qdf” (and the older format “.ldt”), Molecular Devices (Axon) pClamp binary files (“.abf”), HEKA Pulse binary files (“.pul”), and simple text files. QuB native data files can be created by data acquisition, simulation, or by processing other files (e.g., by extracting a subset of data from a file). For this demonstration, we have already prepared a data file (CCOC_Sim.qdf) that can be downloaded from the QuB website. Load this file in the data window (Main Menu > File > Open Data).

This example file contains a stochastic simulation generated with the Nav channel model that will be discussed in the next section, in response to a voltage-clamp protocol

typically used to record Nav macroscopic currents. The entire protocol contains a series of 33 sweeps, where each sweep first equilibrates the channels at -120 mV for 1 s, then “conditions” them for 200 ms at -120...+40 mV, and finally “tests” them for 50 ms at 0 mV. This protocol is typically used to extract information about the time course of supra-threshold activation and inactivation, and about the steady-state activation and inactivation.

A simple but powerful feature in QuB is that it allows the user to manually select different sections in a data file and assign them to a “data list”, which can contain multiple “selections”. For the so-called gap-free data files, QuB has the option of displaying the entire data as if it were a text that can be scrolled through line by line, or page by page. For data files that are structured in sweeps, QuB automatically creates one list for each stimulation protocol, with the selections in the list corresponding to the sweeps in the protocol. Whether created by hand or automatically, lists can be displayed individually, with the selections overlapped, as shown in Fig.4. 2. We will use this feature here.

For your convenience, we created five lists in the CCOC_Sim.qdf file, named Segments, Protocol, ActSteps, InActSteps, and ActFit. The Segments list points to all the 33 sweeps in the file, each in its entirety, whereas the other lists point to different subsections in the data. For example, the Protocol list, which is the one displayed in Fig. 4.2, points to the last 300 ms in each sweep. In general, you have the choice of analyzing the entire data file (or multiple data files), a single selection list with multiple selections, or a single stretch of data that you have just selected on the screen. For this demonstration, we will analyze the data referenced by the ActFit list, as shown in Fig.4.

3. The ActFit list points to the first 5 ms of data in the conditioning step, and contains only the steps where the voltage is equal to, or greater than -50 mV. The other traces were not included in the list, because the channel is not activated at those negative voltages and we would gain nothing by fitting them.

Prepare a kinetic model. QuB can be used to create and analyze ion channel kinetic mechanisms of arbitrary complexity. For this demonstration, we have already prepared several model files (CCOC_Sim.qmf, CCOC_FitStart.qmf, and CCOC_Fit.qmf) that can be downloaded from the QuB website. Load these files in the Model window.

The first of these models, CCOC_Sim.qmf (Fig.4. 4), was used to simulate the data contained in the CCOC_Sim.qdf file, and it is the same as the model used in (Navarro et al., 2018). We must emphasize that this simple model is not a realistic representation of the Nav mechanism. Nevertheless, it will serve well for this demonstration, as it is smaller and easier to use than the model shown Fig.4. 1 but still captures the essential properties of Nav channels, as illustrated in Fig.4. 3. The other two models, CCOC_FitStart.qmf and CCOC_Fit.qmf (Fig.4. 5), are identical with each other and have the same topology as the CCOC_Sim.qmf model, but their parameters have been modified from the “true” values that were used to simulate the data, and result in a very different set of curves (Fig.4. 6). The CCOC_FitStart.qmf model will be used here simply to mark the starting point of the optimization, whereas the CCOC_Fit.qmf will be used to actually fit the data, and it will contain the estimated parameters produced by the optimizer. When you want to repeat an optimization using the same initial values, you can right-click on the model name in the list of opened model files, and select Revert to saved. If you accidentally saved the CCOC_Fit.qmf model with the wrong parameters

and cannot revert, you can copy and paste the original model from the CCOC_FitStart.qmf model, or download the file again from the QuB website.

Define linear parameter constraints. The model provided for this demonstration, CCOC_FitStart.qmf (Fig.4. 5), has already been edited to feature the same linear parameter constraints as in (Navarro et al., 2018). These constraints define the following mathematical relationships:

$$(2) \quad k_{1,2} = a_1 \times k_{2,3},$$

$$(3) \quad k_{3,2} = a_1 \times k_{2,1},$$

$$(4) \quad k_{3,4}^1 = k_{2,3}^1,$$

$$(5) \quad k_{4,3}^1 \leq 0,$$

$$(6) \quad k_{2,1}^1 \geq -0.15,$$

where a_1 is a factor that defines relationships between rates, and which itself must be estimated.

To see how these linear parameter constraints are implemented in QuB, right-click on the model and select Properties, which brings in view the model editor. Select the Kinetic constraints panel, as shown in Fig.4. 7. This interface provides a list of Constraint types, from which you can select and create your list of Defined constraints. Note that you can create any number of Defined constraints but have only a subset of these active and enforced by the optimizer, which is convenient for running tests with

different combinations of constraints.

As discussed in (Salari et al., 2018), each linear parameter constraint requires one or two mathematical relationships, with each of this implemented as a Defined constraint. For example, the constraint defined by Eq. 2 is implemented by Defined constraints #1 and #2, which take the following mathematical forms:

$$(7) \log(k_{1,2}^0) - \log(k_{2,3}^0) - \log(a_1) = 0 \text{ and}$$

$$(8) k_{1,2}^1 - k_{2,3}^1 = 0 .$$

The constraint defined by Eq. 3 is similarly implemented by Defined constraints #3 and #4, Eq. 4 by #5, Eq. 5 by #6, and Eq. 6 by #7. For convenience, the common types of constraints are predefined (e.g., Fix rate or Scale rate), but arbitrary relationships can also be created using the Generalized type. For the predefined constraints, you only need to specify the transitions involved, the value of the ratio or the fixed value, and whether you have equality or inequality. For example, to specify the constraint that enforces Eq. 4, you select Scale exps as the Constraint type, enter “3 4 2 3” for States to indicate that you want to scale $k_{3,4}^1$ to $k_{2,3}^1$, and enter 1 for Value and “=” for Equality, to indicate that the two parameters are equal to each other. For generalized constraints, you have a table where you provide the coefficients of the parameters present in that relationship. For example, to enforce Eq. 7, you enter coefficients values of 1 for $\log(k_{1,2}^0)$, -1 for $\log(k_{2,3}^0)$, and -1 for $\log(a_1)$, a free term value of 0, and “=” to indicate equality.

Formulate behavioral constraints. Unlike linear parameter constraints, which are predefined and can be created easily via the graphical constraint editor shown in Fig.4. 7,

behavioral constraints are by necessity arbitrary and must be defined as custom code. This offers full flexibility but requires you to write code. Fortunately, QuB provides a high-level scripting language that implements many useful functions for manipulating ion channel models. This scripting language is accessible in two ways: as a program-like script that can be edited and run in the Script window, or as (smaller) snippets of code that can be defined in the Scriptlets window. These scriptlets can be run interactively, by clicking on their corresponding buttons, or can be called programmatically as functions, from the main script or from other scriptlets. For this demonstration, we have already prepared a scriptlet library file, Constraints.slf, which can be downloaded from the QuB website. Load this file in the Scriptlets window, as shown in Fig.4. 8.

The library contains three scriptlets that define the set of behavioral constraints that were used in (Navarro et al., 2018) to enforce the number of channels (Calc Nc Penalty), the maximum open probability (Calc Popen Penalty), and the recovery from inactivation (Calc RI Penalty). The code associated with each scriptlet can be accessed and modified by right-clicking with the mouse on the button. Once you made a change in the code, click the Compile button. If you made a coding error, the program will highlight its place.

The Calc Nc Penalty scriptlet contains the following code:

```
/*  
Enforce a range constraint on Nc:  
Nc_Low <= Nc <= Nc_High  
*/
```

```

//Nc range limits

var dbl

    Nc_Low = 6000,

    Nc_High = 8000;

//Declare some variables

var dbl

    Nc,

    Nc_PenaltyLow = 0,

    Nc_PenaltyHigh = 0;

//Get Nc from the optimized model

Nc = macionchannel.channelcount;

//Calculate penalty

if Nc < Nc_Low then {

    Nc_PenaltyLow = ((Nc - Nc_Low)/Nc_Low)^2;

};

if Nc > Nc_High then {

    Nc_PenaltyHigh = ((Nc_High - Nc)/Nc_High)^2;

};

//Return result

```

```
result = Nc_PenaltyLow + Nc_PenaltyHigh;
```

As coded, this constraint will force the estimate of N_C to be between 6000 and 8000. The code is very simple, as it only needs to retrieve N_C from the model being optimized by the Mac Rates algorithm (the `macionchannel` object in the code) and then calculate the penalty.

The Calc Popen Penalty scriptlet contains the following code:

```
/*  
Enforce an equality constraint on Popen:  
    Popen = Popen_Value  
*/  
  
//Popen value  
var dbl  
    Popen_Value = 0.5;  
  
//Local copy of the optimized model  
ionchannel icMyModel;  
  
//Declare some variables  
var dbl  
    V,  
    V0 = -120.0, //mV  
    V1 = 0.0,
```

```

tp = 5.0, //ms

dt = 0.01,

Popen_Max;

//Get the kinetics from the optimized model

icMyModel.copyfrom(macionchannel);

icMyModel.setvoltage(V);

//Calculate the equilibrium state occupancies under V = V0

icMyModel.calceq(voltage = V0, update = true);

//Simulate response to voltage step (V = V1, t = tp), and retrieve maximum Popen

V = V1;

icMyModel.calca;

icMyModel.calca(dt = dt);

Popen_Max = icMyModel.advance(time = tp, return = RETURN_MAX_POPEN);

//Calculate penalty and return result

result = (Popen_Max - Popen_Value)^2;

```

The effect of this constraint is to force the optimizer to find a set of parameters that satisfy the condition that the maximum open probability reached by the channel during a depolarizing voltage step has a value of 0.5. This code is still simple, as it takes advantage of some high-level functions that first calculate the equilibrium probabilities

(calcpeq), the rate constant matrix (calcq), the transition probability matrix (calca), and then simulate the model in response to a voltage step (advance). If the stimulation protocol contained more sections, you would only need to change the value assigned to V, and repeat the sequence of calcq, calca, and advance calls, as shown next.

The Calc RI Penalty scriptlet contains the following code:

```
/*  
  
Enforce an equality constraint on RI fraction:  
  
RI = RI_Value  
  
*/  
  
//RI value  
  
var dbl  
  
RI_Value = 0.8;  
  
//Local copy of the optimized model  
  
ionchannel icMyModel;  
  
//Declare some variables  
  
var dbl  
  
V,  
  
V0 = -80.0, //mV  
  
V1 = 0.0,  
  
tp = 5.0, //ms
```

```

tr = 50.0,

dt = 0.01,

Popen_Max1, Popen_Max2, RI;

//Get the kinetics from the optimized model

icMyModel.copyfrom(macionchannel);

icMyModel.setvoltage(V);

//Calculate the equilibrium state occupancies under V = V0

icMyModel.calceq(voltage = V0, update = true);

//Simulate response to first voltage step (V = V1, t = tp), and retrieve maximum Popen

V = V1;

icMyModel.calcq;

icMyModel.calca(dt = dt);

Popen_Max1 = icMyModel.advance(time = tp, return = RETURN_MAX_POPEN);

//Simulate response to recovery interval (V = V0, t = tr)

V = V0;

icMyModel.calcq;

icMyModel.calca(dt = dt);

icMyModel.advance(time = tr);

```

```

//Simulate response to second voltage step (V = V1, t = tp), and retrieve maximum Popen
V = V1;

icMyModel.calcq;

icMyModel.calca(dt = dt);

Popen_Max2 = icMyModel.advance(time = tp, return = RETURN_MAX_POPEN);

//Calculate RI fraction

RI = Popen_Max2 / Popen_Max1;

//Calculate penalty and return result

result = (RI - RI_Value)^2;

```

This constraint forces the optimizer to find a set of parameters that satisfy the condition that the fraction of channels that recover from inactivation after 50 ms is equal to 0.8. As explained in (Navarro et al., 2018), these three constraints enforce values that are intentionally different from the “true” values used to simulate the data contained in the CCOC_Sim.qdf file, to demonstrate that arbitrary values can be enforced. The true values were as follows: the number of channels $N_C = 5000$, maximum $P_{Open} \approx 0.4175$, and the recovered fraction ≈ 0.4292 .

The three constraints above are just examples that illustrate how the scripting language in QuB can be used to create code that calculates the response of the model to a certain protocol. To implement any other constraints, you can take these examples as templates and further customize them. You should also be aware that there are more sophisticated ways in QuB for defining and optimizing models with constraints, but we

leave that as an exercise, using the examples provided on the QuB website.

Calculating the total penalty. The three user-defined behavioral constraints implemented in this example are managed by the Calc Penalty scriptlet, which simply calls the individual constraint functions, sums up the calculated penalties, and returns the result to the optimization engine, as follows:

```
//Calculate total Penalty

var dbl

  p1 = 0, p2 = 0, p3 = 0;

//Call individual constraint functions

p1 = runscript("Calc Nc Penalty");
p2 = runscript("Calc Popen Penalty");
p3 = runscript("Calc RI Penalty");

//Sum up the values and return the result

result = p1 + p2 + p3;
```

Within this code, individual constraints can be simply turned off by commenting out their calls. For example, to apply only the channel count constraint, the code can be modified as follows:

```
...

p1 = runscript("Calc Nc Penalty");

//p2 = runscript("Calc Popen Penalty");
```



```
//p3 = runscript("Calc RI Penalty");
```

...

Of course, it would be possible to have the code that calculates the three constraints embedded in the Calc Penalty scriptlet. However, having separate code for each constraint makes it easier to manage the analysis.

Setting up the optimization. We have so far prepared the data, the model, the linear parameter constraints, and the code that calculates the behavioral constraints. The last step before fitting the data is to set up the optimization engine. QuB provides algorithms for analyzing both whole-cell (Milescu et al., 2005) and single channel (Qin et al., 1996, 2000) data, but the constraint mechanism is universal. As our example uses macroscopic currents, we will use the Mac Rates algorithm. The user-interface for this type of optimization is shown in Fig.4. 9. There is an extensive (and perhaps a little intimidating) array of options available, but the defaults work well, and there are only a few settings that must be tweaked for enforcing behavioral constraints. As highlighted in the figure, these are Constraints, Cycles, Weight, and Factor.

For this demonstration, you must simply instruct the program that there are behavioral constraints to be enforced, which you indicate by checking the Constraints option and by providing the name of the scriptlet that calculates them, which is Calc Penalty. The optimizer will fit the model iteratively, in several Cycles. During the search for optimum parameters, the optimizer will not only calculate the error between data and model prediction, but will also run the Calc Penalty scriptlet to calculate the constraints. The penalty value returned by this scriptlet will be multiplied by a Weight factor, and then the error and the weighted penalty will be added together. It is this sum that the

optimizer will minimize during each cycle, in multiple iterations per cycle. The parameter values reached at the end of one cycle will become the starting parameters for the next cycle. However, the weight of the penalty will be increased by a Factor.

Through these options, the constraints can be enforced more loosely at the beginning of the optimization, but more and more tightly with each optimization cycle. This iterative approach has a reason: if the behavioral constraints are too strong in the beginning, the optimizer may get stuck with a suboptimal solution. In practice, we find that a few cycles – or sometimes, depending on the problem, just one – are enough for a good fit with tightly enforced behavioral constraints. To better understand these options and the general workflow of optimization with constraints, consult Fig.4. 1 in (Navarro et al., 2018).

Run the optimization. In (Navarro et al., 2018), we tested the constrained optimization algorithm in several runs, with different combinations of constraints applied in each run. For the sake of simplicity, here we run only two tests: in the first run, we fit the data without enforcing any constraint; in the second run, we fit the data with all the linear parameter constraints and the behavioral constraints enforced. Nevertheless, when you are done with this demonstration, you can experiment with other combinations.

Furthermore, we only fit the data shown in Fig.4. 3, without including the steady-state activation and inactivation curves, as in the previous study. Considering these procedural differences, we expect to obtain different parameter estimates than in (Navarro et al., 2018). The prediction of the model corresponding to the starting parameter values is shown in Fig.4. 6.

Run I – no constraints applied. To turn off the linear parameter constraints, select the CCOC_FitStart.qmf model file, right-click on the model and select Properties, then go to the Kinetic constraints panel and uncheck all the seven Defined constraints. Next, select the CCOC_Sim.qdf data file, and make sure the FitAct list is selected (click on it). Also make sure that Data source (Fig.4. 2) is set to Selection list. Then, right-click on the Mac Rates button to raise the optimization interface, and check that have the same configuration as in Fig.4. 9, with the exception of the Constraints option, which should be unchecked. Hit Run and watch magic happen.

The optimizer will run for 100 iterations, reporting its progress via text messages in the Report window, and graphically, in the Graph window. During optimization, you will notice that the rate constants of the model change continuously, as the optimizer searches the multidimensional parameter space. You will also notice that the four scriptlets are called each time the fit curves are recalculated.

The estimated model is shown in Fig.4. 10, the fit curves are shown in Fig.4. 11, and the progress of the optimization is shown in Fig.4. 12. The results demonstrate the convergence of the optimizer when started with the “wrong” parameters. Nevertheless, be aware that the initial model must be good enough, qualitatively. Otherwise, the optimizer, which only searches locally in the parameter space, may not find a good solution. Clearly, the estimated parameters are not a good match for the “true” parameters, yet the fit is “perfect” (sum of square errors ≈ 127.73). The explanation is that the model simply has too many parameters and multiple solutions exist. If this were a real modeling project, and not just a simple demonstration, the parameters of an undetermined model would be of little use.

Run II – all constraints applied. To optimize with all the constraints enforced, you simply repeat the same steps as described above, but turn on all the linear parameter constraints in the Kinetic Constraints editor, as well as the Constraints option in the Mac Rates interface. Also set the Max step to 0.1, Cycles to 2, Weight to 1000, and Factor to 100. You are now ready to run the optimization. However, before you hit Run, you must take a moment and ask yourself: are the three behavioral constraints compatible with each other and with the data?

In fact, they are not. Specifically, the two constraints that enforce $6,000 \leq N_C \leq 8,000$ and maximum $P_{Open} = 0.5$ are mutually incompatible, given the actual data and the conductance properties of the model. Thus, the maximum peak current of -1290 pA reached during the step to 0 mV corresponds to approximately 2150 channels open, given that the conductance of the open state is 10 pS and the reversal voltage is +60 mV. Therefore, we can have either $N_C = 6000$, which gives a maximum $P_{Open} \approx 0.358$, or a maximum P_{Open} of 0.5, which gives $N_C = 4300$. However, we cannot have both at the same time. In (Navarro et al., 2018), this issue has not been raised, because these two constraints were not enforced at the same time. To eliminate this incompatibility here, you can either disable the N_C constraint, or change the maximum P_{Open} constraint to enforce a compatible value, such as 0.3. In this case, the Calc Popen Penalty scriptlet will be modified as follows:

...

//Popen value

var dbl

Popen_Value = 0.3;

...

Now run the optimization. As expected, at the end of the two cycles, the estimated parameters are quite different from the previous run, due to all the enforced constraints (Fig.4. 13). The good news is that the fit curves match the data just as well (Fig.4. 14), which means that the constraints are all mutually compatible, and also compatible with the data. The behavioral constraints were already enforced quite tightly at the end of the first cycle, which ran for only 70 iterations before convergence criteria were satisfied, with the maximum $P_{\text{Open}} \approx 0.282$, instead of 0.3, and the fraction recovered ≈ 0.799 instead of 0.8. The sum of square errors was ≈ 129.47 , just a little higher than in the unconstrained run, on account of the many constraints that reduce the degrees of freedom (Fig.4. 15, green points). At the end of the second cycle, both maximum P_{Open} and the recovered fraction were within 0.0001 of their constraining values, and the sum of square errors was ≈ 129.79 (Fig.4. 15, magenta points). In conclusion, you have successfully integrated new data with known kinetic properties!

As an exercise, you can try to run the optimization with mutually incompatible behavioral constraints. What happens then? Another exercise would be to enforce the “correct” model behavior, i.e., a channel count of 5000, a maximum open probability of 0.4175, and a recovered fraction of 0.4292. Will the estimates in this case be closer to the “true” values?

An important test you should always run is to check whether the constrained model is fully determined or not, in which case you have too many degrees of freedom relative to the information contained in the data. You can run this test easily, by defining an additional linear parameter constraint that fixes any of the model parameters to a

slightly modified value, relative to the value obtained in the above fit. If the optimizer can still find a solution that fits the data just as well, even with that additional constraint that keeps it away from the previous solution, it means that the model is not fully determined. In other words, the solution you found in Run II is not unique. Alternatively, if the fit is slightly worse, you know that the solution is unique, at least in the local space surrounding it. Be aware that the optimizer engine in QuB relies on a local search algorithm that is not meant to look for a global solution, although it can be restarted by the user from different initial points in the parameter space.

Conclusions

Our objective in this chapter was to explain how QuB can be used to investigate ion channel mechanisms in a way that integrates new experimental data with known channel properties. We demonstrated this idea with stochastically simulated macroscopic currents, which were fitted with a Nav model that featured a variety of linear parameter constraints and model behavioral constraints. When you want to analyze real data, you simply repeat the same steps described here: prepare the data you want to fit, create a state model, define the constraints you want to apply, and then optimize the model. If you have single channel (or single molecule) data, then you can use the MIL or MPL single channel algorithms (Qin et al., 1996, 2000). For macroscopic data, use the Mac algorithm (Milescu et al., 2005).

If you only need to apply linear parameter constraints, then you don't have to write code: you simply use the Kinetic constraint editor (Fig.4. 7). Of course, all the difficulties inherent to mechanistic kinetic analysis still apply. However, if there are specific model behaviors that you want to enforce, you will have to write some code. If

you have even minimal experience using any scientific computation software, such as Matlab, the scripting language in QuB should present no difficulty at all, and you can easily reuse the example code available on the QuB website. Using scripts, you can also implement more complex analysis, where you can, for example, combine multiple types of data and different experimental paradigms recordings (Milescu et al., 2008).

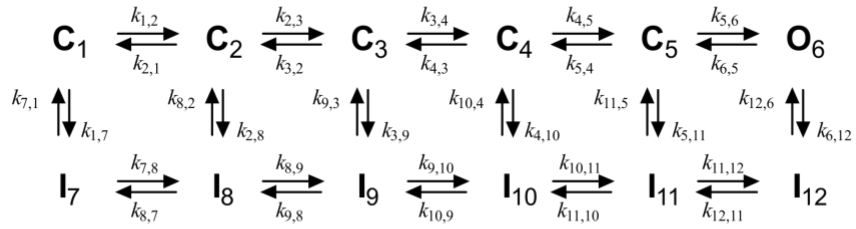


Fig. 4.1. State models for ion channel kinetic mechanisms. This example model was previously proposed to describe the kinetic properties of neuronal voltage-gated sodium (Nav) channels (Kuo & Bean, 1994). During an action potential, Nav channels undergo transitions between closed (C), open (O), and inactivated (I) states.

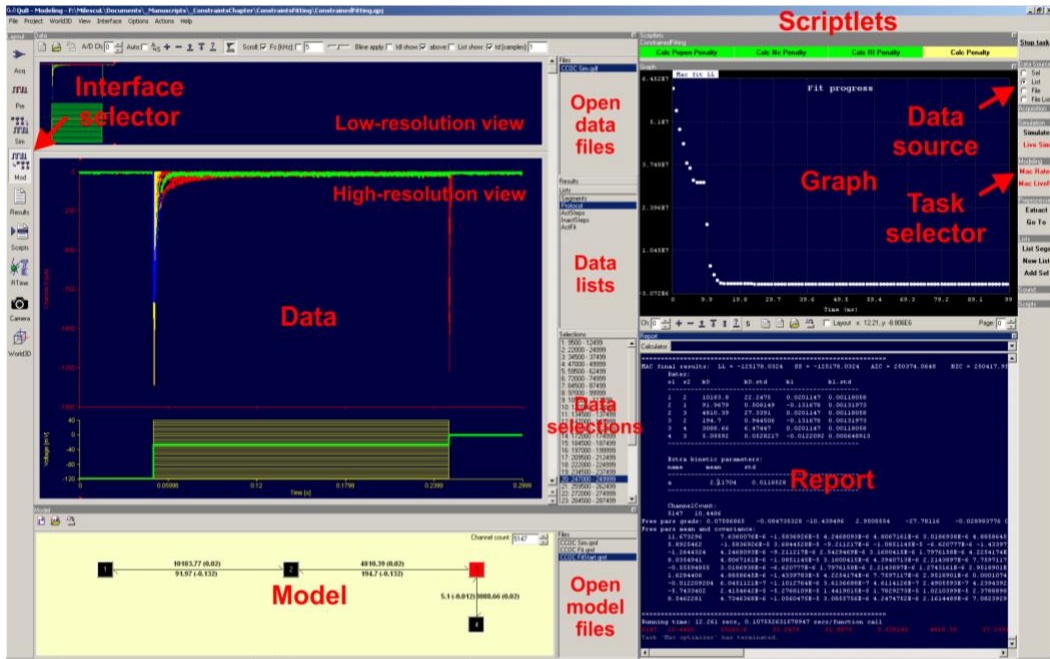


Fig. 4.2. Customizing the modeling interface in the QuB software. Different windows can be displayed and resized to create a convenient layout for visualization and analysis.

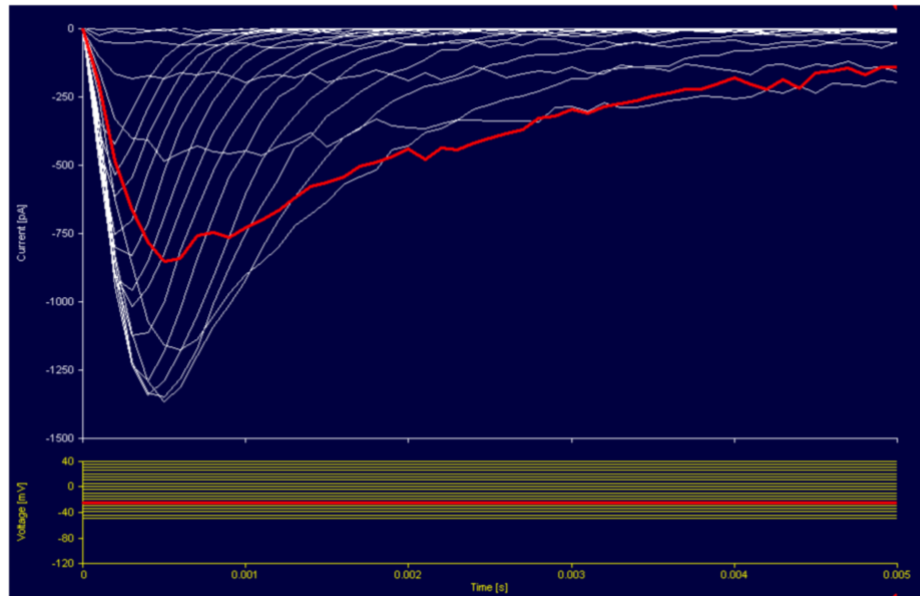


Fig. 4.3. Preparing the data for analysis. For this demonstration, a test data file (CCOC_Sim.qdf, downloadable from the QuB website) was previously generated and is loaded here in the Data window. The file contains stochastically simulated macroscopic sodium currents, generated with the Nav model shown in Fig. 4. 4, in response to a typical voltage-clamp step protocol. To have these traces displayed in QuB as shown in this figure, select the ActFit selection list in the Data window.

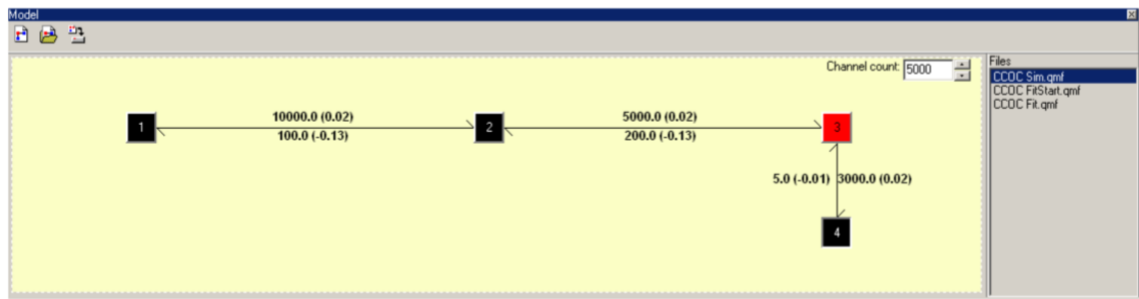


Fig. 4.4. A simple Nav model. For this demonstration, a test model file (CCOC_Sim.qmf, downloadable from the QuB website) was previously created and is loaded here in the Model window. This model was previously used to simulate the data shown in Fig.4. 3. Each number represents the value of that rate constant at 0 mV, equal to k_{ij}^0 in Eq. 1. The voltage sensitivity, equal to k_{ij}^1 in Eq. 1, is shown in parentheses.

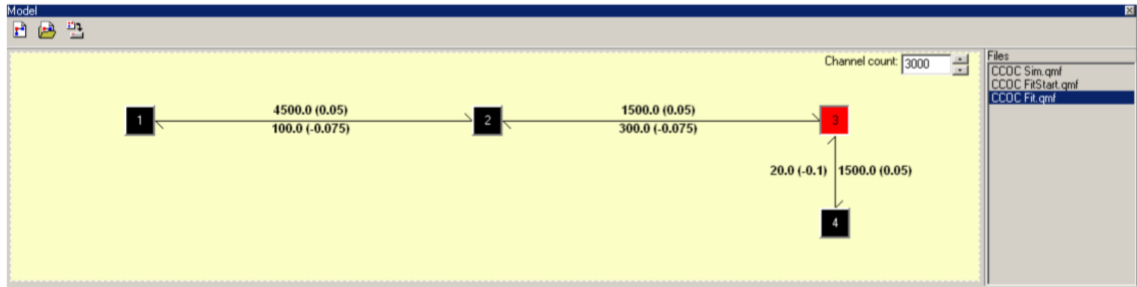


Fig. 4.5. The model used as the starting point of optimization. This model (CCOC_Fit.qmf, downloadable from the QuB website) is the same as the model shown in Fig. 4.4, but the parameters were changed to generate different predictions (Fig.4. 6).

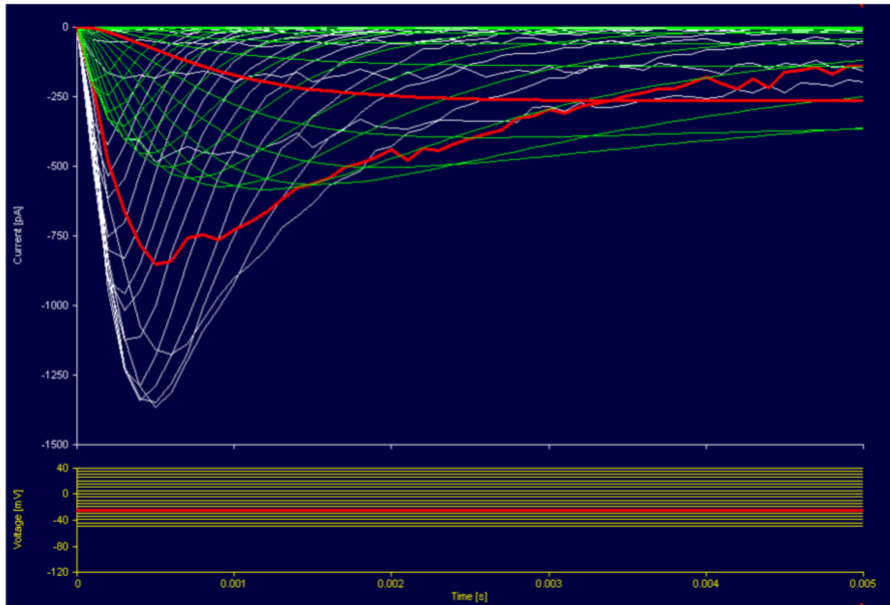


Fig. 4.6. The starting model makes predictions that significantly deviate from the **data**. The yellow curves were simulated with the CCOC_Fit.qmf model. Will the optimizer find a good solution, if the search is started with these parameters?

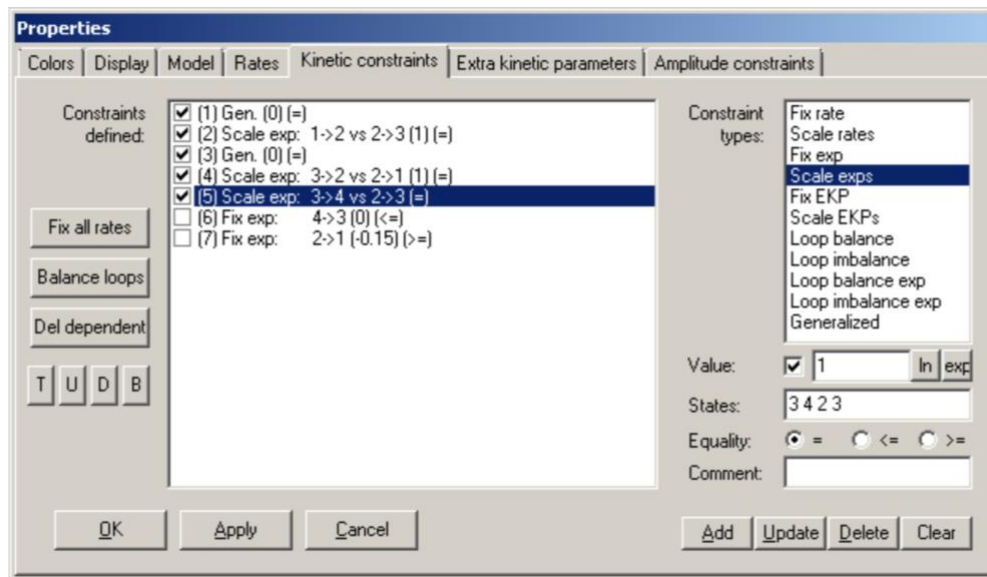


Fig. 4.7. Defining linear parameter constraints. To bring this dialog in view, right-click on the model and select Properties. The constraints prefixed by a checkmark are active and will be enforced during optimization.

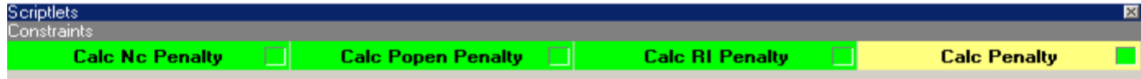


Fig. 4.8. Defining behavioral constraints. The Scriptlets window contains user-defined snippets of code that can be used to implement behavioral constraints.

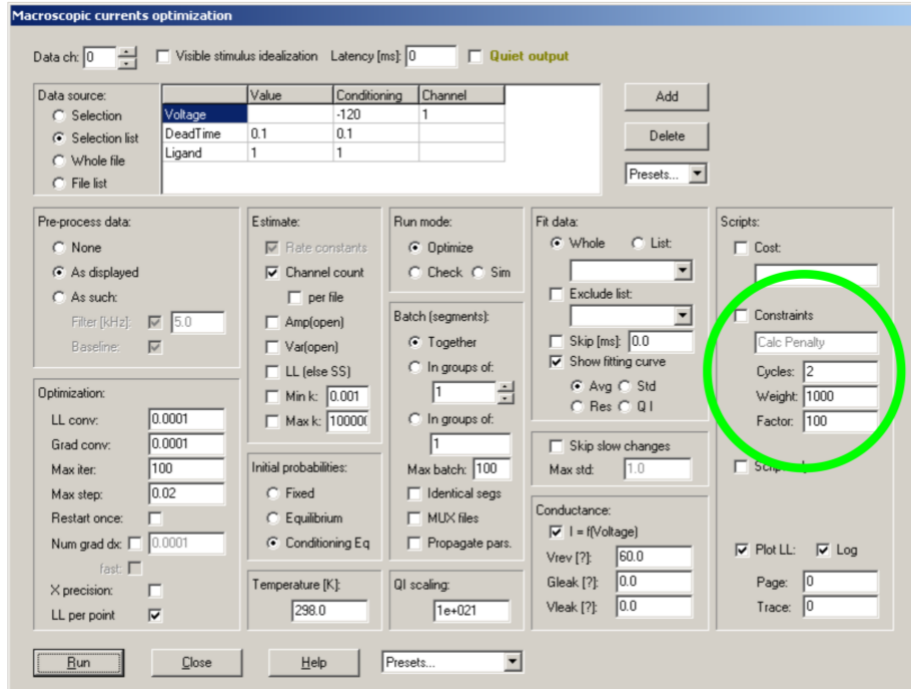


Fig. 4.9. Setting up the optimization. For macroscopic currents, we use the Mac Rates algorithm. To raise this interface, right-click on the Mac Rates button in the Task selector area.

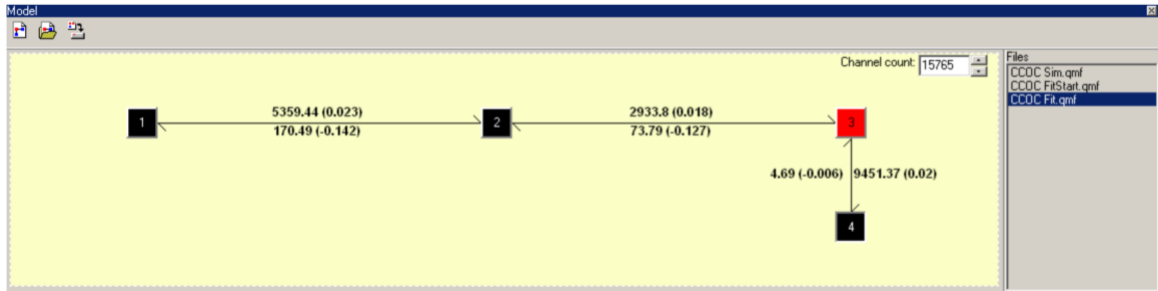


Fig. 4.10. Model parameters – no constraints applied. The rate constants shown here represent the solution found by the optimizer.

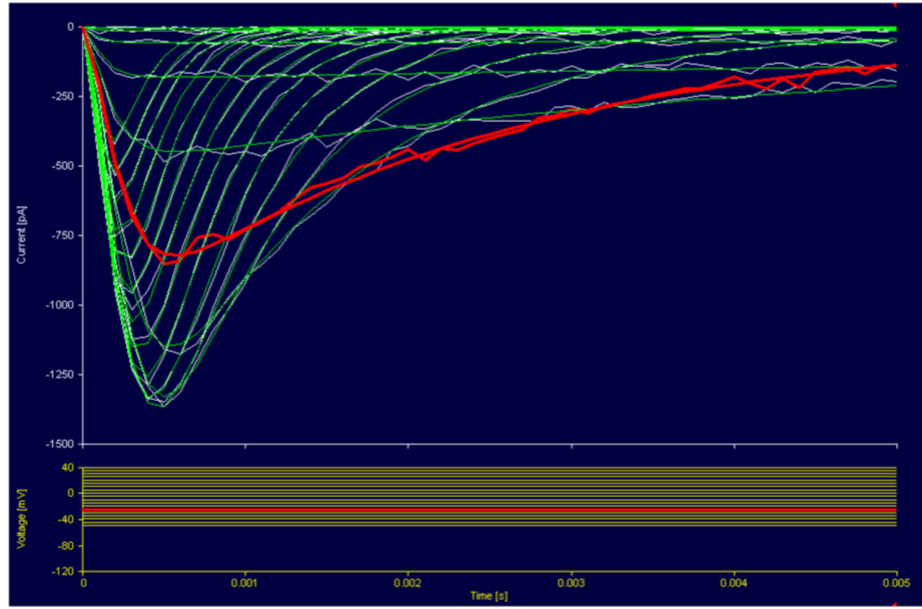


Fig. 4.11. Model predictions – no constraints applied. These fit curves were generated with the parameters shown in Fig.4. 10.

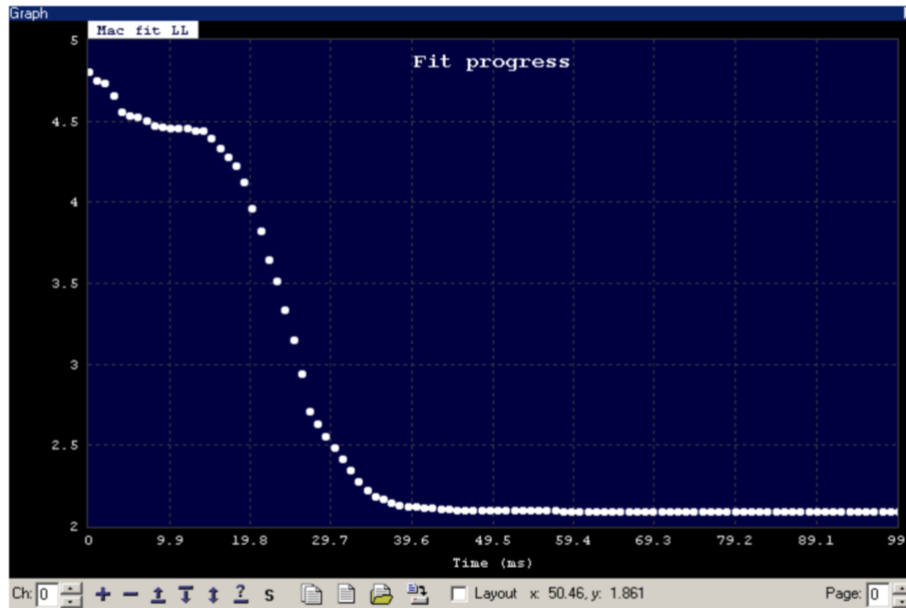


Fig. 4.12. Optimization progress – no constraints applied. The points represent the logarithm of the sum of square errors, as reduced by the optimizer at each iteration, during its search for a solution. We recommend you try different values for the Max step parameter (Fig.4. 9), which can make the search slower but more stable (e.g., with Max step = 0.01), or faster but possibly unstable (e.g., with Max step = 0.1).

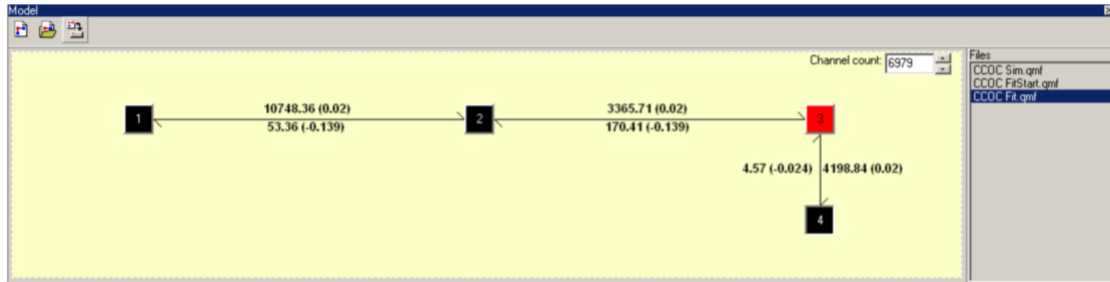


Fig 4.13. Model parameters – all constraints applied. As in Fig. 4. 10, but with all the linear parameter and model behavioral constraints applied. The values of the enforced model properties (number of channels, maximum open probability, and fraction of channels recovered from inactivation) are given in the main text.

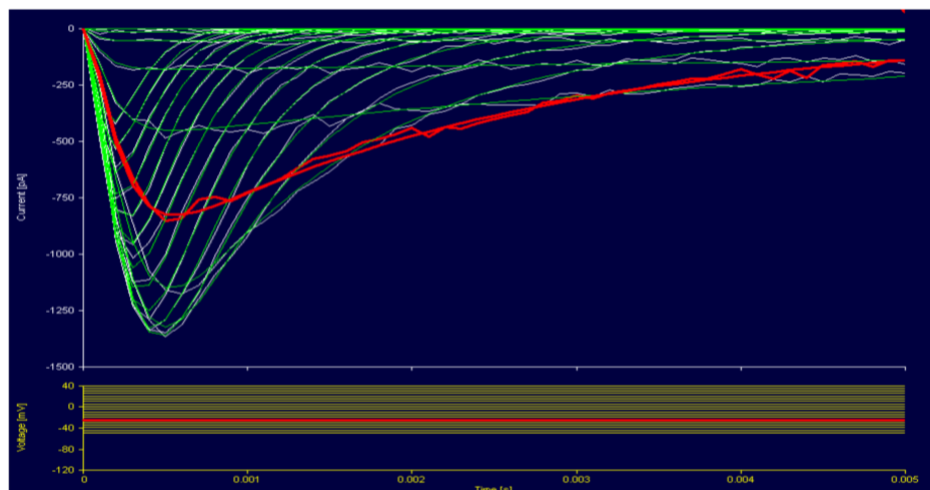


Fig. 4.14. Model predictions – all constraints applied. These fit curves were generated with the parameters shown in Fig.4. 13 and are just as good as the fit curves shown in Fig.4. 11. However, all the constraints were enforced now, which has resulted in a set of parameters (Fig.4. 13) that differ from the parameters used to simulate the data. This demonstrates that the optimization algorithm has successfully integrated new data with known kinetic properties.

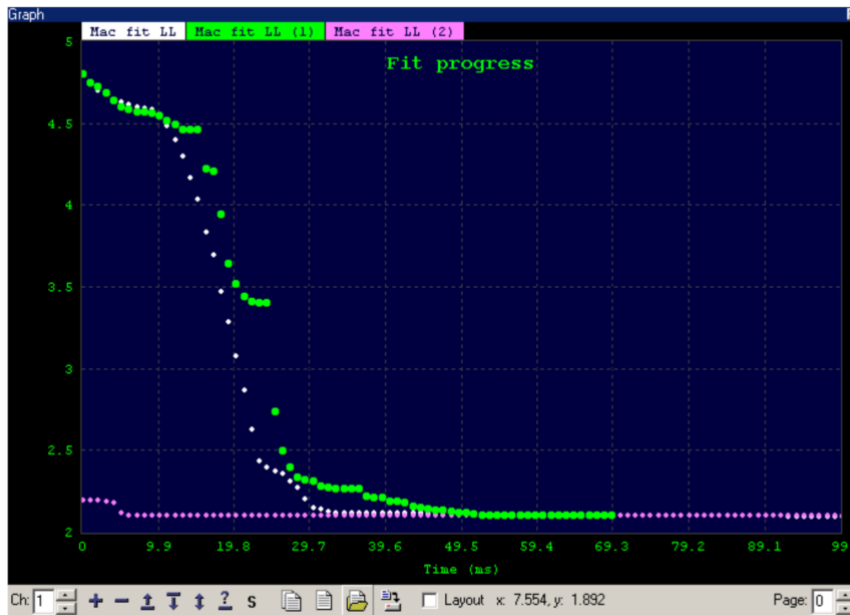


Fig. 4.15. Optimization progress – all constraints applied. The white points are the same as in Fig.4. 12, shown here for comparison. The green and the magenta points represent the sum of square errors during the first and second optimization Cycles, respectively, when all constraints were enforced. The first cycle has terminated in 70 iterations, instead of 100, because the convergence criteria were satisfied sooner.

Chapter 5

Methods

Otherwise noted, the reagents were purchased from Sigma-Aldrich, USA (St. Louis, MO).

Gr28b constructs and oocyte expression. The *Gr28b* genes were cloned in pcDNA3.1+/C-(K)DYK (GenScript). Complementary RNA (cRNA) was synthesized using T7 polymerase (mMessage mMachin kit, Ambion, USA), after linearizing the DNA with XmaI. All *Gr28b* constructs were expressed in *Xenopus laevis* oocytes, and studied 1 - 3 days after cRNA injection. The oocytes were incubated at 15 °C in a ND96 solution containing (in mM): 96 NaCl, 2 KCl, 5 HEPES, 1 MgCl₂, 1.8 CaCl₂, and 50 µg/ml gentamicin, adjusted to pH 7 with NaOH.

Site-directed mutagenesis. Single amino acid mutations made in Gr28b proteins were generated using the QuickChange II XL site-directed mutagenesis kit (Agilent Technologies). Complementary primers containing the single mutation were designed and used in the PCR reaction. Resulting DNA was treated with endonuclease DpnI to digest and separate the methylated template DNA strand from the mutated synthesized strand. The remaining PCR product was transformed in *Escherichia Coli* ultracompetent gold cells (Agilent Technologies) and incubated in NZY+ broth. All subsequent steps for expression of mutant proteins in *Xenopus* oocytes were performed as described above.

Oocyte electrophysiology and data analysis. Before cRNA injections *X. laevis* oocytes were treated with collagenase and washed several times with ND96 solution. After 1 – 3

days incubation, the oocytes were transferred into a 150 μ l recording chamber and examined via the two-electrode voltage-clamp recording technique (OC-725C amplifier, Warner Instruments, USA). Oocyte currents were low-pass filtered at 5 kHz and digitized at 10 kHz using a Digidata 1440a data acquisition system and pClamp 10 software (Molecular Devices, USA). Microelectrode resistance was 0.3 - 1 M Ω when filled with 3 M KCl. Several external recording solutions were used, all based on the standard ND96 formulation, containing (in mM): 96 NaCl, 2 KCl, 5 HEPES, 1 MgCl₂, 1.8 CaCl₂, pH 7.6 with NaOH. A low-Cl⁻ solution was formulated as: 96 NaC₆H₁₁O₇ (sodium gluconate), 2 KC₆H₁₁O₇ (potassium gluconate), 5 HEPES, 1 MgCl₂, 1.8 CaCl₂, pH 7.6 with NaOH. Two low-Na⁺ solutions were made, one with 48 mM and one with 2 mM Na⁺, obtained by substituting the corresponding amounts of NaCl with NMDG-HCl. All experiments were performed between 10 °C – 40 °C, with the temperature regulated by a bipolar temperature controller (CL-100, Harvard Apparatus, USA) and a dual in-line heater/cooler (SC-20, Warner Instruments, USA). Q₁₀ values were calculated from slow temperature ramp experiments, using the equation $Q_{10} = 10^{10 \times s}$, where s is the slope of the linear fit to the logarithmic plot of the normalized current versus temperature. The

equilibrium potentials were calculated using the Nernst equation:

$$E_x = \frac{RT}{zF} \ln \frac{[X]_o}{[X]_i},$$

where E_x is the equilibrium potential for a given ion X, of extracellular and intracellular concentrations $[X]_o$ and $[X]_i$, respectively. R , T , z and F are the usual quantities: the gas constant, the temperature, the valence of the ion, and Faraday's constant, respectively.

The data were analyzed with Clampfit 10 (Molecular Devices, USA) and Origin 2017 (OriginLab, USA).

Flies and rearing conditions (Mishra et al, 2018). The *UAS-Gr28b A, B, C, D, and E* lines were generously provided by Paul Garrity, Brandeis University (Ni, Bronk et al. 2013). The *nSyb-GAL4*, *OK6-GAL4*, and *UAS-GCaMP6f* lines were obtained from the Bloomington Stock Center, Indiana. Flies were created to overexpress *UAS-Gr28b* transgenes with the pan-neuronal *nSyb-GAL4* driver and *UAS-Gr28bD* with the motor neuron *OK6-GAL4* driver. Flies heterozygous for *nSyb-GAL4* or *UAS-Gr28b* transgenes were used as negative genetic controls. Flies expressing *UAS-Gr28bD + UAS-GCaMP6f*, or heterozygous *UAS-GCaMP6f* (control), with the *OK6-GAL4* driver, were created for the calcium fluorescence imaging experiments. Flies were reared on cornmeal-yeast medium at 25 °C in a 12 hour light-dark cycle at 60% relative humidity. Flies used for thermo-tolerance tests were 2 - 10 days of age.

Calcium fluorescence imaging and data analysis (Mishra et al, 2018). Flies, 5 - 11 days old, were dissected as previously described (Boerner and Godenschwege 2011). To eliminate descending thermotaxis signals to the ventral nerve cord, the head of the fly was removed before imaging. The dissected preparations were perfused in external saline containing (in mM): 103 NaCl, 3 KCl, 5 N-tris(hydroxymethyl) methyl-2-aminoethanesulfonic acid, 8 trehalose, 10 glucose, 26 NaHCO₃, 1 NaH₂PO₄, 1.5 CaCl₂, 4 MgCl₂, with an osmolarity between 270 – 275 mOsm. The saline was continuously bubbled with 95% O₂/ 5% CO₂ to a pH of 7.3. Perfusate temperature was regulated with a bipolar temperature controller (CL-100, Harvard Apparatus, USA), a SC-20 dual in-line heater/cooler (Warner Instruments, USA), and a LCS-1 liquid cooling system (Warner Instruments, USA). A custom imaging stage was designed in SketchUp (sketchup.com) and 3D printed with PLA using an Ultimaker Original+ (Ultimaker, Netherlands). Lateral

motor neurons in the abdominal neuromeres (Armstrong, Borner et al. 2017) were imaged on a customized upright microscope (Scientifica, UK) equipped with epifluorescence and two-photon imaging. For wide-field illumination, CoolLED p100 LED sources (CoolLED Ltd., UK), GFP filters (Chroma, USA), and a 40X water-immersion objective (Olympus LUMPLFLN40XW) were used. Images were acquired using a Hamamatsu sCMOS Flash 4.0 V2 camera (Hamamatsu Photonics KK, Japan), typically with a 25 ms exposure time. For two-photon imaging, we used a Ti:Sapphire MaiTai HP laser (Newport, USA). The QuB program (MilescuLabs.biology.missouri.edu/QuB) was used for 3D data mapping, experiment control and visualization, and image acquisition (Navarro, Hibbard et al. 2015). ScanImage 3.8.1 (Vidrio Technologies, USA) was used to control the two-photon hardware. Fluorescence signals were digitally processed, analyzed with the QuB software, and the spectral content was calculated in MATLAB 2017a (MathWorks, USA) using the continuous wavelet-transform (CWT) and a Morlet wavelet.

Behavioral experiments (Mishra et al, 2018). Behavioral experiments were performed using the heat box as previously described (Wustmann, Rein et al. 1996, Zars 2001). In the heat box, flies were allowed to walk the length of a chamber (l = 3.4 cm, w = 3 mm, h = 1 mm) lined top and bottom with Peltier elements. A light sensor was used to detect the position of the fly. The temperature in the chamber was controlled using custom software (Zars, Wolf et al. 2000). Additional custom software was used to analyze the activity of flies. In the thermotolerance assays, the temperature of the chamber was initially increased in steps of 2 °C from 24 °C to 40 °C, and later in steps of one degree from 32 °C to 40 °C. The movement of each fly was measured at each temperature step for 90

seconds. Six or seven trials were conducted for each experimental genotype, with 10 - 12 flies in each trial. A fly was considered incapacitated if it was inactive for at least 45 s within a 90 s window. To determine the time-to-incapacitation and the time-to-recovery, flies were allowed to acclimate at 24 °C for 90 s prior to a temperature jump to 34 °C - 40 °C for 90 s, and then allowed a recovery time of 15 minutes. The movement of flies was recorded for the entire duration of the test. Observations from incapacitation assays were analyzed with the Statistica 8.0 software (StatSoft, USA), using Kaplan-Meier survival analysis. P-values less than 0.05 were considered significant.

Computational modeling of Gr28bD. We used Visual Molecular Dynamics (VMD) program that is designed for modeling, visualization and analysis of biological molecules such as proteins, nucleic acids, etc (Hsin et al., 2008). VMD is designed by the Theoretical and Computational Biophysics Group from University of Illinois at Urbana Champaign.

Kinetic modeling software and simulations. For all kinetic modeling work, a version of the QuB software (<https://mileskulabs.org/qub.html>), as developed and maintained by our lab was used. Details are presented in Chapter 4.

Animal care. *Xenopus laevis* were used for harvesting oocytes. Survival surgeries and euthanasia were performed following animal protocols approved by the Animal Use and Care Committee at the University of Missouri.

Conclusions and summary

Developing better tools for extrinsic control of brain activity is of paramount importance to neuroscience. These tools enable scientists to manipulate the electrical activity of specific neurons within the dense and complex network of brain. By activating or inhibiting specific cells, we can understand how these neurons work within their circuits. Optogenetics is the most widely used approach, but thermogenetics has emerged as a complementary technique, expanding the number of control modalities, as well as the range of preparations.

My work on thermosensitive gustatory receptors from *Drosophila* species should hopefully advance the range of existing thermogenetic tools, and at the same time shed new light on thermosensitivity mechanisms in ion channels. To summarize, my colleagues and I have investigated the thermosensitivity properties of the Gr28bD receptor from *D. melanogaster*, as well as its orthologs from related species. We heterologously expressed these proteins in *Xenopus laevis* oocytes and examined their channel activity via the two-electrode voltage-clamp method. We then formulated a computational model of these proteins using the recently solved structure of Orco (olfactory co-receptor protein) as a scaffold. With this model, we designed and tested a number of mutations, to validate the model and the overall topology of the protein, and to understand how different parts of the channel contribute to the pore structure and the thermosensitive domains.

Of course, much work remains to be done. Most importantly, to fully understand the mechanisms of mechanosensitivity in Gr28bD and to be able to rationally design new channels with specific properties, we need to obtain a high-resolution structure of the channel, possibly through cryo-EM.

References

- Adamantidis, A. R., Zhang, F., Aravanis, A. M., Deisseroth, K., & de Lecea, L. (2007). Neural substrates of awakening probed with optogenetic control of hypocretin neurons. *Nature*, *450*(7168), 420–424. <https://doi.org/10.1038/nature06310>
- Armstrong, J. D., Texada, M. J., Munjaal, R., Baker, D. A., & Beckingham, K. M. (2006). Gravitaxis in *Drosophila melanogaster*: A forward genetic screen. *Genes, Brain and Behavior*, *5*(3), 222–239. <https://doi.org/10.1111/j.1601-183X.2005.00154.x>
- Ball, F. G., Sansom, M. S. P., & Colquhoun, D. (1989). Ion-channel gating mechanisms: Model identification and parameter estimation from single channel recordings. *Proceedings of the Royal Society of London. B. Biological Sciences*, *236*(1285), 385–416. <https://doi.org/10.1098/rspb.1989.0029>
- Barbagallo, B., & Garrity, P. A. (2015a). Temperature sensation in *Drosophila*. *Current Opinion in Neurobiology*, *34*, 8–13. <https://doi.org/10.1016/j.conb.2015.01.002>
- Barbagallo, B., & Garrity, P. A. (2015b). Temperature sensation in *Drosophila*. *Current Opinion in Neurobiology*, *34*, 8–13. <https://doi.org/10.1016/j.conb.2015.01.002>
- Bean, B. P. (2007). The action potential in mammalian central neurons. *Nature Reviews Neuroscience*, *8*(6), 451–465. <https://doi.org/10.1038/nrn2148>
- Bellemer, A. (2015). Thermotaxis, circadian rhythms, and TRP channels in *Drosophila*. *Temperature*, *2*(2), 227–243. <https://doi.org/10.1080/23328940.2015.1004972>
- Benton, R., Sachse, S., Michnick, S. W., & Vosshall, L. B. (2006). Atypical Membrane Topology and Heteromeric Function of *Drosophila* Odorant Receptors In Vivo. *PLOS Biology*, *4*(2), e20. <https://doi.org/10.1371/journal.pbio.0040020>

Benzer, S. (1967). BEHAVIORAL MUTANTS OF *Drosophila* ISOLATED BY COUNTERCURRENT DISTRIBUTION. *Proceedings of the National Academy of Sciences of the United States of America*, 58(3), 1112–1119.

Berndt, A., Lee, S. Y., Ramakrishnan, C., & Deisseroth, K. (2014). Structure-Guided Transformation of Channelrhodopsin into a Light-Activated Chloride Channel. *Science*, 344(6182), 420–424. <https://doi.org/10.1126/science.1252367>

Bernstein, J. G., Garrity, P. A., & Boyden, E. S. (2012a). Optogenetics and thermogenetics: Technologies for controlling the activity of targeted cells within intact neural circuits. *Current Opinion in Neurobiology*, 22(1), 61–71. <https://doi.org/10.1016/j.conb.2011.10.023>

Bernstein, J. G., Garrity, P. A., & Boyden, E. S. (2012b). Optogenetics and thermogenetics: Technologies for controlling the activity of targeted cells within intact neural circuits. *Current Opinion in Neurobiology*, 22(1), 61–71. <https://doi.org/10.1016/j.conb.2011.10.023>

Boerner, J., & Godenschwege, T. A. (2011). Whole Mount Preparation of the Adult *Drosophila* Ventral Nerve Cord for Giant Fiber Dye Injection. *Journal of Visualized Experiments : JoVE*, 52, 3080. <https://doi.org/10.3791/3080>

Boton, R., Dascal, N., Gillo, B., & Lass, Y. (1989). Two calcium-activated chloride conductances in *Xenopus laevis* oocytes permeabilized with the ionophore A23187. *The Journal of Physiology*, 408(1), 511–534. <https://doi.org/10.1113/jphysiol.1989.sp017473>

Boyden, E. S. (2011). A history of optogenetics: The development of tools for controlling brain circuits with light. *FL1000 Biology Reports*, 3, 11.

<https://doi.org/10.3410/B3-11>

Butterwick, J. A., del Marmol, J., Kim, K. H., Kahlson, M. A., Rogow, J. A., Walz, T., & Ruta, V. (2018). Cryo-EM structure of the insect olfactory receptor Orco. *Nature*, 560(7719), 447–452. <https://doi.org/10.1038/s41586-018-0420-8>

Cao, E., Cordero-Morales, J. F., Liu, B., Qin, F., & Julius, D. (2013). TRPV1 Channels Are Intrinsically Heat Sensitive and Negatively Regulated by Phosphoinositide Lipids. *Neuron*, 77(4), 667–679. <https://doi.org/10.1016/j.neuron.2012.12.016>

Card, G., & Dickinson, M. H. (2008). Visually Mediated Motor Planning in the Escape Response of *Drosophila*. *Current Biology*, 18(17), 1300–1307.

<https://doi.org/10.1016/j.cub.2008.07.094>

Caterina, M. J., & Julius, D. (2001). The Vanilloid Receptor: A Molecular Gateway to the Pain Pathway. *Annual Review of Neuroscience*, 24(1), 487–517.

<https://doi.org/10.1146/annurev.neuro.24.1.487>

Caterina, M. J., Rosen, T. A., Tominaga, M., Brake, A. J., & Julius, D. (1999). A capsaicin-receptor homologue with a high threshold for noxious heat. *Nature*, 398(6726), 436–441. <https://doi.org/10.1038/18906>

Caterina, M. J., Schumacher, M. A., Tominaga, M., Rosen, T. A., Levine, J. D., & Julius, D. (1997). The capsaicin receptor: A heat-activated ion channel in the pain pathway. *Nature*, 389(6653), 816–824. <https://doi.org/10.1038/39807>

Celentano, J. J., & Hawkes, A. G. (2004). Use of the Covariance Matrix in Directly Fitting Kinetic Parameters: Application to GABAA Receptors. *Biophysical Journal*, 87(1), 276–294. <https://doi.org/10.1529/biophysj.103.036632>

Chow, B. Y., Han, X., Dobry, A. S., Qian, X., Chuong, A. S., Li, M., Henninger, M. A., Belfort, G. M., Lin, Y., Monahan, P. E., & Boyden, E. S. (2010). High-performance genetically targetable optical neural silencing by light-driven proton pumps. *Nature*, 463(7277), 98–102. <https://doi.org/10.1038/nature08652>

Clapham, D. E. (2003a). TRP channels as cellular sensors. *Nature*, 426(6966), 517–524. <https://doi.org/10.1038/nature02196>

Clapham, D. E. (2003b). TRP channels as cellular sensors. *Nature*, 426(6966), 517–524. <https://doi.org/10.1038/nature02196>

Clapham, D. E., & Miller, C. (2011). A thermodynamic framework for understanding temperature sensing by transient receptor potential (TRP) channels. *Proceedings of the National Academy of Sciences*, 108(49), 19492–19497. <https://doi.org/10.1073/pnas.1117485108>

Clyne, P. J., Warr, C. G., Freeman, M. R., Lessing, D., Kim, J., & Carlson, J. R. (1999). A Novel Family of Divergent Seven-Transmembrane Proteins: Candidate Odorant Receptors in *Drosophila*. *Neuron*, 22(2), 327–338. [https://doi.org/10.1016/S0896-6273\(00\)81093-4](https://doi.org/10.1016/S0896-6273(00)81093-4)

Colquhoun, D., & Hawkes, A. G. (1995). A Q-Matrix Cookbook. In B. Sakmann & E. Neher (Eds.), *Single-Channel Recording* (pp. 589–633). Springer US. https://doi.org/10.1007/978-1-4419-1229-9_20

Colquhoun, D., & Sigworth, F. J. (1995a). Fitting and Statistical Analysis of Single-Channel Records. In B. Sakmann & E. Neher (Eds.), *Single-Channel Recording* (pp. 483–587). Springer US. https://doi.org/10.1007/978-1-4419-1229-9_19

Colquhoun, D., & Sigworth, F. J. (1995b). Fitting and Statistical Analysis of Single-Channel Records. In B. Sakmann & E. Neher (Eds.), *Single-Channel Recording* (pp. 483–587). Springer US. https://doi.org/10.1007/978-1-4419-1229-9_19

Court, R., Namiki, S., Armstrong, D., Börner, J., Card, G., Costa, M., Dickinson, M., Duch, C., Korff, W., Mann, R., Merritt, D. J., Murphey, R. K., Seeds, A., Shirangi, T., Simpson, J. H., Truman, J. W., Tuthill, J., Williams, D., & Shepherd, D. (2020). *A Systematic Nomenclature for the Drosophila Ventral Nervous System* (SSRN Scholarly Paper ID 3545527). Social Science Research Network.

<https://doi.org/10.2139/ssrn.3545527>

Csanády, L. (2006). Statistical Evaluation of Ion-Channel Gating Models Based on Distributions of Log-Likelihood Ratios. *Biophysical Journal*, 90(10), 3523–3545.

<https://doi.org/10.1529/biophysj.105.075135>

Dai, J., Ozden, I., Brooks, D. I., Wagner, F., May, T., Agha, N. S., Brush, B. R., Borton, D., Nurmikko, A. V., & Sheinberg, D. L. (2015). Modified toolbox for optogenetics in the nonhuman primate. *Neurophotonics*, 2(3), 031202.

<https://doi.org/10.1117/1.NPh.2.3.031202>

DeGennaro, M., McBride, C. S., Seeholzer, L., Nakagawa, T., Dennis, E. J., Goldman, C., Jasinskiene, N., James, A. A., & Vosshall, L. B. (2013). Orco mutant mosquitoes lose strong preference for humans and are not repelled by volatile DEET. *Nature*, 498(7455), 487–491. <https://doi.org/10.1038/nature12206>

Dhaka, A., Viswanath, V., & Patapoutian, A. (2006a). Trp Ion Channels and Temperature Sensation. *Annual Review of Neuroscience*, 29(1), 135–161.

<https://doi.org/10.1146/annurev.neuro.29.051605.112958>

Dhaka, A., Viswanath, V., & Patapoutian, A. (2006b). Trp Ion Channels and Temperature Sensation. *Annual Review of Neuroscience*, 29(1), 135–161.

<https://doi.org/10.1146/annurev.neuro.29.051605.112958>

Diester, I., Kaufman, M. T., Mogri, M., Pashaie, R., Goo, W., Yizhar, O., Ramakrishnan, C., Deisseroth, K., & Shenoy, K. V. (2011). An optogenetic toolbox designed for primates. *Nature Neuroscience*, 14(3), 387–397.

<https://doi.org/10.1038/nn.2749>

Edwards, S. L., Charlie, N. K., Milfort, M. C., Brown, B. S., Gravlin, C. N., Knecht, J. E., & Miller, K. G. (2008). A novel molecular solution for ultraviolet light detection in *Caenorhabditis elegans*. *PLoS Biology*, 6(8), e198.

<https://doi.org/10.1371/journal.pbio.0060198>

Epstein, M., Calderhead, B., Girolami, M. A., & Sivilotti, L. G. (2016). Bayesian Statistical Inference in Ion-Channel Models with Exact Missed Event Correction.

Biophysical Journal, 111(2), 333–348. <https://doi.org/10.1016/j.bpj.2016.04.053>

Ermakova, Y. G., Lanin, A. A., Fedotov, I. V., Roshchin, M., Kelmanson, I. V., Kulik, D., Bogdanova, Y. A., Shokhina, A. G., Bilan, D. S., Staroverov, D. B., Balaban, P. M., Fedotov, A. B., Sidorov-Biryukov, D. A., Nikitin, E. S., Zheltikov, A. M., & Belousov, V. V. (2017). Thermogenetic neurostimulation with single-cell resolution.

Nature Communications, 8(1), 15362. <https://doi.org/10.1038/ncomms15362>

Friedmann, D., Hoagland, A., Berlin, S., & Isacoff, E. Y. (2015). A Spinal Opsin Controls Early Neural Activity and Drives a Behavioral Light Response. *Current Biology*, 25(1), 69–74. <https://doi.org/10.1016/j.cub.2014.10.055>

Gradinaru, V., Thompson, K. R., & Deisseroth, K. (2008). eNpHR: A Natronomonas halorhodopsin enhanced for optogenetic applications. *Brain Cell Biology*, 36(1), 129–139. <https://doi.org/10.1007/s11068-008-9027-6>

Gurkiewicz, M., & Korngreen, A. (2007). A Numerical Approach to Ion Channel Modelling Using Whole-Cell Voltage-Clamp Recordings and a Genetic Algorithm. *PLOS Computational Biology*, 3(8), e169. <https://doi.org/10.1371/journal.pcbi.0030169>

Hamada, F. N., Rosenzweig, M., Kang, K., Pulver, S. R., Ghezzi, A., Jegla, T. J., & Garrity, P. A. (2008a). An internal thermal sensor controlling temperature preference in *Drosophila*. *Nature*, 454(7201), 217–220. <https://doi.org/10.1038/nature07001>

Hamada, F. N., Rosenzweig, M., Kang, K., Pulver, S. R., Ghezzi, A., Jegla, T. J., & Garrity, P. A. (2008b). An internal thermal sensor controlling temperature preference in *Drosophila*. *Nature*, 454(7201), 217–220. <https://doi.org/10.1038/nature07001>

Hawkes, A. G., Jalali, A., & Colquhoun, D. (1992). Asymptotic distributions of apparent open times and shut times in a single channel record allowing for the omission of brief events. *Philosophical Transactions of the Royal Society of London. Series B: Biological Sciences*, 337(1282), 383–404. <https://doi.org/10.1098/rstb.1992.0116>

Helmchen, F., Imoto, K., & Sakmann, B. (1996). Ca²⁺ buffering and action potential-evoked Ca²⁺ signaling in dendrites of pyramidal neurons. *Biophysical Journal*, 70(2), 1069–1081. [https://doi.org/10.1016/S0006-3495\(96\)79653-4](https://doi.org/10.1016/S0006-3495(96)79653-4)

Hille, B. (2001). *Ion channels of excitable membranes* (3rd ed). Sinauer.

Horn, R., & Lange, K. (1983). Estimating kinetic constants from single channel data. *Biophysical Journal*, 43(2), 207–223. [https://doi.org/10.1016/S0006-3495\(83\)84341-0](https://doi.org/10.1016/S0006-3495(83)84341-0)

Hsin, J., Arkhipov, A., Yin, Y., Stone, J. E., & Schulten, K. (2008). Using VMD: An Introductory Tutorial. *Current Protocols in Bioinformatics*, 24(1), 5.7.1-5.7.48. <https://doi.org/10.1002/0471250953.bi0507s24>

Huang, J., Zhang, X., & McNaughton, P. A. (2006). Modulation of temperature-sensitive TRP channels. *Seminars in Cell & Developmental Biology*, 17(6), 638–645. <https://doi.org/10.1016/j.semcdb.2006.11.002>

Ion-channel gating mechanisms: Model identification and parameter estimation from single channel recordings / *Proceedings of the Royal Society of London. B. Biological Sciences*. (n.d.). Retrieved November 23, 2021, from https://royalsocietypublishing.org/doi/abs/10.1098/rspb.1989.0029?casa_token=LZhCozwTjWgAAAAA:ZNSI8H0Zgm9EA_DPCs590k6locLNNRNzpvSBYaS5ZAGXnTj6SAIP_ReE8t2pU_Ta0VzmgjktZbfaSfc

Jordt, S.-E., McKemy, D. D., & Julius, D. (2003). Lessons from peppers and peppermint: The molecular logic of thermosensation. *Current Opinion in Neurobiology*, 13(4), 487–492. [https://doi.org/10.1016/S0959-4388\(03\)00101-6](https://doi.org/10.1016/S0959-4388(03)00101-6)

Kahsai, L., & Zars, T. (2011). Learning and Memory in *Drosophila*: Behavior, Genetics, and Neural Systems. In N. Atkinson (Ed.), *International Review of Neurobiology* (Vol. 99, pp. 139–167). Academic Press. <https://doi.org/10.1016/B978-0-12-387003-2.00006-9>

Kang, K., Panzano, V. C., Chang, E. C., Ni, L., Dainis, A. M., Jenkins, A. M., Regna, K., Muskavitch, M. A. T., & Garrity, P. A. (2012). Modulation of TRPA1 thermal sensitivity enables sensory discrimination in *Drosophila*. *Nature*, *481*(7379), 76–80.

<https://doi.org/10.1038/nature10715>

Klapoetke, N. C., Murata, Y., Kim, S. S., Pulver, S. R., Birdsey-Benson, A., Cho, Y. K., Morimoto, T. K., Chuong, A. S., Carpenter, E. J., Tian, Z., Wang, J., Xie, Y., Yan, Z., Zhang, Y., Chow, B. Y., Surek, B., Melkonian, M., Jayaraman, V., Constantine-Paton, M., ... Boyden, E. S. (2014a). Independent optical excitation of distinct neural populations. *Nature Methods*, *11*(3), 338–346. <https://doi.org/10.1038/nmeth.2836>

Klapoetke, N. C., Murata, Y., Kim, S. S., Pulver, S. R., Birdsey-Benson, A., Cho, Y. K., Morimoto, T. K., Chuong, A. S., Carpenter, E. J., Tian, Z., Wang, J., Xie, Y., Yan, Z., Zhang, Y., Chow, B. Y., Surek, B., Melkonian, M., Jayaraman, V., Constantine-Paton, M., ... Boyden, E. S. (2014b). Independent optical excitation of distinct neural populations. *Nature Methods*, *11*(3), 338–346. <https://doi.org/10.1038/nmeth.2836>

Kuo, C.-C., & Bean, B. P. (1994). Na⁺ channels must deactivate to recover from inactivation. *Neuron*, *12*(4), 819–829. [https://doi.org/10.1016/0896-6273\(94\)90335-2](https://doi.org/10.1016/0896-6273(94)90335-2)

Larsson, M. C., Domingos, A. I., Jones, W. D., Chiappe, M. E., Amrein, H., & Vosshall, L. B. (2004). Or83b Encodes a Broadly Expressed Odorant Receptor Essential for *Drosophila* Olfaction. *Neuron*, *43*(5), 703–714.

<https://doi.org/10.1016/j.neuron.2004.08.019>

Latorre, R., Zaelzer, C., & Brauchi, S. (2009). Structure–functional intimacies of transient receptor potential channels. *Quarterly Reviews of Biophysics*, *42*(3), 201–246.

<https://doi.org/10.1017/S0033583509990072>

Lewis, L. P. C., Siju, K. P., Aso, Y., Friedrich, A. B., Bulteel, A. J. B., Rubin, G. M., & Grunwald Kadow, I. C. (2015). A Higher Brain Circuit for Immediate Integration of Conflicting Sensory Information in *Drosophila*. *Current Biology*, 25(17), 2203–2214. <https://doi.org/10.1016/j.cub.2015.07.015>

Liao, M., Cao, E., Julius, D., & Cheng, Y. (2013). Structure of the TRPV1 ion channel determined by electron cryo-microscopy. *Nature*, 504(7478), 107–112. <https://doi.org/10.1038/nature12822>

Mancuso, J. J., Kim, J., Lee, S., Tsuda, S., Chow, N. B. H., & Augustine, G. J. (2011). Optogenetic probing of functional brain circuitry. *Experimental Physiology*, 96(1), 26–33. <https://doi.org/10.1113/expphysiol.2010.055731>

Matsuno-Yagi, A., & Mukohata, Y. (1977). Two possible roles of bacteriorhodopsin; a comparative study of strains of *Halobacterium halobium* differing in pigmentation. *Biochemical and Biophysical Research Communications*, 78(1), 237–243. [https://doi.org/10.1016/0006-291X\(77\)91245-1](https://doi.org/10.1016/0006-291X(77)91245-1)

Menon, V., Spruston, N., & Kath, W. L. (2009). A state-mutating genetic algorithm to design ion-channel models. *Proceedings of the National Academy of Sciences*, 106(39), 16829–16834. <https://doi.org/10.1073/pnas.0903766106>

Milescu, L. S., Akk, G., & Sachs, F. (2005). Maximum Likelihood Estimation of Ion Channel Kinetics from Macroscopic Currents. *Biophysical Journal*, 88(4), 2494–2515. <https://doi.org/10.1529/biophysj.104.053256>

Milescu, L. S., Yamanishi, T., Ptak, K., Mogri, M. Z., & Smith, J. C. (2008). Real-Time Kinetic Modeling of Voltage-Gated Ion Channels Using Dynamic Clamp. *Biophysical Journal*, 95(1), 66–87. <https://doi.org/10.1529/biophysj.107.118190>

Milescu, L. S., Yamanishi, T., Ptak, K., & Smith, J. C. (2010). Kinetic Properties and Functional Dynamics of Sodium Channels during Repetitive Spiking in a Slow Pacemaker Neuron. *Journal of Neuroscience*, *30*(36), 12113–12127.

<https://doi.org/10.1523/JNEUROSCI.0445-10.2010>

Mishra, A., Salari, A., Berigan, B. R., Miguel, K. C., Amirshenava, M., Robinson, A., Zars, B. C., Lin, J. L., Milescu, L. S., Milescu, M., & Zars, T. (2018). The *Drosophila* Gr28bD product is a non-specific cation channel that can be used as a novel thermogenetic tool. *Scientific Reports*, *8*(1), 901. [https://doi.org/10.1038/s41598-017-](https://doi.org/10.1038/s41598-017-19065-4)

[19065-4](https://doi.org/10.1038/s41598-017-19065-4)

Missbach, C., Dweck, H. K., Vogel, H., Vilcinskas, A., Stensmyr, M. C., Hansson, B. S., & Grosse-Wilde, E. (2014). Evolution of insect olfactory receptors. *eLife*, *3*, e02115. <https://doi.org/10.7554/eLife.02115>

Moffatt, L. (2007). Estimation of Ion Channel Kinetics from Fluctuations of Macroscopic Currents. *Biophysical Journal*, *93*(1), 74–91.

<https://doi.org/10.1529/biophysj.106.101212>

Navarro, M. A., Hibbard, J. V. K., Miller, M. E., Nivin, T. W., & Milescu, L. S. (2015a). 3D Data Mapping and Real-Time Experiment Control and Visualization in Brain Slices. *Biophysical Journal*, *109*(8), 1521–1527.

<https://doi.org/10.1016/j.bpj.2015.08.045>

Navarro, M. A., Hibbard, J. V. K., Miller, M. E., Nivin, T. W., & Milescu, L. S. (2015b). 3D Data Mapping and Real-Time Experiment Control and Visualization in Brain Slices. *Biophysical Journal*, *109*(8), 1521–1527.

<https://doi.org/10.1016/j.bpj.2015.08.045>

Navarro, M. A., Salari, A., Milesco, M., & Milesco, L. S. (2018). Estimating kinetic mechanisms with prior knowledge II: Behavioral constraints and numerical tests.

Journal of General Physiology, 150(2), 339–354. <https://doi.org/10.1085/jgp.201711912>

Ni, L., Bronk, P., Chang, E. C., Lowell, A. M., Flam, J. O., Panzano, V. C., Theobald, D. L., Griffith, L. C., & Garrity, P. A. (2013a). A gustatory receptor paralogue controls rapid warmth avoidance in *Drosophila*. *Nature*, 500(7464), 580–584.

<https://doi.org/10.1038/nature12390>

Ni, L., Bronk, P., Chang, E. C., Lowell, A. M., Flam, J. O., Panzano, V. C., Theobald, D. L., Griffith, L. C., & Garrity, P. A. (2013b). A gustatory receptor paralogue controls rapid warmth avoidance in *Drosophila*. *Nature*, 500(7464), 580–584.

<https://doi.org/10.1038/nature12390>

Ni, L., Bronk, P., Chang, E. C., Lowell, A. M., Flam, J. O., Panzano, V. C., Theobald, D. L., Griffith, L. C., & Garrity, P. A. (2013c). A gustatory receptor paralogue controls rapid warmth avoidance in *Drosophila*. *Nature*, 500(7464), 580–584.

<https://doi.org/10.1038/nature12390>

Ni, L., Klein, M., Svec, K. V., Budelli, G., Chang, E. C., Ferrer, A. J., Benton, R., Samuel, A. D., & Garrity, P. A. (2016). The Ionotropic Receptors IR21a and IR25a mediate cool sensing in *Drosophila*. *ELife*, 5, e13254.

<https://doi.org/10.7554/eLife.13254>

Nilius, B., Talavera, K., Owsianik, G., Prenen, J., Droogmans, G., & Voets, T. (2005). Gating of TRP channels: A voltage connection? *The Journal of Physiology*,

567(1), 35–44. <https://doi.org/10.1113/jphysiol.2005.088377>

Patapoutian, A. (2005). TRP Channels and Thermosensation. *Chemical Senses*, 30(suppl_1), i193–i194. <https://doi.org/10.1093/chemse/bjh180>

Patapoutian, A., Peier, A. M., Story, G. M., & Viswanath, V. (2003). ThermoTRP channels and beyond: Mechanisms of temperature sensation. *Nature Reviews Neuroscience*, 4(7), 529–539. <https://doi.org/10.1038/nrn1141>

Pavlou, H. J., Lin, A. C., Neville, M. C., Nojima, T., Diao, F., Chen, B. E., White, B. H., & Goodwin, S. F. (2016). Neural circuitry coordinating male copulation. *ELife*, 5, e20713. <https://doi.org/10.7554/eLife.20713>

Pulver, S. R., Pashkovski, S. L., Hornstein, N. J., Garrity, P. A., & Griffith, L. C. (2009). Temporal Dynamics of Neuronal Activation by Channelrhodopsin-2 and TRPA1 Determine Behavioral Output in Drosophila Larvae. *Journal of Neurophysiology*, 101(6), 3075–3088. <https://doi.org/10.1152/jn.00071.2009>

Qin, F., Auerbach, A., & Sachs, F. (1996). Estimating single-channel kinetic parameters from idealized patch-clamp data containing missed events. *Biophysical Journal*, 70(1), 264–280. [https://doi.org/10.1016/S0006-3495\(96\)79568-1](https://doi.org/10.1016/S0006-3495(96)79568-1)

Qin, F., Auerbach, A., & Sachs, F. (2000). A Direct Optimization Approach to Hidden Markov Modeling for Single Channel Kinetics. *Biophysical Journal*, 79(4), 1915–1927. [https://doi.org/10.1016/S0006-3495\(00\)76441-1](https://doi.org/10.1016/S0006-3495(00)76441-1)

Ramsey, I. S., Delling, M., & Clapham, D. E. (2006). An Introduction to Trp Channels. *Annual Review of Physiology*, 68(1), 619–647. <https://doi.org/10.1146/annurev.physiol.68.040204.100431>

Reuss, L., & Grady, T. P. (1979). Effects of external sodium and cell membrane potential on intracellular chloride activity in gallbladder epithelium. *The Journal of Membrane Biology*, 51(1), 15–31. <https://doi.org/10.1007/BF01869341>

Robertson, H. M., Warr, C. G., & Carlson, J. R. (2003). Molecular evolution of the insect chemoreceptor gene superfamily in *Drosophila melanogaster*. *Proceedings of the National Academy of Sciences*, 100(suppl 2), 14537–14542. <https://doi.org/10.1073/pnas.2335847100>

Rosenzweig, M., Brennan, K. M., Tayler, T. D., Phelps, P. O., Patapoutian, A., & Garrity, P. A. (2005). The *Drosophila* ortholog of vertebrate TRPA1 regulates thermotaxis. *Genes & Development*, 19(4), 419–424. <https://doi.org/10.1101/gad.1278205>

Ruffinatti, F. A., Lovisolo, D., Distasi, C., Ariano, P., Erriquez, J., & Ferraro, M. (2011). Calcium signals: Analysis in time and frequency domains. *Journal of Neuroscience Methods*, 199(2), 310–320. <https://doi.org/10.1016/j.jneumeth.2011.05.009>

Salari, A., Navarro, M. A., & Milesescu, L. S. (2016). Modeling the Kinetic Mechanisms of Voltage-Gated Ion Channels. In A. Korngreen (Ed.), *Advanced Patch-Clamp Analysis for Neuroscientists* (pp. 267–304). Springer. https://doi.org/10.1007/978-1-4939-3411-9_13

Salari, A., Navarro, M. A., Milesescu, M., & Milesescu, L. S. (2018). Estimating kinetic mechanisms with prior knowledge I: Linear parameter constraints. *Journal of General Physiology*, 150(2), 323–338. <https://doi.org/10.1085/jgp.201711911>

Salari, A., Vega, B. S., Milescu, L. S., & Milescu, M. (2016). Molecular Interactions between Tarantula Toxins and Low-Voltage-Activated Calcium Channels. *Scientific Reports*, 6(1), 23894. <https://doi.org/10.1038/srep23894>

Sato, K., Pellegrino, M., Nakagawa, T., Nakagawa, T., Vosshall, L. B., & Touhara, K. (2008). Insect olfactory receptors are heteromeric ligand-gated ion channels. *Nature*, 452(7190), 1002–1006. <https://doi.org/10.1038/nature06850>

Sato, K., Tanaka, K., & Touhara, K. (2011). Sugar-regulated cation channel formed by an insect gustatory receptor. *Proceedings of the National Academy of Sciences*, 108(28), 11680–11685. <https://doi.org/10.1073/pnas.1019622108>

Schnell, B., Ros, I. G., & Dickinson, M. H. (2017). A Descending Neuron Correlated with the Rapid Steering Maneuvers of Flying *Drosophila*. *Current Biology*, 27(8), 1200–1205. <https://doi.org/10.1016/j.cub.2017.03.004>

Schobert, B., & Lanyi, J. K. (1982). Halorhodopsin is a light-driven chloride pump. *Journal of Biological Chemistry*, 257(17), 10306–10313. [https://doi.org/10.1016/S0021-9258\(18\)34020-1](https://doi.org/10.1016/S0021-9258(18)34020-1)

Shirai, F., & Hayashi-Takagi, A. (2017). Optogenetics: Applications in psychiatric research. *Psychiatry and Clinical Neurosciences*, 71(6), 363–372. <https://doi.org/10.1111/pcn.12516>

Shyu, W.-H., Chiu, T.-H., Chiang, M.-H., Cheng, Y.-C., Tsai, Y.-L., Fu, T.-F., Wu, T., & Wu, C.-L. (2017). Neural circuits for long-term water-reward memory processing in thirsty *Drosophila*. *Nature Communications*, 8(1), 15230. <https://doi.org/10.1038/ncomms15230>

Spruston, N., Schiller, Y., Stuart, G., & Sakmann, B. (1995). Activity-Dependent Action Potential Invasion and Calcium Influx into Hippocampal CA1 Dendrites. *Science*, 268(5208), 297–300. <https://doi.org/10.1126/science.7716524>

Stengl, M., & Funk, N. W. (2013). The role of the coreceptor Orco in insect olfactory transduction. *Journal of Comparative Physiology. A, Neuroethology, Sensory, Neural, and Behavioral Physiology*, 199(11), 897–909. <https://doi.org/10.1007/s00359-013-0837-3>

Stepanyuk, A., Borisyuk, A., & Belan, P. (2014). Maximum likelihood estimation of biophysical parameters of synaptic receptors from macroscopic currents. *Frontiers in Cellular Neuroscience*, 8, 303. <https://doi.org/10.3389/fncel.2014.00303>

Stepanyuk, A. R., Borisyuk, A. L., & Belan, P. V. (2011). Efficient Maximum Likelihood Estimation of Kinetic Rate Constants from Macroscopic Currents. *PLOS ONE*, 6(12), e29731. <https://doi.org/10.1371/journal.pone.0029731>

Venkatachalam, K., & Montell, C. (2007). TRP Channels. *Annual Review of Biochemistry*, 76(1), 387–417. <https://doi.org/10.1146/annurev.biochem.75.103004.142819>

Venkatachalam, V., & Cohen, A. E. (2014). Imaging GFP-Based Reporters in Neurons with Multiwavelength Optogenetic Control. *Biophysical Journal*, 107(7), 1554–1563. <https://doi.org/10.1016/j.bpj.2014.08.020>

Venkataramanan, L., & Sigworth, F. J. (2002). Applying Hidden Markov Models to the Analysis of Single Ion Channel Activity. *Biophysical Journal*, 82(4), 1930–1942. [https://doi.org/10.1016/S0006-3495\(02\)75542-2](https://doi.org/10.1016/S0006-3495(02)75542-2)

Voets, T. (2014). TRP Channels and Thermosensation. In B. Nilius & V. Flockerzi (Eds.), *Mammalian Transient Receptor Potential (TRP) Cation Channels: Volume II* (pp. 729–741). Springer International Publishing. https://doi.org/10.1007/978-3-319-05161-1_1

Voets, T., Talavera, K., Owsianik, G., & Nilius, B. (2005). Sensing with TRP channels. *Nature Chemical Biology*, *1*(2), 85–92. <https://doi.org/10.1038/nchembio0705-85>

Vosshall, L. B., Wong, A. M., & Axel, R. (2000). An Olfactory Sensory Map in the Fly Brain. *Cell*, *102*(2), 147–159. [https://doi.org/10.1016/S0092-8674\(00\)00021-0](https://doi.org/10.1016/S0092-8674(00)00021-0)

Vries, S. E. J. de, & Clandinin, T. (2013). Optogenetic Stimulation of Escape Behavior in *Drosophila melanogaster*. *JoVE (Journal of Visualized Experiments)*, *71*, e50192. <https://doi.org/10.3791/50192>

Weber, W. (1999). Ion currents of *Xenopus laevis* oocytes: State of the art. *Biochimica Et Biophysica Acta*, *1421*(2), 213–233. [https://doi.org/10.1016/s0005-2736\(99\)00135-2](https://doi.org/10.1016/s0005-2736(99)00135-2)

Wustmann, G., Rein, K., Wolf, R., & Heisenberg, M. (1996). A new paradigm for operant conditioning of *Drosophila melanogaster*. *Journal of Comparative Physiology A*, *179*(3), 429–436. <https://doi.org/10.1007/BF00194996>

Xiao, R., & Xu, X. Z. S. (2021). Temperature Sensation: From Molecular Thermosensors to Neural Circuits and Coding Principles. *Annual Review of Physiology*, *83*(1), 205–230. <https://doi.org/10.1146/annurev-physiol-031220-095215>

Zars, T. (2001). Two thermosensors in *Drosophila* have different behavioral functions. *Journal of Comparative Physiology A*, 187(3), 235–242.

<https://doi.org/10.1007/s003590100194>

Zars, T., Wolf, R., Davis, R., & Heisenberg, M. (2000). Tissue-Specific Expression of a Type I Adenylyl Cyclase Rescues the rutabaga Mutant Memory Defect: In Search of the Engram. *Learning & Memory*, 7(1), 18–31.

<https://doi.org/10.1101/lm.7.1.18>

Zhang, F., Gradinaru, V., Adamantidis, A. R., Durand, R., Airan, R. D., de Lecea, L., & Deisseroth, K. (2010). Optogenetic interrogation of neural circuits: Technology for probing mammalian brain structures. *Nature Protocols*, 5(3), 439–456.

<https://doi.org/10.1038/nprot.2009.226>

Zheng, J. (2013). Molecular Mechanism of TRP Channels. *Comprehensive Physiology*, 3(1), 221–242. <https://doi.org/10.1002/cphy.c120001>

Vita

Marzie Amirshenava was born in Iran, Lahijan and moved to Tehran few years later where she grew and did her education in Biology and Biochemistry at University of Tehran. Marzie were determined to go to grad school when she chose biology as her undergrad major. She met her spouse at University of Tehran where they decided to pursue their education in the United States. Throughout her education, Marzie benefited from the support of many people, but she owes her success to her beloved ones, her mother, sister, and husband, with their ever-present caring and encouragement.